This item is the archived peer-reviewed author-version of:

Plasma-catalytic ammonia synthesis in a DBD plasma : role of microdischarges and their afterglows

Plasma-Catalytic Ammonia Synthesis in a DBD Plasma: Role of the Micro-Discharges and Their Afterglows

K. van 't Veer[1,2,*], Y. Engelmann[1], F. Reniers[2], A. Bogaerts[1,*]

[1]*University of Antwerp, Department of Chemistry, Research Group PLASMANT, Universiteitsplein 1, 2610 Wilrijk-Antwerp, Belgium*

[2] *Université Libre de Bruxelles, Faculty of Sciences, Chemistry of Surfaces, Interfaces and Nanomaterials, CP255, Avenue F. D. Roosevelt 50, B-1050 Brussels, Belgium*

[*]E-mail: kevin.vantveer@uantwerpen.be, annemie.bogaerts@uantwerpen.be

Abstract

Plasma-catalytic ammonia synthesis is receiving ever increasing attention, especially in packed bed dielectric barrier discharge (DBD) reactors. The latter typically operate in the filamentary regime when used for gas conversion applications. While DBDs are in principle well understood and already applied in industry, the incorporation of packing materials and catalytic surfaces considerably adds to the complexity of the plasma physics and chemistry governing the ammonia formation. We employ a plasma kinetics model to gain insights into the ammonia formation mechanisms, paying special attention to the role of the filamentary micro-discharges and their afterglows. During the micro-discharges the synthesized ammonia is actually decomposed, but the radicals created upon electron impact dissociation of N_2 and H_2 and the subsequent catalytic reactions cause a net ammonia gain in the afterglows of the micro-discharges. Under our plasma conditions, electron impact dissociation of N_2 in the gas phase followed by the adsorption of N atoms is identified as rate-limiting step, instead of dissociative adsorption of N_2 at the catalyst surface. Both elementary Eley-Rideal and Langmuir-Hinshelwood reaction steps can be found important in plasma-catalytic NH_3 synthesis.

Keywords

Dielectric barrier discharge, plasma catalysis, ammonia synthesis, Eley-Rideal, Langmuir-Hinshelwood, micro-discharges

Introduction

The potential applications of decentralized ammonia (NH$_3$) synthesis on small scale, i.e. fertilizer production or energy storage,[1] have caused increasing interest in plasma-catalytic NH$_3$ synthesis.[2] Starting late 1960, the synthesis of NH$_3$ in plasma systems has been attributed to 'wall effects', i.e., the reactor walls and/or electrodes appear to have a (catalytic-like) contribution to the NH$_3$ formation.[2] Especially dielectric barrier discharges (DBDs) received major attention over the past few decades.[2–7] DBDs are already commonly used in industry, e.g. for ozone generation,[8] and are quite well understood. However, for plasma-catalytic synthesis, typically a packing material is introduced into the reactor, yielding a so-called packed bed DBD (PB DBD), greatly increasing the complexity. The packing support material and the catalytic material applied on the support influence the discharge characteristics[9] and reaction kinetics. In addition, the discharge characteristics and reaction kinetics, especially in the plasma itself, are closely tied to each other. The radicals or excited molecules created in the plasma can, in turn, either influence the physical properties of the catalytic surface[10] or steer the surface reaction kinetics.[11,12] This causes a complexity that is difficult to resolve with experimental studies only. Hence, modelling studies are helpful, allowing to disentangle the different effects. At the same time, the sheer amount of choice for catalytic and support materials and their intrinsic properties, in combination with the lack of data in literature on the catalytic reaction rates, makes it difficult to capture in detail the full complexity of plasma catalysis in a single model. Therefore, the combination of individual modelling and experimental studies with properly set boundaries can increase our understanding of plasma-catalytic mechanisms. Particularly, NH$_3$ synthesis from N$_2$/H$_2$ feed gas is an important case study due to the simplicity of the reaction (i.e. only NH$_x$ as reaction products).

Mehta *et al*. proposed that vibrational excitation of N$_2$ can increase the NH$_3$ synthesis rate by decreasing the dissociative adsorption energy barrier.[11] Rouwenhorst *et al*. confirmed by additional experiments that indeed vibrational excitation in the plasma helps to overcome this barrier and that further hydrogenation towards NH$_3$ happens on the catalytic surface.[12] However, the specific energy input (SEI) of the DBD plasma was relatively low when compared to typical DBD values, as reported in reference 3. Many researchers observed an increasing NH$_3$ synthesis rate with increasing plasma power (or SEI).[13–17] Aihara *et al*. proposed that NH$_3$ synthesis occurred through the adsorption of electronically excited N$_2$ with further hydrogenation on the surface, based on a direct correlation between the NH$_3$ synthesis rate and electronically activated N$_2$.[13] Zhu *et al.* also hypothesized that electronically excited metastable N$_2$ aids in the adsorption processes.[18] Bai *et al*. assumed ionization to be detrimental

for the NH$_3$ formation.[14] Akay *et al*. argued that NH plasma radicals are most likely created between N and H$_2$, and that NH$_3$ can be formed by further hydrogenation reactions in the gas phase. At the same time, they also reported NH$_3$ formation due to hydrogenation on the surface, starting with N$_2$ and H$_2$ adsorption, but the gas phase and surface reaction pathways were not linked to each other.[15] Peng *et al*. reported the stepwise hydrogenation on the surface as the faster pathway.[16] Hong *et al*. performed a detailed kinetic analysis with and without a catalytic surface. They found that the surface-adsorbed N atoms (i.e. N(s)) were formed mainly by dissociative adsorption of ground state N$_2$ molecules, followed by the first vibrational level and direct adsorption of N atoms. H(s) was also mainly formed by dissociative adsorption from ground state H$_2$ molecules, but followed by direct adsorption of H atoms, and only then by dissociative adsorption from the first vibrational level. The rate of H(s) formation was four orders of magnitude higher than that of N(s). The authors did not only consider stepwise hydrogenation on the surface, but also reactions between gas phase radicals and surface-adsorbed species (so-called Eley-Rideal reactions), and they actually found that the reaction of gas phase NH$_2$ with H(s) was more important in the formation of NH$_3$.[19]

It is clear that the existing studies claim different processes to be important, so there is a clear need for a more detailed understanding. The mentioned studies were all specific to DBDs, but to our knowledge, the strong filamentary micro-discharges and what happens in between them are typically not considered separately in the assessment of the reaction mechanisms.

Therefore, in this study, we present a reaction kinetics analysis, based on a zero-dimensional (0D) plasma kinetics model, in which we explicitly capture the filamentary behaviour of an experimental PB DBD. In the assessment of the reaction mechanisms, we pay special attention to the separate notion of the filamentary micro-discharges and their afterglows. We consider both elementary Eley-Rideal (ER) and Langmuir-Hinshelwood (LH) reaction steps. The LH reactions correspond to the classical (thermal) hydrogenations on the surface, while the ER reactions describe the interaction of plasma radicals with surface-adsorbed species. We will discuss the evolution of the species densities and reaction rates, as well as the overall NH$_3$ formation mechanisms.

Computational Details

We used a time-dependent 0D plasma kinetics model, called ZDPlasKin,[20,21] to investigate the plasma-catalytic synthesis of NH$_3$ from a N$_2$:H$_2$ 1:3 stoichiometric gas mixture in a PB DBD at 400 K and atmospheric pressure. This plasma kinetics model uses rate coefficients from literature to describe the density evolution of various species, i.e. the

3

precursor gases, various plasma radicals, the electrons, various ions, and electronically and vibrationally excited molecules, as well as surface-adsorbed atoms and molecules. The rate coefficients and the concentrations of these species provide the actual reaction rates, which in turn govern the time evolution of all these species, described by the continuity equation:

$$\frac{dn_i}{dt} = S_i = \sum_r c_{i,r} R_r = \sum_r c_{i,r} \left(k_r \prod_c n_c \right) \tag{1}$$

where n is the concentration or density of species i, S is the source term, c is the stochiometric number of the species in reaction r, R is the reaction rate, k is the rate coefficient and the subscript c represents the colliding species in the reaction.

The considered gas phase and surface kinetics were reported in our recent paper[22] and are also listed in the supplementary information (SI, section S.1.1). The surface kinetics use reaction rates based on sticking coefficients corresponding to a metal surface, which could be related to iron,[19,23–27] they describe the catalytic reactions leading to N, H and NH_x adsorption or hydrogenation and the eventual desorption of NH_3. Both elementary ER and LH reaction steps are included.

We assume a surface site density of 10^{15} cm^{-2}, which is generally representative of metal surfaces.[24] This value, together with the volume-to-surface area ratio of the reactor, is used to convert the rate coefficients of the catalytic reactions from s^{-1} to cm^{3}s^{-1}, or cm^{6}s^{-1} in case of dissociative adsorption. A volume-to-surface area ratio of 0.007 cm was used.[23] Any change in these parameters would cause an equal change in the rate coefficients of all surface reactions, i.e. the relative surface reaction rates remain the same.

The surface kinetics are subject to many assumptions and thus also to uncertainties. That includes the exact surface described, i.e. step or surface sites. We describe the surface as being representative of iron, merely for reference and context. A detailed description of the surface kinetics would require micro-kinetics models.[11,28,29] The latter type of model uses surface reaction rates more closely derived from density functional theory calculations and generally solves a system under steady state conditions, while not including a full gas phase chemistry. To our knowledge, such models have not yet been combined with a full time dependent plasma kinetics model, as developed in present study. The present study focusses mainly on the plasma chemistry, and the temporal discharge behaviour (i.e. the role of the micro-discharges and their afterglows). We believe it provides important insights that will allow to better focus future studies, considering that such a combined model would yield an

increased number of degrees of freedom (such as the surface, described by the surface binding energy).[28]

We chose to only describe one surface in our model and neglect the wall effect[2] due to the electrodes or dielectric barrier, which represent different gas-surface interfaces. Indeed, those surfaces would require different kinetic parameters which are subject to the same uncertainties.[25] Furthermore, recent experimental insights show us that the NH_3 formation in an empty reactor is very low compared to a reactor packed with supports (Al_2O_3) and that both cases are significantly lower than when a (metal) catalyst is loaded onto the supports.

The principles to capture the properties of a PB DBD in a 0D model, i.e., how the applied plasma power is distributed over the micro-discharges and their afterglows, are also described in our previous work.[22] In the present work, we derive the plasma conditions from experimentally measured current and voltage characteristics of a PB DBD (see figure S2 and S3 in the SI). The average plasma power was 68 W and a discharge frequency of 23.5 kHz was applied. The reactor volume was 20 ml. The flow rate was 100 ml/min. The reactor was packed with 1.9-2.0 mm diameter Al_2O_3 beads. The measured electrical characteristics determine the plasma parameters during the calculations. Generally, we see no large difference in those characteristics between the Al_2O_3 supports alone and when a metallic coating (5 - 10 wt %) is on the beads. A detailed translation of the experimental conditions is given in the SI (section S.1.2).

To summarize, we mimic the micro-discharges by applying the experimentally measured plasma power over 50 triangular pulses with pulse duration of 200 ns (100 ns at FWHM), equally spaced over the residence time of 3.84 s. In practice, there will be millions of micro-discharges in the reactor during this typical residence time, but individual gas molecules are never exposed to all micro-discharges. Therefore, we consider that individual gas molecules see, on average, 50 micro-discharges over their full gas residence time. This number is based on the average number of micro-discharges that we counted during a single discharge cycle. Each micro-discharge is followed by weaker plasma conditions, with 76.8 ms duration, which we refer to as the afterglow of a micro-discharge. In addition, the first micro-discharge in the model starts at 38.4 ms, to account for the gas that is already present in the plasma reactor before being exposed to an actual micro-discharge.

The adopted maximum and minimum instantaneous plasma power (i.e., during the micro-discharges and their afterglows) correspond to 332 W and 33 W, respectively, based on the typical experimentally measured instantaneous plasma power. These values are converted to a maximum and minimum power density of 3.4×10^6 W/cm^3 and 12 W/cm^3, for the micro-

discharges and their afterglows, respectively. The discharge volumes used in these conversions are based on the micro-discharge and reactor volume, respectively, as described in detail in the SI (section S.1.2). This power is used to heat the electrons, allowing us to also self-consistently calculate the reduced electric field in our model.[22]

Results and Discussion

We studied the production and destruction mechanisms of NH_3 and its precursors during a single micro-discharge and its afterglow. We evaluated the mechanisms in all the successive micro-discharge and afterglow pairs and found that the most important reactions are always the same. Therefore, in the following sections, we focus on the reaction kinetics in the first micro-discharge and afterglow pair, as well as the overall NH_3 evolution during the full residence time.

Surface Coverages and Plasma Species Densities in the Micro-Discharges and Their Afterglows. Our model predicts that the electrons, the plasma radicals and surface-adsorbed species (indicated with (s)) govern the most important reactions taking place, leading to NH_3 production. Some of these species are mainly important in the micro-discharges, while others mainly in the afterglows. Figure 1(a) depicts the surface coverage from the start of the plasma until the end of the first afterglow, while in figure 1(b), the concentrations of the gas phase species are plotted.

The first afterglow ends after approximately 115 ms. At this time scale, the 200 ns micro-discharge pulse is not resolved in figure 1. For the sake of completeness, we plot the time evolutions of the various species during the micro-discharge alone in the SI (section S.2; figure S5). Typical densities of all species in figure 1 are also summarized in table S8.

Figure 1 shows that all the adsorbed and gas phase species rise (either quickly or more gradually) during the first (few) ms, and reach a plateau after approximately 15 ms, i.e., well before the first micro-discharge takes place, while the fraction of empty sites decreases over three orders of magnitude. H(s) is the main adsorbate, and both H(s) and N(s) reach their plateau within 0.3 ms. The coverages or concentrations of NH(s), NH_2(s), H, N, the electrons, NH and NH_2 clearly increase due to the micro-discharge (up to six orders of magnitude), after which they drop back smoothly to almost their original values over approximately 20 ms, but both NH and NH_2 rise slightly again in the late afterglow. The N(s) coverage stays almost constant during the micro-discharge, but rises in the early afterglow, while H(s) is the main adsorbate throughout. The latter is initially due to the dissociative adsorption, which has an initial high reaction rate, and then due to radical adsorption (which is discussed later and in SI

section S.4, figure S12). The NH_3 concentration decreases during the micro-discharges (but only slightly in the first micro-discharge where the NH_3 concentration is still low, see figure S5(b)), but rises in the early afterglow.

Figure 1(b) shows that radicals are already present in the gas phase before the first micro-discharge. This is due to the non-zero power density outside of the micro-discharges. Thus the electrons are already slightly heated by a small amount of power deposition, allowing for electron impact reactions that create the various plasma radicals. However, the reaction rates are of course small compared to the micro-discharge itself.

It is also clear from figure 1(b) that besides the H_2 and N_2 gas molecules (with concentrations of approximately 75 % and 25 %, or 1.4×10^{19} cm^{-3} and 4.6×10^{18} cm^{-3}, respectively; not plotted in figure 1), the H atoms have the highest density in the plasma (1.2×10^{17} cm^{-3} and 1.0×10^{14} cm^{-3} in the micro-discharge and afterglow, respectively; corresponding to an H_2 dissociation degree of 0.4 % and 0.0004 %, respectively), followed by NH_3 (up to 38 ppm or 6.9×10^{14} cm^{-3} after the first micro-discharge and afterglow pair). The N atom density is two orders of magnitude lower than H, corresponding to a maximum concentration of 8.4×10^{14} cm^{-3} in the micro-discharge and an N_2 dissociation degree of 0.01 %; attributed to the much higher bond strength of N_2 (9.8 eV) vs. H_2 (4.5 eV).[30] The NH radical density (1.5×10^{11} cm^{-3}) is the same order of magnitude as the N atom density in the afterglow, while the NH_2 density is one order of magnitude higher (1.9×10^{12} cm^{-3}).
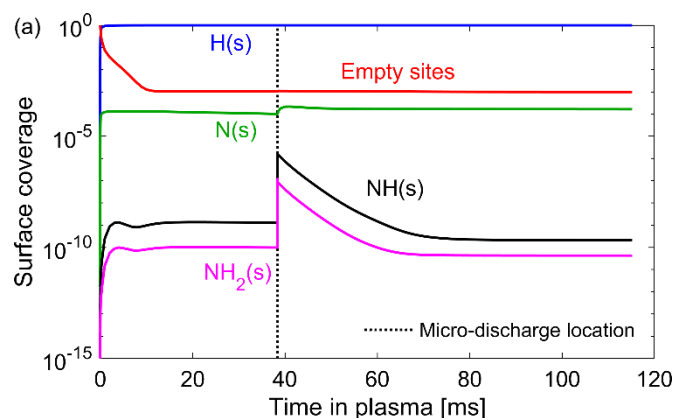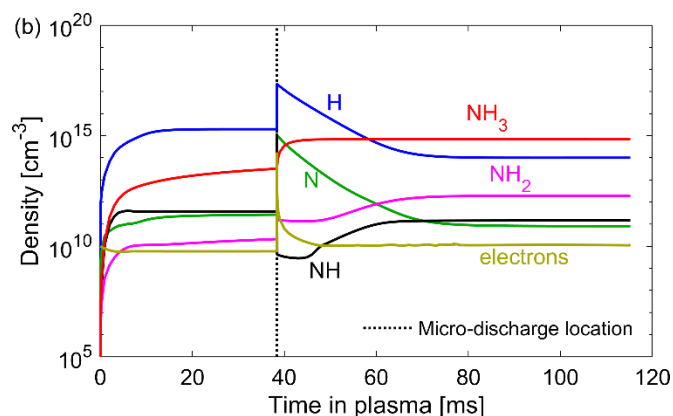
Figure 1. Surface coverages and fraction of empty surface sites (a), and number densities of the neutral gas phase species and electrons (b), as a function of time in the plasma, from the start of the plasma to the end of the first micro-discharge and afterglow pair. The micro-discharge with 200 ns duration takes place at 38.4 ms. The feed gas was N_2:H_2 1:3 and the N_2 and H_2 densities were approximately 4.6×10^{18} cm^{-3} and 1.4×10^{19} cm^{-3}, respectively.

Of course, this figure applies to the first pair of micro-discharge and afterglow. The picture is a bit different after periodic steady state is reached, at least for the NH_3 concentration, because NH_3 will accumulate during successive micro-discharge and afterglow pairs, while the other plasma species already reach periodic steady state after the first pair (see discussions in next section).

Under the present DBD plasma conditions, the electron impact collisions with N_2 and H_2 typically involve the ground state, but also both the electronically and vibrationally excited molecules. In figure 2 we show the time-evolution of the number densities of N_2 and H_2 in the ground state, as well as in the vibrationally and electronically excited states, while in figure 3 we plot the N_2 vibrational distribution function (VDF) in the micro-discharges at various moments in time. The time-evolution of the number densities in the micro-discharge is depicted in the SI (section S.2, figure S6), as well as the H_2 VDF, for completeness (figure S7).

Clearly, in the afterglows the vibrationally excited N_2 and H_2 molecules are higher in density than the electronically excited molecules, and this is most apparent for N_2. The vibrational temperature is approximately 700 K in the afterglows (cf. figure S8(a)). Also, during the micro-discharges, the vibrationally excited N_2 molecules have a higher density than the electronically excited states, and the vibrational temperature reaches 2100 K. On the other hand, the electronically excited H_2 molecules have a higher density than the vibrationally excited states during the micro-discharges (cf. figure S6). The N_2 VDF shows a clear overpopulation compared to a Boltzmann distribution at the gas temperature, both at the start and especially during the micro-discharges. Note that the start of a micro-discharge corresponds to the end of the previous afterglow. An overpopulation is also observed in the afterglows, because of the non-zero power deposition between the micro-discharges, which

allows for continuous electron impact vibrational excitation, in turn causing a non-equilibrium compared to the gas temperature of 400 K.
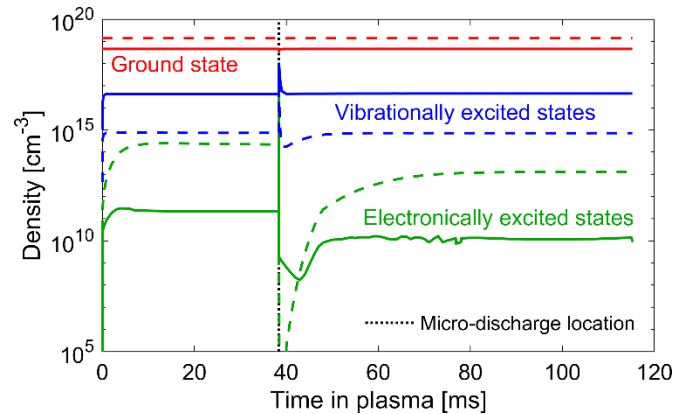

Figure 2. Number densities of the N_2 (solid lines) and H_2 (dashed lines) molecules in the ground state and the sum of the electronically and vibrationally excited states, as a function of time in the plasma, from the start of the plasma to the end of the first micro-discharge and afterglow pair. The micro-discharge with 200 ns duration takes place at 38.4 ms.
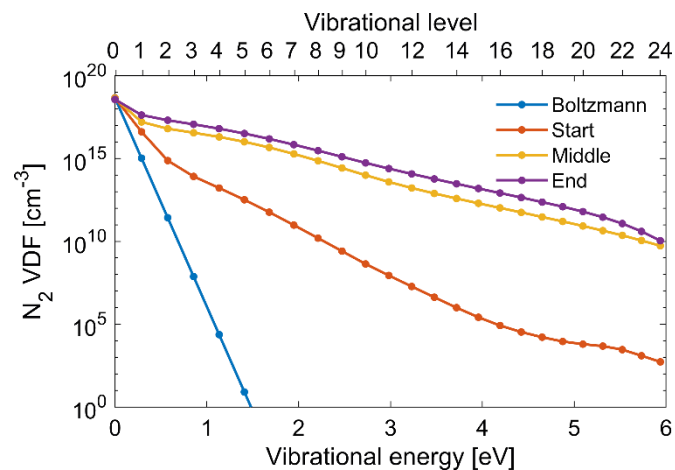

Figure 3. N_2 vibrational distribution function (VDF) at various moments in the micro-discharge, as well as the Boltzmann distribution at the gas temperature (400 K).

Production and Destruction of Plasma Radicals, Adsorbed Species and NH$_3$ in the Micro-discharges and Their Afterglows. To illustrate more clearly whether species are being produced or destroyed during the micro-discharges or the afterglows, we present in figure 4 their time-averaged source terms, for a single micro-discharge and its afterglow separately. As noted before, NH$_2$(s), NH(s), NH$_2$, N(s), and especially NH, H, N and the electrons are net produced during the micro-discharges. For all these neutral species, the source term in the afterglows is destructive but small (compare red bar to gray background, and keeping in mind the log-scale), except for H, which is largely destroyed, and N(s), which is also produced in the afterglow, but again the net production is relatively small (cf. gray background). In other words,

the actual production and destruction in the afterglows (grey bars) are nearly equal for all these species, which means that upon formation, the species are quickly converted into other species. For the electrons, the destruction far exceeds the production in the afterglows. This is attributed to the lack of electron impact ionization processes in the afterglows, where the plasma is significantly weaker compared to the micro-discharges.
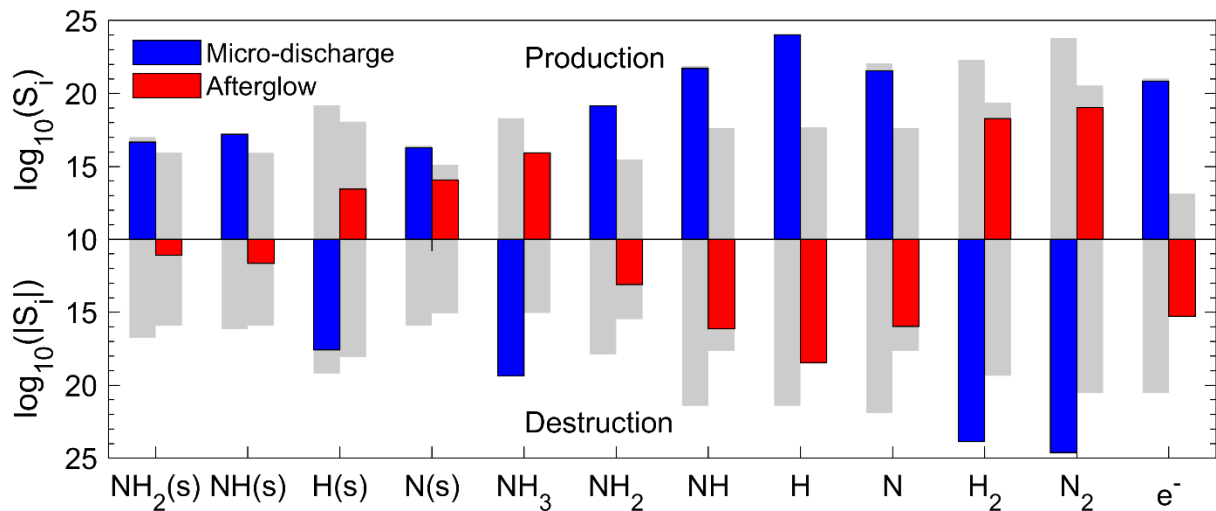

Figure 4. Time-averaged species source terms in the first micro-discharge and its afterglow, of the surface-adsorbed and neutral gas-phase species and the electrons. The source term is either positive or negative, representing net production (top y-axis) and net destruction (bottom y-axis), respectively. The logarithm of the (absolute) source terms S_i is plotted. The grey bars indicate the total production and destruction source terms of the species i, $S_{i,p}$ and $S_{i,d}$, respectively. The net production or destruction $S_i = S_{i,p} - |S_{i,d}|$. Note: the units of S are in cm^{-3} s^{-1}. Comparing the blue or red bars with the grey background reveals whether production is much larger than destruction (or vice versa) (i.e., when the blue or red bar is as large as grey background), or whether they are nearly equal to each other (i.e., when the blue or red bar is smaller than the grey background). In other words, the colored bars correspond to the source terms S_i (cf. equation 1 and y axis labels) which can either be positive (production, upper panel) or negative (destruction, lower panel) and the grey background specifically corresponds to $S_{i,p}$ and $S_{i,d}$ in the micro-discharge and the afterglow.

In contrast to the above species, NH$_3$ is largely destroyed during the micro-discharges and produced in the afterglows. Likewise, the N$_2$ and H$_2$ ground state molecules also exhibit high loss rates during the micro-discharges, because they are converted into reactive species by the electron impact reactions, but their population slightly increases again in the afterglows, due to recombination of these reactive species. This is also illustrated in figure 5, showing the time-averaged source terms of the ground states and electronically and vibrationally excited molecules of both H$_2$ and N$_2$. During the micro-discharges, the ground state H$_2$ and N$_2$ molecules get destroyed, while the electronically and vibrationally excited molecules are produced, and the opposite is true for the afterglows. The production of the N$_2$ vibrational

levels in the micro-discharges and the subsequent depopulation in the afterglows is most pronounced, corresponding to their highest number density (cf. figure 2).
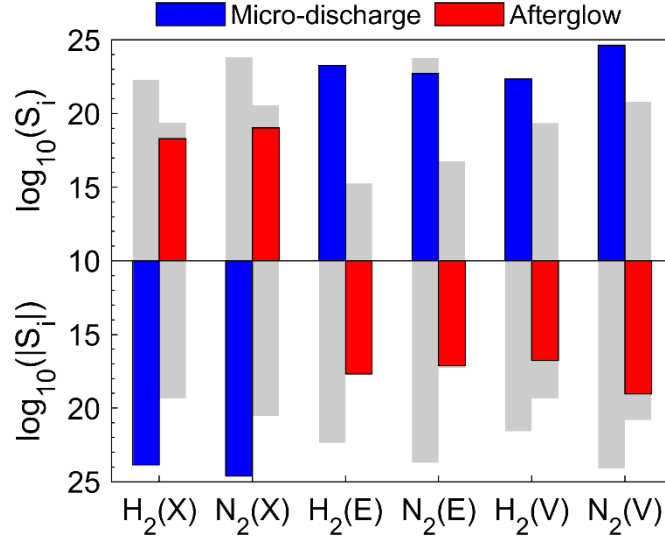

Figure 5. Time-averaged species source terms in the first micro-discharge and its afterglow, of the ground state (X), electronically excited (E) and vibrationally excited (V) H_2 and N_2 molecules. Cf. caption of figure 4 for more information.

In general, the average production and destruction rates and thus the species source terms are much larger in the micro-discharges than in the afterglows (i.e., typically 10^{16} - 10^{23} $cm^{-3}s^{-1}$ vs 10^{14} - 10^{18} $cm^{-3}s^{-1}$), attributed to the stronger plasma environment (cf. the difference in power density, mentioned in section 2) and the associated high radical and electron densities. However, the micro-discharge lifetime is significantly shorter than the afterglow duration (i.e., 200 ns vs 76.8 ms).

Hence, to determine whether the various species accumulate or drop in consecutive micro-discharge and afterglow pairs, we also need to account for the duration of the micro-discharge and afterglow. We calculate the average production-to-destruction ratio across one pair with

$$\frac{P}{D} = \left| \frac{S_{afterglow} \times \tau_{afterglow}}{S_{micro-discharge} \times \tau_{micro-discharge}} \right|^{\alpha} \tag{2}$$

where S is the average source term (i.e., production minus destruction, red and blue bars in figures 4 and 5) of a species in the afterglow or micro-discharge, τ is the duration of the afterglow or micro-discharge, and α is given by

$$\alpha = \begin{cases} 1, & S_{afterglow} > 0 \text{ and } S_{micro-discharge} < 0 \\ -1, & S_{afterglow} < 0 \text{ and } S_{micro-discharge} > 0 \end{cases} \tag{3}$$

For all gas phase and surface-adsorbed species, including electronically and vibrationally excited molecules, equation 2 yields a value of approximately 1, expect for NH_3. This means that the surface coverages and gas phase concentrations of all species very quickly

reach a periodic steady state, while NH_3 is able to accumulate by the consecutive micro-discharges and afterglows, as shown in figure 6.
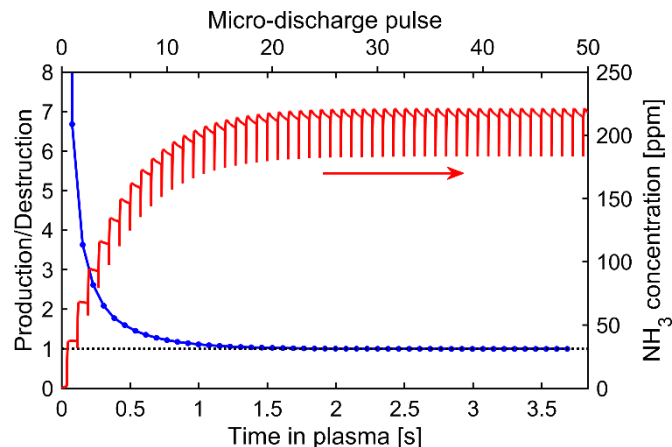

Figure 6. Production-to-destruction ratio of NH_3 based on the net production in the afterglows and net destruction in the micro-discharges (equation 2, left y-axis), and NH_3 concentration (right y-axis), as a function of time (bottom x-axis) and micro-discharge pulse number (top x-axis).

In this figure, the vertical lines in the NH_3 concentration correspond to the destruction of NH_3 in each micro-discharge, followed by the strong rise in the beginning of each subsequent afterglow. Considering that the electron concentration immediately reaches periodic steady state, it is logical that the drop in each micro-discharge increases with rising NH_3 concentration, as the electron impact dissociation rate is proportional to the NH_3 concentration. We identified this process as the main loss mechanism of NH_3 in the micro-discharges. The NH_3 production in the afterglows has to overcome this dissociation in the micro-discharges in order to increase the overall NH_3 concentration. Note that electron impact dissociation still occurs in the afterglows as well, despite a very low electron density. Hence, even in the afterglows, electron impact dissociation determines the eventual steady state NH_3 concentration.

The presented results are for a stoichiometric feed gas ratio (i.e. N_2:H_2 of 1:3), but our model predicts the NH_3 concentration to reach values up to 2000 ppm at higher N_2 contents (not shown). Indeed, for plasma-catalytic NH_3 synthesis, the optimal ratio does not necessary correspond to the stoichiometric gas ratio, among others because N_2 dissociation requires more energy than H_2 dissociation.[30] Furthermore, while we believe that the adopted plasma conditions in our model are representative for a PB DBD, the exact conditions, however, are subject to uncertainties. Therefore, higher NH_3 yields may be reached by using other input values, such as for the maximum and minimum instantaneous power, the micro-discharge volumes and the number of micro-discharges. However, we have generally observed no drastic differences in reaction mechanisms as a function of these model parameters (see also the

species density evolution in our previous work under different conditions[22]). Therefore, while the exact species concentrations in figure 1 and 6 must be considered with caution, as they depend on the conditions assumed in the model, the qualitative reaction mechanisms and the related discussions, presented in the next sections, should still contribute to a better insight.

NH$_3$ Formation: Reaction Rates and Determination of the Rate-Limiting Step. In reaction kinetics, the complete system can reach a steady state, meaning that the plasma parameters and the various species concentrations remain unchanged as a function of time, but reactions can still take place, with the total production and destruction rates of species being equal to each other. When in a chain of consecutive reactions, the reaction rate of the final reaction is equal to those of the preceding steps, the rate-limiting step can be determined. A DBD is a periodic discharge and thus such steady state is not evident. Instead, a periodic steady state might be reached, that is, each discharge period becomes identical.

Our calculations reveal that electron impact dissociation of N$_2$ in the plasma, followed by N adsorption at the catalyst surface, is the rate-limiting step for NH$_3$ synthesis at our conditions, and not dissociative adsorption of N$_2$. This can be explained by the observation that shortly after a micro-discharge, when NH$_3$ increases (cf. figure 1(b)), multiple surface catalytic reaction rates are almost equal to each other. This is true for the formation of NH$_3$ as well as the NH$_3$ precursors. Hence, all intermediate surface species, i.e., N(s), NH(s) and NH$_2$(s), created during the afterglows, are immediately converted towards NH$_3$ according to our model. In addition, electron impact dissociation of the feed gas becomes negligible during this period. The NH$_3$ formation rate was found to be equal to the various adsorption rates of N atoms, i.e. both direct adsorption and the ER reaction between N and H(s). As mentioned, in the early afterglow the N atom source (electron impact dissociation of N$_2$) is not present, and thus, the N atoms are consumed by adsorption, reducing the N density and thus also the N adsorption rate. Consequently, the rates of the further processes (i.e., hydrogenation steps) that exhibit the same rate as the N atom adsorption also drop, and thus also the densities of the NH$_3$ precursors (i.e. NH(s) and NH$_2$(s), cf. figure 1(a)). We summarize this observation in figure 7, while in figure 8 we schematically depict the involved surface reaction mechanisms. A more detailed analysis is presented in the SI (section S.4). We note that the mechanisms in figure 8 are in principle subject to the actual catalytic surface and the temperature at which the process takes place.
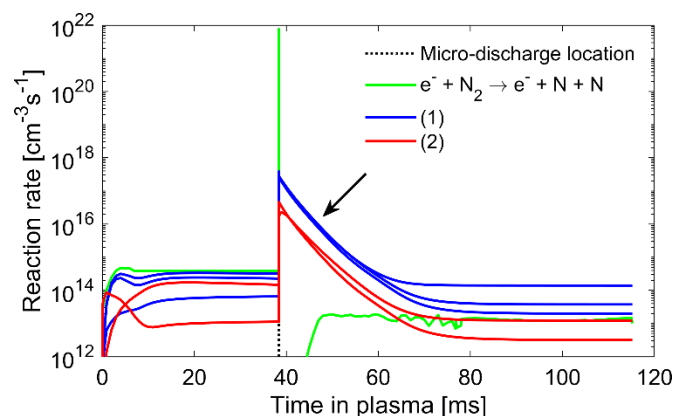
Figure 7. Graphical summary of the detailed analysis presented in the SI (section S.4), showing surface reaction rates that are identical shortly after the micro-discharge (indicated with the arrow) and the N_2 electron impact dissociation rate in the plasma as a function of time, from the start of the plasma to the end of the first micro-discharge and afterglow pair. The micro-discharge with a 200 ns duration takes place at 38.4 ms. The electron impact N_2 dissociation rate, and thus the N atom source, becomes negligible after the micro-discharge. The first group of overlapping reaction rates (1) consists of $N + H(s) \rightarrow NH(s)$, $NH(s) + H(s) \rightarrow NH_2(s)$ and $NH_2(s) + H(s) \rightarrow NH_3$. The second group of overlapping reaction rates (2) consists of $N + Surface \rightarrow N(s)$ and $H + N(s) \rightarrow NH(s)$. The reactions are also depicted in figure 8.
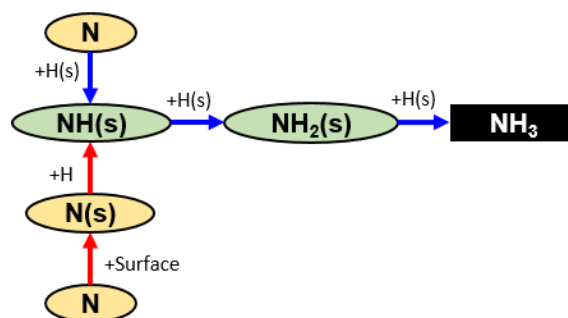
Figure 8. Schematic diagram of the various surface reactions, starting with N atoms, which form NH_3 shortly after a micro-discharge. The blue and red arrows correspond to the reactions in group (1) and (2) in figure 7, respectively.

As part of our detailed analysis (cf. SI, section S.4) we saw a relatively large increase in NH_3 concentration when increasing the N atomic adsorption rates (i.e., $N + Surface \rightarrow N(s)$, $N + H(s) \rightarrow NH(s)$ and $N + N(s) \rightarrow N_2$) and an even larger increase when increasing the N_2 electron impact dissociation rate (cf. figure S14). We conclude that, among the surface reactions, the adsorption of N atoms is the rate-limiting step, both through the ER reaction between N and H(s) and direct adsorption of N, which leads to the other ER reaction, $H + N(s)$ (see Figure 8: blue and red arrows, respectively). This is attributed to both the relatively low N atom gas phase density and the large H(s) surface coverage. Note that the latter reaction is less significant to the formation of NH(s) (cf. figure 7, group (2) compared to group (1)) under the conditions investigated. It is clear that the rate of those reactions can be increased by increasing the N atom density, i.e. by a higher N_2 gas phase dissociation. Thus, we conclude that electron impact N_2 dissociation in the plasma, followed by N adsorption at the surface, is the rate-

14

limiting step determining the NH_3 yield in our DBD. In other words, we do not find that the dissociative N_2 adsorption, from the ground state or vibrational levels, due to the surface itself, is rate limiting.

N_2 Dissociation Rates in the Plasma. The dissociation of N_2 in the plasma occurs exclusively by electron impact collisions. In figure 9, we show the various electron impact N_2 dissociation rates as a function of time. The dissociation is only significant in the micro-discharges and consequently, the N atoms are consumed directly after the micro-discharges. In our previous work we showed that even in a filamentary DBD, vibrational excitation and thus dissociation from vibrational levels can be important.[22] In experiments, high N_2 vibrational temperatures were also reported for PB DBDs.[11,31] Colonna *et al*. showed the significance of the vibrational distribution function and electron energy distribution function in strong ns pulsed N_2 and H_2 discharges.[32,33] As discussed before, our model predicts a maximum N_2 vibrational temperature slightly above 2100 K during the micro-discharges, at the conditions under study, and it relaxes back to slightly above the gas temperature (700 K compared to 400 K) in the afterglows over approximately 1 ms (cf. SI: section S.3, figure S8(a)). Thus, vibrational excitation is quite prominent during the micro-discharges. The reduced electric field (E/N) and electron temperature are also plotted as a function of time in SI (section S.3, figure S8(b)). The maximum E/N was calculated to be 105 Td in each micro-discharge and the maximum electron temperature (T_e) was 5.9 eV. In the afterglows, they reach constant values, around E/N = 6 Td and T_e = 0.7 eV.

| (a) | (b) |
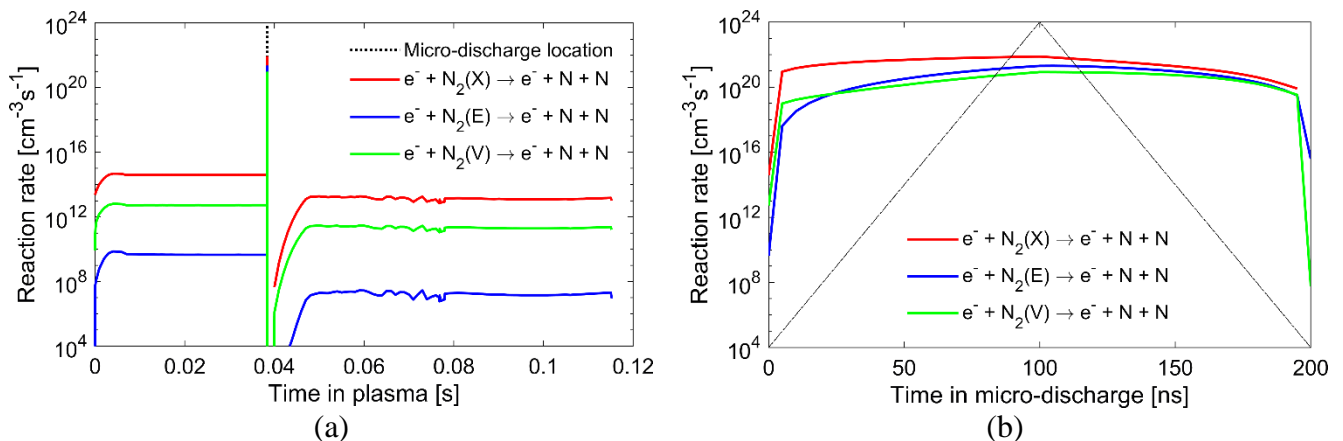
Figure 9. N_2 electron impact dissociation rates from the ground state (X), electronically (E) and vibrationally (V) excited states in the plasma, as a function of time, from the start of the plasma to the end of the first micro-discharge and afterglow pair (a), and as a function of time in the first micro-discharge (b). In (a), the micro-discharge with a 200 ns duration takes place at 38.4 ms.

When comparing the N_2 dissociation rates from the ground state, vibrational levels and electronically excited states in figure 9, it is clear that ground state dissociation is always the

highest, followed by dissociation from the vibrational levels in the afterglows, and from the electronically excited levels during the micro-discharges. However, dissociation from the vibrational levels during the micro-discharges is still high and contributes for 8 % to the total electron impact N_2 dissociation, while the contribution of the ground state and the electronically excited states is 73 % and 19 %, respectively. Compared to the micro-discharges, the dissociation in the afterglows is much lower, and mainly due to the ground state (98.4 %), but dissociation from the vibrational levels (1.6 %) is higher than from electronically excited levels (only 0.0001 %). Even if we account for the duration of the micro-discharges (200 ns) and afterglows (76.8 ms), similar to before (cf. equation 2), we find that 99 % of all N_2 electron impact dissociation occurs during the micro-discharges.

Many authors reported an increase in NH_3 yield upon increasing plasma power or applied voltage.[13–17] A higher plasma power or applied voltage leads to a stronger plasma, and thus higher electron densities and/or energies, and faster electron impact processes, including N_2 dissociation. Hence, these experimental observations from literature qualitatively support our model prediction that electron impact N_2 dissociation in the plasma directly affects the NH_3 formation rate, or in other words, that it can be considered the rate-limiting step for NH_3 formation in DBD plasma.

NH_3 Formation Reaction Scheme for the Micro-discharges and Their Afterglows. Based on the preceding sections, we can summarize the NH_3 formation mechanisms as follows, as revealed by our model. First, dissociative adsorption of H_2 covers the surface with H(s), before the first micro-discharge occurs, due to the large amount of free surface sites (cf. figure 1(a) and SI, section S.2).

$$H_2 + \text{Surface} \rightarrow H(s) + H(s) \tag{4}$$
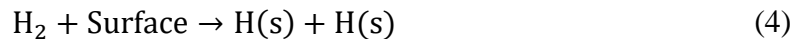
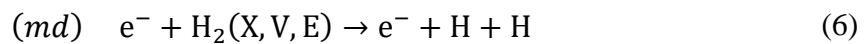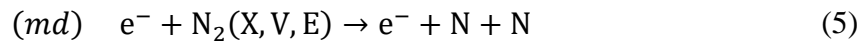Subsequently, during the micro-discharges (indicated with md), first electron impact dissociation of the feed gases takes place, from the ground state but also from the electronically and vibrationally excited states (cf. figure 9).

$$(md) \quad e^- + N_2(X, V, E) \rightarrow e^- + N + N \tag{5}$$

$$(md) \quad e^- + H_2(X, V, E) \rightarrow e^- + H + H \tag{6}$$

The dissociation is enhanced by the high electron density and high electron energy in the micro-discharges (cf. figure 1(b) and figure S8(b)). The high electron density is a result of ionization of the feed gases.

$$(md) \quad e^- + N_2 \rightarrow e^- + e^- + N_2^+ \tag{7}$$

16

$$(md) \quad e^- + H_2 \rightarrow e^- + e^- + H_2^+ \tag{8}$$
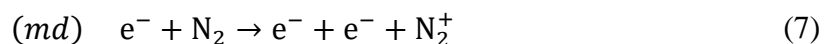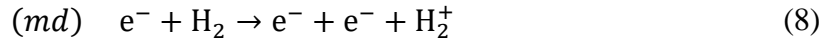
In addition, dissociation of H_2 also occurs upon collisions with electronically excited N_2 (contribution of 10 %).

$$(md) \quad e^- + N_2 \rightarrow e^- + N_2(E) \tag{9}$$

$$(md) \quad N_2(E) + H_2 \rightarrow N_2 + H + H \tag{10}$$
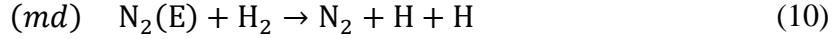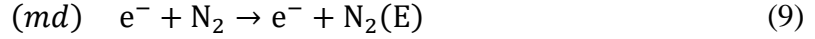
During the micro-discharges, the formation of $NH_2(s)$ from NH and H(s) (ER reaction) is also significant, and even more, it only happens significantly during the micro-discharges (cf. figure S9). The full pathway of this formation mechanism is as follows:

$$(md) \quad e^- + H_2 \rightarrow e^- + H_2(E) \tag{11}$$

$$(md) \quad N + H_2(E) \rightarrow H + NH \tag{12}$$

$$(md) \quad NH + H(s) \rightarrow NH_2(s) \tag{13}$$
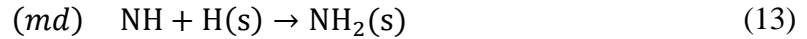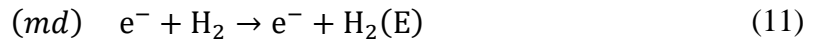
This causes some depletion of H(s) at the surface, but the latter is immediately compensated by the supply of fresh H(s) upon H atom adsorption in the afterglows (indicated with ag) (cf. figure S12 and S13).

$$(ag) \quad H + Surface \rightarrow H(s) \tag{14}$$

Note that during the micro-discharges, H(s) is also consumed via the very large number of H atoms in the plasma (cf. figure 1(b) and SI, section S.2).

$$(md) \quad H + H(s) \rightarrow H_2 \tag{15}$$

H atom recombination is also reported by Shah *et al*. to be more significant due to the surface in comparison with gas phase reactions.[34]

Looking further to the NH_3 formation, the NH_3 precursors are formed according to the same reactions during both the micro-discharges and afterglows, i.e., a combination of ER and LH reactions (cf. figure 7 and 8).

$$(md + ag) \quad N + H(s) \rightarrow NH(s) \tag{16}$$

$$(md + ag) \quad N + Surface \rightarrow N(s) \tag{17}$$

$$(md + ag) \quad H + N(s) \rightarrow NH(s) \tag{18}$$

$$(md + ag) \quad NH(s) + H(s) \rightarrow NH_2(s) \tag{19}$$
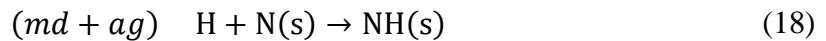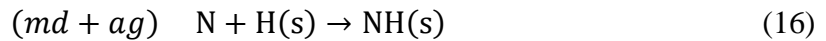
Finally, NH_3 is formed by the following LH reaction (cf. figure 7 and 8).

$$(md + ag) \quad NH_2(s) + H(s) \rightarrow NH_3 \tag{20}$$
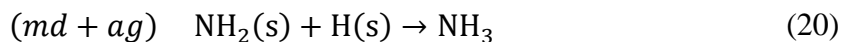
This process takes place both during the micro-discharges and the afterglows, but in the micro-discharges a larger fraction of NH_3 is dissociated (cf. figure 4) due to the high electron density.

$$(md + ag) \quad e^- + NH_3 \rightarrow e^- + NH_2 + H \tag{21}$$

$$(md + ag) \quad e^- + NH_3 \rightarrow e^- + NH + H_2 \tag{22}$$
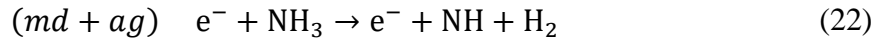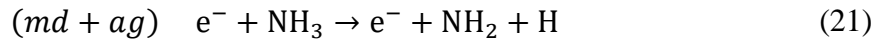
The same reactions govern the eventual NH_3 yield, i.e. in steady state, in the afterglows (cf. figure 6). In other words, reactions 21 and 22 balance with the NH_3 formation in the late afterglow, due to the high NH_3 density, in spite of the low electron density in the afterglows (cf. figure 1(b)). The most significant NH_3 formation in the late afterglow is actually the ER reaction with NH_2.

$$(ag) \quad NH_2 + H(s) \rightarrow NH_3 \tag{23}$$

It should be noted however that this reaction does not contribute to the actual net NH_3 formation (cf. figure 1 and figure S9(a)). NH_3 is mainly formed by reaction 20.

The electrons created in the micro-discharges are lost in the afterglows due to recombination reactions.

$$(ag) \quad e^- + H_3^+ \rightarrow H_2 + H \tag{24}$$

$$(ag) \quad e^- + H_3^+ \rightarrow H + H + H \tag{25}$$

$$(ag) \quad e^- + N_2H^+ \rightarrow N_2 + H \tag{26}$$

The formation of these ions occurs in the micro-discharges through the quick conversion of N_2^+ and H_2^+.

$$(md) \quad H_2^+ + H_2 \rightarrow H_3^+ + H \tag{27}$$

$$(md) \quad N_2^+ + H_2 \rightarrow N_2H^+ + H \tag{28}$$
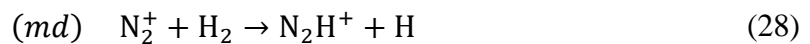
As mentioned, the electrons govern the NH_3 steady state yield (through reactions 21 and 22). They are produced upon ionization reactions 7 and 8, which are followed by charge transfer reactions 27 and 28, of which the products eventually recombine again with the electrons (reaction 24, 25 and 26). Thus, the electron source in the micro-discharges is directly linked to the electron losses in the afterglows. This could explain why in literature, no saturation in NH_3 yield is observed upon increasing the plasma power or applied voltage.[13–17] Nevertheless, Mizushima *et al*. do speculate that NH_3 decomposition is promoted with increasing applied voltage.[35]

Note that recombination reaction 25 is often mentioned in literature to be important for the formation of NH.[36–38] In our model, this is not the case. The latter is in agreement with Molek *et al*. who reports that only 5 % of this recombination leads to NH.[39] On the other hand, this NH formation mechanism may become important at different plasma conditions, such as low pressure.[40–46]

Hong *et al*. performed a kinetic analysis based on a similar model as ours, but the plasma conditions, albeit derived from a PB DBD as well, were described as constants. Thus, their model did not explicitly capture the micro-discharges. They also found that the surface is covered with H(s) under all plasma conditions due to dissociative adsorption (reaction 4), which they attribute to the low dissociation rates in the plasma.[19] This agrees with our model, up to the first micro-discharge. Once a micro-discharge occurs, the dissociation rate in the plasma increases, and our model predicts that direct adsorption of N and H atoms (reaction 14 and 17) are more important. In addition, instead of reaction 12, Hong et al. observed the formation of NH from vibrationally excited H_2.[19] At our plasma conditions, however, the NH formation is only important during the micro-discharges, which represent a stronger plasma than in reference 19, thus it is logical that electronic excitation is more significant, explaining the difference in predicted NH precursors by both models. Furthermore, the subsequent ER reaction that forms $NH_2(s)$ (reaction 13) was reported to be the main $NH_2(s)$ source in reference 19, while in our study, this is again only true during the micro-discharges. In the afterglows, the formation is attributed to an LH reaction instead (reaction 19). Finally, Hong *et al*. did not observe the ions to play an important role in the formation of NH or NH_3,[19] in agreement with our study, and they also found that gas phase NH_2 arises from the dissociation of NH_3 (reaction 21). However, they claimed that NH_2 is recirculated back to the desired products,[19] which is in contrast to the conclusions of our model.

According to our reaction analysis, NH_2 only occurs as product of reaction 21, i.e. NH_3 electron impact dissociation, and it does not actively contribute towards NH_3 formation, despite $NH_2 + H(s) \rightarrow NH_3$ (reaction 23) having the highest NH_3 formation rate in the late afterglow (cf. figure S9(a)). Indeed, collisions with neutral species convert NH_2 into NH and back to the feed gas. Those collisions account for 71 % of the NH_2 destruction in the afterglow, while reaction 23 accounts for 10 % (cf. section S.6, table S11). Furthermore, our model reveals that $N_2(E)$, $H_2(E)$ and NH radicals do not contribute towards NH_3 formation in the afterglows. Indeed, these three species are produced by electron impact collisions, which have a much lower rate in the afterglows than in the micro-discharges (see for example figure 6), and they are quenched back to the feed gas.

As mentioned above, at the DBD conditions under study, our calculations reveal that dissociative adsorption of N_2 does not play a significant role in the NH_3 synthesis. Furthermore, the surface is most significantly covered by H(s). Mehta *et al*. proposed that vibrational excitation of N_2 increases the NH_3 synthesis rate by an enhanced dissociative adsorption rate.[11] If we consider all N(s) sources, i.e. both direct adsorption of N atoms and dissociative adsorption from N_2 ground state and excited molecules, we find that only at the very beginning dissociative adsorption of N_2 molecules in the ground state or from vibrational levels causes the initial coverage with N(s) (96 % and 4 % contribution for ground state and vibrational levels, respectively). The same applies to the initial H(s) adsorption, i.e. due to the empty surface sites and the lack of other radicals. However, quickly thereafter, and already before the first micro-discharge, the contribution from direct adsorption of N atoms is already 98 %, while dissociative adsorption accounts for the remainder of N(s) (i.e., 1.6 % from the ground state and 0.1 % from the vibrational levels). During the micro-discharges, the contribution of dissociative adsorption does not rise, because the N atom density largely increases (cf. figure 1(b)). After the micro-discharges, the contribution of dissociative adsorption reduces further to only 0.28 % and 0.02 % for the ground state and vibrationally excited levels, respectively. Still the contribution of the vibrational levels in the afterglow is generally higher than that of the electronically excited molecules in dissociative adsorption; see also figure S16.

The above reaction mechanisms are summarized in figure 10, in which we also distinguish between the micro-discharges and their afterglows. During the micro-discharges, electron impact excitation creates electronically excited levels ($H_2(E)$, $N_2(E)$), and vibrationally excited levels, while electron impact dissociation of H_2 and N_2 ground state and electronic and vibrationally excited molecules creates H and N atoms, and electron impact ionization creates H_2^+ and N_2^+ ions. The latter are converted into H_3^+ and N_2H^+ ions, which recombine with the electrons in the afterglows. These ions do not contribute to the NH_3 formation. The $N_2(E)$ molecules also contribute to H_2 dissociation. The collision between $H_2(E)$ molecules and N atoms yields NH radicals. In addition, the N atoms adsorb on the surface. Two types of ER reactions (N(s) + H, and H(s) + N) form NH(s). Both NH and NH(s) form $NH_2(s)$ upon reaction with H(s), i.e., in an ER and LH reaction, respectively. Finally, $NH_2(s)$ forms NH_3, but the latter gets destroyed in the micro-discharges upon electron impact dissociation.

In the afterglows, roughly the same processes occur as during the micro-discharges, i.e., the two ER reactions (N(s) + H, and H(s) + N) form NH(s), which reacts further with H(s) into $NH_2(s)$ (LH). Note that the ER reaction (NH + H(s) $\rightarrow$ $NH_2(s)$) does not occur in the afterglows, because there are virtually no NH radicals present in the afterglows. The same is

true for NH_2 radicals, which are actually quenched back to the feed gas (not shown). Finally, $NH_2(s)$ reacts again with $H(s)$ into NH_3 (LH), but in contrast to the micro-discharges, NH_3 is virtually not consumed through electron impact dissociation (except by some residual electrons), so there is net NH_3 formation in the afterglows, until periodic steady state is reached (when NH_3 formation is balanced by dissociation due to the residual electrons at the high NH_3 density).

The data used in the assessment of the reaction mechanisms (reactions 4 through 28 and figure 10) is presented in detail in the SI (section S.6), where we comment on the sensitivity of the assessed mechanisms to possible uncertainties in the underlying reaction rate coefficients. The effect of the uncertainties in rate coefficients has been studied in the past by our group, for plasma-based CO_2 conversion and dry reforming of methane.[47,48] While the absolute values of model outputs, e.g. conversion, were greatly affected by the uncertainties in reaction rate coefficients, the general plasma behavior and reaction pathways remained the same. Hence, we have to keep in mind that the present study aims at qualitatively clarifying the reaction mechanisms, rather than providing quantitative predictions.
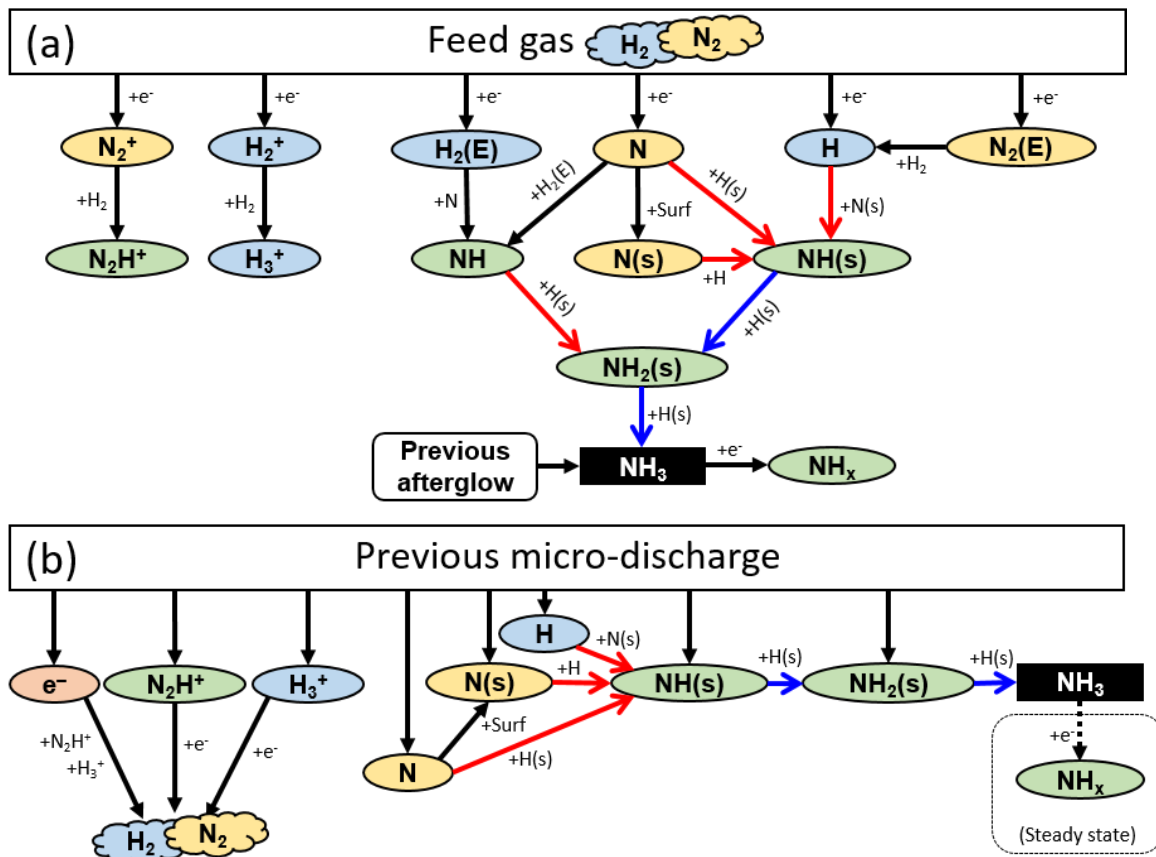
Figure 10. Reaction mechanisms governing the formation of NH_3 in a DBD during the micro-discharges (a) and their afterglows (b). Elementary ER and LH reaction steps are drawn with red and blue arrows, respectively. In (a), the creation of reactive species during the micro-discharges from electron impact collisions with the feed gas is shown, next to the further

reactions of these species into NH$_3$ formation, as well as NH$_3$ destruction. In (b), the further reactions of these species, leading to a net production of NH$_3$ in the afterglows are shown, starting with the radicals produced in the previous micro-discharge.

Within the reaction mechanisms of figure 10, we can thus identify four elementary ER reaction steps taking place during the micro-discharges (i.e., N + H(s) → NH(s); H + N(s) → NH(s); NH + H(s) → NH$_2$(s); and H + H(s) → H$_2$; reaction 16, 18, 13 and 15 above). Two of these reactions (reaction 16 and 18) also play an important role in the afterglows. In addition, both in the micro-discharges and afterglows, two elementary LH reaction steps occur (i.e., NH(s) + H(s) → NH$_2$(s); and NH$_2$(s) + H(s) → NH$_3$; reaction 19 and 20 above) but the ER reactions are mainly responsible for the formation of the precursor, NH(s) (reaction 16 and 18), indicating the overall importance of ER reactions in a DBD plasma.

If we would only consider the gas phase reactions, the most significant NH$_3$ formation (in the afterglow) is due to H + NH$_2$ + M and NH + H$_2$ + M, both with reaction rates in the order of 10^{14} cm^{-3}s^{-1} to 10^{15} cm^{-3}s^{-1}. These reactions account for less than 10 % of the overall NH$_3$ formation rate. A calculation with only the gas phase reactions taken into account results in only 20 ppm of NH$_3$ formed, compared to 220 ppm with the catalytic reactions (cf. figure 6).

The exact reaction mechanisms of course depend on the reaction and activation energies, and in turn, the latter can depend on the surface. For example, the activation barriers for Langmuir-Hinshelwood reactions are different across different metals.[11] Our present model does not easily capture the properties of different metal surfaces, but we have seen that the reaction mechanisms beyond the formation of NH(s) indeed depend on the activation energies of Langmuir-Hinshelwood reactions and the overall available reactions in the chemistry description, and this should be subject to future studies. In the supplementary information (section S.7) we provide a small analysis, which reveals that indeed with faster LH reactions, the results are unchanged and that with slower reactions other reactions will form NH$_3$ with the same reaction rate, resulting in the same NH$_3$ concentrations, due to the reactions being limited by the ER formation of NH(s). Based on these test cases, we found that NH$_3$ can also be formed in a single ER reaction (instead of reactions 19 and 20).

$$H_2 + NH(s) \rightarrow NH_3 \tag{28}$$

We acknowledge that this reaction appears to be a thermal-only process, but that it is generally not considered in typical thermal catalytic models of ammonia synthesis. When this reaction was not considered, we found that the stepwise ER hydrogenation reactions can form NH$_3$ instead.

$$H + NH(s) \rightarrow NH_2(s) \qquad\qquad (29)$$

$$H + NH_2(s) \rightarrow NH_3 \qquad\qquad (30)$$

In addition, the surface is quickly covered by H(s) due to dissociative adsorption due to the large presence of empty surface sites and the lack of radicals at the start of the plasma. The dissociative adsorption rates in principle also depend on the metal surface. This in combination with various feed gas mixtures, i.e. an excess of N_2, could change the (initial) surface coverage towards more N(s). Due to the high gas phase dissociation rate of H_2, the ER reaction between N(s) and H to form NH(s) is then expected to gain importance relative to $H(s) + N \rightarrow NH(s)$.

Our model reveals that radicals play an important role in the assessed reaction mechanisms, through direct adsorption and elementary ER reaction steps. Although the underlying rate coefficients suffer from large uncertainties, as there are no extensive (density functional theory calculation) reports on this type of reactions available yet, Engelmann et al. showed that for typical gas phase concentrations found in DBDs, the radical-surface interactions are important over a wide range of ER activation barriers (i.e. 0 eV to 1.5 eV) for this type of reactions.[28]

Apart from NH_3, which is created due to the presence of the catalytic reactions, the surface is most likely to influence the gas phase composition through the N and H atoms and NH_2 radicals. The former are the most significant gas phase precursors and undergo radical adsorption. The latter is a dissociation product of NH_3 and thus dependent on the formation of NH_3, which happens mainly through the surface reactions. A change in the radical adsorption would either deplete the gas phase N and H atoms quicker or slower. A change in the NH_3 synthesis would result in more or less NH_3 dissociation and consequently NH_2.

The gas phase concentrations would be more directly influenced by the plasma conditions themselves. Those conditions serve as model input (i.e. the power density) and are derived from experimental current and voltage characteristics of a PB DBD. Next to the catalytic reaction rates, the type of packing and the precise catalytic surface can also influence the current-voltage characteristics, which presents another way of the packing or catalytic surface to directly influence the gas phase reaction rates, e.g. dissociation. Indeed, the dielectric constant of the support is known to influence the discharge characteristics.[9] In addition, Patil et al. observed an effect of the (metal) catalyst on the discharge characteristics, but no clear explanation has yet been given.[49]

In their recent paper,[12] Rouwenhorst *et al.* proposed four plasma-catalytic NH_3 synthesis regimes, i.e. (1) NH_3 synthesis in the plasma phase only, (2) NH_3 formation in the plasma phase and at the catalytic surface, through direct adsorption of N and H atoms, which are first formed in the plasma by electron impact dissociation, (3) the same as (2), but H_2 adsorbs dissociatively onto the catalytic surface, and (4) both H_2 and N_2 undergo dissociative adsorption on the catalytic surface and NH_3 formation occurs at the surface only. In the latter case, the dissociative adsorption of N_2 is promoted by vibrational excitation in the plasma, and this regime was claimed to be energetically most favourable.[12] Our model reveals that the conditions under study mostly give rise to the third proposed mechanism, except that in our case, NH_3 is not significantly formed in the gas phase and the adsorption of N atoms does not only occur onto free surface sites.

Conclusions

We performed a detailed kinetic study of NH_3 synthesis in a PB DBD. Such plasma operates in a filamentary regime, characterized by strong micro-discharges, followed by weaker afterglows. Hence, we determined the formation mechanisms that take place in the micro-discharges and their afterglows, as well as how they are connected. Our findings can be summarized as follows.

- Initial surface coverage with H(s).
- Creation of plasma radicals (e.g., N, H, NH) by electron impact collisions in the micro-discharges.
- Adsorption of these radicals onto the surface and subsequent hydrogenation until desorption of NH_3.

The last step causes a net production of NH_3 in the afterglows, while during the micro-discharges, the formed NH_3 is destroyed again by electron impact dissociation.

Specifically, we could identify electron impact dissociation of N_2 during the micro-discharges and the subsequent adsorption of N atoms on the catalyst surface as rate-limiting reaction step for NH_3 formation in a DBD, and thus determining the eventual NH_3 yield, and not dissociative adsorption of N_2. Despite the fact that a PB DBD is typically a filamentary plasma, electron impact dissociation from vibrationally excited N_2 levels still contributes for about 8 % to the overall N_2 dissociation rate in the plasma. The larger this contribution, the more energy efficient the overall NH_3 synthesis would be, as the required dissociation energy is reduced by vibrational excitation. While vibrational excitation can also overcome the energy barrier of dissociative adsorption, within our reaction mechanisms we did not observe this

process to play an important role. The N(s) formation is accounted for by the direct adsorption of N atoms for at least 98 %.

Overall, our model reveals that both elementary ER and LH reaction steps can play an important role in plasma-catalytic NH_3 synthesis. The ER reactions (involving N, H and NH) are mainly attributed to the large abundance of plasma radicals in the micro-discharges, while in the afterglows, only the H and N atoms contribute to ER reactions, forming NH(s), but the subsequent NH_3 formation occurs by LH steps.

However, the rate coefficients used in the model are subject to significant uncertainties. They are adopted from earlier plasma-catalytic models of NH_3 synthesis, and they are often collected from various sources with different conditions (e.g., pressure), and are sometimes explicitly assumed therein. Hence, the model conclusions are only as reliable as the assumptions used, and the assumptions should be considered with caution. This applies especially to the ER sticking coefficients because there is no reliable kinetics data available. In addition, the results will also be sensitive to the reaction temperature and the choice of catalyst. For instance, changing the reaction temperature will significantly influence the surface coverage of adsorbed species and the relative rates of the LH vs ER reactions. Therefore, also the presented results should be considered carefully, certainly in terms of absolute values. However, the predicted trends on the importance of certain pathways are expected to be reliable, as they were found to be the same even when varying the rate coefficients within their range of uncertainties.

In the future we plan to combine this the presented plasma kinetics model with a more detailed surface kinetics model, in which both the specific catalytic surface and the feed gas ratio will be explored. The present study gives novel insights in the interplay between the micro-discharges and their afterglows, which will allow to better focus future studies.

Supplementary Information

S.1. Description of the Model: (S.1.1) Plasma Kinetic and Surface Kinetic Reactions, (S.1.2) Translation of Experimentally Measured Current and Voltage Characteristics to the Model Conditions, (S.1.3) Relationship Between Instantaneous Power and Power Density: Choice of Discharge Volumes

S.2. Surface Coverages and Gas Phase Concentrations in the Micro-Discharge

S.3. Calculated Plasma Parameters

S.4. NH_3 Formation: Detailed Analysis of the Reaction Rates and Determination of the Rate-Limiting Step

S.5. N_2 Dissociative Adsorption Compared Against N Atom Direct Adsorption

Acknowledgments

References

(1)   Chen, J. G.; Crooks, R. M.; Seefeldt, L. C.; Bren, K. L.; Bullock, R. M.; Darensbourg, M. Y.; Holland, P. L.; Hoffman, B.; Janik, M. J.; Jones, A. K.; et al. Beyond Fossil Fuel-Driven Nitrogen Transformations. *Science.* **2018**, *360*, 873.

(2)   Carreon, M. L. Plasma Catalytic Ammonia Synthesis: State of the Art and Future Directions. *J. Phys. D. Appl. Phys.* **2019**, *52*, 483001.

(3)   Bogaerts, A.; Neyts, E. C. Plasma Technology: An Emerging Technology for Energy Storage. *ACS Energy Lett.* **2018**, *3*, 1013–1027.

(4)   Mehta, P.; Barboun, P.; Go, D. B.; Hicks, J. C.; Schneider, W. F. Catalysis Enabled by Plasma Activation of Strong Chemical Bonds: A Review. *ACS Energy Lett.* **2019**, *4*, 1115–1133.

(5)   Hong, J.; Prawer, S.; Murphy, A. B. Plasma Catalysis as an Alternative Route for Ammonia Production: Status, Mechanisms, and Prospects for Progress. *ACS Sustain. Chem. Eng.* **2018**, *6*, 15–31.

(6)   Peng, P.; Chen, P.; Schiappacasse, C.; Zhou, N.; Anderson, E.; Chen, D.; Liu, J.; Cheng, Y.; Hatzenbeller, R.; Addy, M.; et al. A Review on the Non-Thermal Plasma-Assisted Ammonia Synthesis Technologies. *J. Cleaner Prod.* **2018**, *177*, 597–609.

(7)   Peng, P.; Schiappacasse, C.; Zhou, N.; Addy, M.; Cheng, Y.; Zhang, Y.; Ding, K.; Wang, Y.; Chen, P.; Ruan, R. Sustainable Non-Thermal Plasma-Assisted Nitrogen Fixation — Synergistic Catalysis. *ChemSusChem* **2019**, *12*, 3702.

(8)   Kogelschatz, U. Dielectric-Barrier Discharges: Their History , Discharge Physics , and Industrial Applications. *Plasma Chem. Plasma Process.* **2003**, *23*, 1–46.

(9)   Wang, W.; Kim, H.; Laer, K. Van; Bogaerts, A. Streamer Propagation in a Packed Bed Plasma Reactor for Plasma Catalysis Applications. *Chem. Eng. J.* **2018**, *334*, 2467–2479.

(10) Neyts, E. C.; Ostrikov, K. K.; Sunkara, M. K.; Bogaerts, A. Plasma Catalysis: Synergistic Effects at the Nanoscale. *Chem. Rev.* **2015**, *115*, 13408–13446.

(11) Mehta, P.; Barboun, P.; Herrera, F. A.; Kim, J.; Rumbach, P.; Go, D. B.; Hicks, J. C.; Schneider, W. F. Overcoming Ammonia Synthesis Scaling Relations with Plasma-Enabled Catalysis. *Nat. Catal.* **2018**, *1*, 269–275.

(12) Rouwenhorst, K. H. R.; Kim, H.; Le, L. Vibrationally Excited Activation of N_2 in Plasma-Enhanced Catalytic Ammonia Synthesis: A Kinetic Analysis. *ACS Sustainable Chem. Eng.* **2019**, *7*, 17515–17522.

(13) Aihara, K.; Akiyama, M.; Deguchi, T.; Tanaka, M.; Hagiwara, R.; Iwamoto, M. Remarkable Catalysis of a Wool-like Copper Electrode for NH_3 Synthesis from N_2 and H_2 in Non-Thermal Atmospheric Plasma. *Chem. Commun.* **2016**, *52*, 13560-13563.

(14) Bai, M.; Zhang, Z.; Bai, X.; Bai, M.; Ning, W. Plasma Synthesis of Ammonia With a Microgap Dielectric Barrier Discharge at Ambient Pressure. *IEEE Trans. Plasma Sci.* **2003**, *31*, 1285–1291.

(15) Akay, G.; Zhang, K. Process Intensification in Ammonia Synthesis Using Novel Coassembled Supported Microporous Catalysts Promoted by Nonthermal Plasma. *Ind. Eng. Chem. Res.* **2017**, *56*, 457–468.

(16) Peng, P.; Cheng, Y.; Hatzenbeller, R.; Addy, M.; Zhou, N.; Schiappacasse, C.; Chen, D.; Zhang, Y.; Anderson, E.; Liu, Y.; et al. Ru-Based Multifunctional Mesoporous Catalyst for Low-Pressure and Non-Thermal Plasma Synthesis of Ammonia. *Int. J. Hydrogen Energy* **2017**, *42*, 19056–19066.

(17) Barboun, P.; Mehta, P.; Herrera, F. A.; Go, D. B.; Schneider, W. F.; Hicks, J. C. Distinguishing Plasma Contributions to Catalyst Performance in Plasma-Assisted Ammonia Synthesis. *ACS Sustain. Chem. Eng.* **2019**, *7*, 8621–8630.

(18) Zhu, X.; Hu, X.; Wu, X.; Cai, Y.; Zhang, H.; Tu, X. Ammonia Synthesis over γ-Al_2O_3 Pellets in a Packed-Bed Dielectric Barrier Discharge Reactor. **2020**, *53*, 164002.

(19) Hong, J.; Pancheshnyi, S.; Tam, E.; Lowke, J. J.; Prawer, S.; Murphy, A. B. Kinetic Modelling of NH_3 Production in N_2–H_2 Non-Equilibrium Atmospheric-Pressure Plasma Catalysis. *J. Phys. D. Appl. Phys.* **2018**, *51*, 109501.

(20) Pancheshnyi, S.; Eismann, B.; Hagelaar, G. J. M.; Pitchford, L.C. Computer code ZDPlasKin, versions 2.0a; University of Toulouse: LAPLACE, CNRS-UPS-INP, Toulouse, France. http://www.zdplaskin.laplace.univ-tlse.fr (2008).

(21) Hagelaar, G. J. M.; Pitchford, L. C. Solving the Boltzmann Equation to Obtain Electron Transport Coefficients and Rate Coefficients for Fluid Models. *Plasma Sources Sci. Technol.* **2005**, *14*, 722.

(22) van 't Veer, K.; Reniers, F.; Bogaerts, A. Zero-Dimensional Modelling of Unpacked and Packed Bed Dielectric Barrier Discharges: The Role of Vibrational Kinetics in Ammonia Synthesis. *Plasma Sources Sci. Technol.* **2020**, *29*, 045020.

(23) Shah, J.; Wang, W.; Bogaerts, A.; Carreon, M. L. Ammonia Synthesis by Radio Frequency Plasma Catalysis: Revealing the Underlying Mechanisms. *ACS Appl. Energy Mater.* **2018**, *1*, 4824–4839.

(24) Carrasco, E.; Jiménez-Redondo, M.; Tanarro, I.; Herrero, V. J. Neutral and Ion Chemistry in Low Pressure Dc Plasmas of H_2/N_2 Mixtures: Routes for the Efficient Production of NH_3 and NH_4^+. *Phys. Chem. Chem. Phys.* **2011**, *13*, 19561–19572.

(25) Hansen, F. Y.; Henriksen, N. E.; Billing, G. D.; Guldberg, A. Catalytic Synthesis of Ammonia Using Vibrationally Excited Nitrogen Molecules: Theoretical Calculation of Equilibrium and Rate Constants. *Surf. Sci.* **1992**, *264*, 225–234.

(26) Billing, D.; Guldberg, A.; He, N. E.; Hansen, F. Y. Dissociative Chemisorption of N_2 on Rhenium: Dynamics at Low Impact Energies. *Chem. Phys.* **1990**, *147*, 1–11.

(27) Ertl, G. Surface Science and Catalysis- Studies on the Mechanism of Ammonia Synthesis: The P. H. Emmett Award Address. *Catal. Rev. Sci. Eng.* **1980**, *21*, 201–223.

(28) Engelmann, Y.; van 't Veer, K.; Gorbanev, Y.; Neyts, E. C.; Schneider, W. F.; Bogaerts, A. Plasma Catalysis for Ammonia Synthesis: The Importance of Eley-Rideal Reactions. *Submitted.*

(29) Engelmann, Y.; Mehta, P.; Neyts, E. C.; Schneider, W. F.; Bogaerts, A. Predicted Influence of Plasma Activation on Nonoxidative Coupling of Methane on Transition Metal Catalysts. *ACS Sustain. Chem. Eng.* **2020**, *8*, 6043–6054.

(30) Kim, H.; Nanba, T. Atmospheric-Pressure Nonthermal Plasma Synthesis of Ammonia over Ruthenium Catalysts. *Plasma Process. Polym.* **2016**, 1–9.

(31) Uchida, Y.; Takaki, K.; Urashima, K.; Chang, J.-S. Atmospheric Pressure of Nitrogen Plasmas in a Ferro-Electric Packed-Bed Barrier Discharge Reactor Part II: Spectroscopic Measurements of Excited Nitrogen Molecule Density and Its Vibrational Temperature. *IEEE Trans. Dielectr. Electr. Insul.* **2004**, *11*, 491–497.

(32) Colonna, G.; Pietanza, L. D.; Ammando, G. D.; Celiberto, R.; Capitelli, M.; Laricchiuta, A. Vibrational Kinetics of Electronically Excited States in H_2 Discharges. *Eur. Phys. J. D* **2017**, *71*, 279.

(33) Colonna, G.; Laricchiuta, A.; Pietanza, L. D. Time Dependent Selfconsistent Electron Energy Distribution Functions during Nano-Second Repetitive Discharges in Reacting N_2/H_2 Mixtures. *Plasma Phys. Control. Fusion* **2020**, *62*, 014003.

(34) Shah, J.; Gorky, F.; Psarras, P.; Seong, B. Enhancement of the Yield of Ammonia by Hydrogen-Sink Effect during Plasma Catalysis. *ChemCatChem* **2020**, *12*, 1200–1211.

(35) Mizushima, T.; Matsumoto, K.; Sugoh, J. I.; Ohkita, H.; Kakuta, N. Tubular Membrane-like Catalyst for Reactor with Dielectric-Barrier-Discharge Plasma and Its Performance in Ammonia Synthesis. *Appl. Catal. A Gen.* **2004**, *265*, 53–59.

(36) Wang, Y.; Craven, M.; Yu, X.; Ding, J.; Bryant, P.; Huang, J.; Tu, X. Plasma-Enhanced Catalytic Synthesis of Ammonia over a Ni/Al_2O_3 Catalyst at Near-Room Temperature: Insights into the Importance of the Catalyst Surface on the Reaction Mechanism. *ACS Catal.* **2019**, *9*, 10780–10793.

(37) Gómez-ramírez, A.; Lambert, R. M. About the Enhancement of Chemical Yield during the Atmospheric Plasma Synthesis of Ammonia in a Ferroelectric Packed Bed Reactor. *Plasma Process. Polym.* **2016**, *2016*, 1–8.

(38) Gómez-Ramírez, A.; Cotrino, J.; Lambert, R. M.; González-Elipe, A. R. Efficient Synthesis of Ammonia from N_2 and H_2 Alone in a Ferroelectric Packed-Bed DBD Reactor. *Plasma Sources Sci. Technol.* **2015**, *24*, 065011.

(39) Molek, C. D.; Mclain, J. L.; Poterya, V.; Adams, N. G.; Uni, V.; Heyro, J. V. A Remeasurement of the Products for Electron Recombination of N_2H^+ Using a New Technique: No Significant NH + N Production. **2007**, 6760–6765.

(40) Brewer, A. K.; WestHaver, J. W. The Synthesis of Ammonia in the Glow Discharge. *J.*

Phys. Chem. **1929**, *33*, 883–895.

(41)   Brewer, A. K.; Westhaver, J. W. Chemical Action in the Glow Discharge II. Further Investigation on the Synthesis of Ammonia. *J. Phys. Chem.* **1930**, *34*, 153–164.

(42)   Botchway, G. Y.; Venugopalan, M. Plasma Synthesis of Ammonia in Presence of an Iron Catalyst. *Zeitschrift für Phys. Chemie Neue Folge* **1980**, *120*, 103–110.

(43)   Yin, K. S.; Venugopalan, M. Plasma Chemical Synthesis. I. Effect of Electrode Material on the Synthesis of Ammonia. *Plasma Chem. Plasma Process.* **1983**, *3*, 343–350.

(44)   Touvelle, M.; Licea, J. L. M.; Venugopalan, M. Plasma Chemical Synthesis. II. Effect of Wall Surface on the Synthesis of Ammonia. *Plasma Chem. Plasma Process.* **1987**, *7*, 101–108.

(45)   Uyama, H.; Matsumoto, O. Synthesis of Ammonia in High-Frequency Discharges. *Plasma Chem. Plasma Process.* **1989**, *9*, 13–24.

(46)   Uyama, H.; Matsumoto, O. Synthesis of Ammonia in High-Frequency Discharges. II. Synthesis of Ammonia in a Microwave Discharge under Various Conditions. *Plasma Chem. Plasma Process.* **1989**, *9*, 421–432.

(47)   Berthelot, A.; Bogaerts, A. Modeling of CO_2 Plasma: Effect of Uncertainties in the Plasma Chemistry. *Plasma Sources Sci. Technol.* **2017**, *26*, 115002.

(48)   Wang, W.; Berthelot, A.; Zhang, Q.; Bogaerts, A. Modelling of Plasma-Based Dry Reforming: How Do Uncertainties in the Input Data Affect the Calculation Results? *J. Phys. D. Appl. Phys.* **2018**, *51*, 204003.

(49)   Patil, B. S. *et al.* The role of heterogeneous catalysts in the plasma-catalytic ammonia synthesis. *Catal. Today* **2020**, doi:10.1016/j.cattod.2020.06.074

TOC Graphic
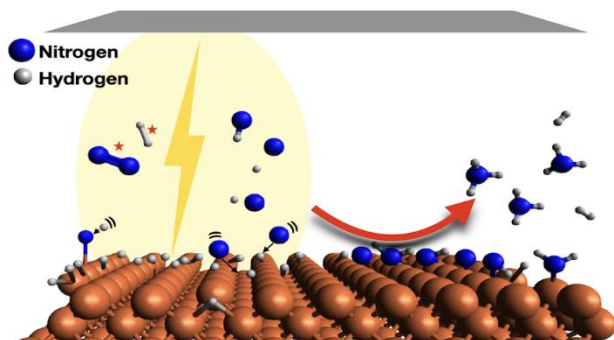
Supplementary Information:

Plasma-Catalytic Ammonia Synthesis in a DBD Plasma: Role of the Micro-Discharges and Their Afterglows

K. van 't Veer[1,2,*], Y. Engelmann[1], F. Reniers[2], A. Bogaerts[1,*]

[1]*University of Antwerp, Department of Chemistry, Research Group PLASMANT, Universiteitsplein 1, 2610 Wilrijk-Antwerp, Belgium*

[2] *Université Libre de Bruxelles, Faculty of Sciences, Chemistry of Surfaces, Interfaces and Nanomaterials, CP255, Avenue F. D. Roosevelt 50, B-1050 Brussels, Belgium*

[*]E-mail: kevin.vantveer@uantwerpen.be, annemie.bogaerts@uantwerpen.be

S.1. Description of the Model

We used a time-dependent 0D plasma kinetics model[1,2] to investigate a PB DBD. The principles to capture the properties of a PB DBD in a 0D model are already described in our previous work.[3] We list the chemical reactions in the plasma and at the surface in section S.1.1. In contrast to our previous work, we now derive the plasma conditions more directly from experimentally measured current and voltage characteristics of a PB DBD, as described in section S.1.2 and S.1.3.

S.1.1. Plasma Kinetic and Surface Kinetic Reactions

Table S1 through S5 report all the gas phase reactions included in the model. In table S1, the electron-impact reactions are reported, most of which are evaluated from a unique cross section (i.e. $\sigma(\epsilon)$, with ϵ the electron energy) and the electron energy distribution function, which is calculated in the model with BOLSIG+.[2] Each cross section has a different threshold energy, which describes the onset of the reaction. For example, the threshold energy of N_2 dissociation is higher than of H_2 dissociation (9.8 eV and 4.5 eV, respectively).[4] Table S5 reports the included vibrational interactions of the feed gas molecules. Table S6 reports the surface kinetics, followed by a small discussion on the parameters describing those reactions.

Table S1. Electron-impact collisions describing the plasma kinetics. The ground state, vibrational levels and electronically excited states are indicated with X, V and E, respectively. The temperatures are given in Kelvin unless otherwise noted.

#	Reaction			Rate coefficient	Ref.	
	Excitation and de-excitation					
R1	$e^- + H_2(X,V)$	$\leftrightarrow$	$e^- + H_2(E)$	$\sigma_{R1}(\epsilon)$	[5]	[1,2,3]
R2	$e^- + N_2(X,V)$	$\leftrightarrow$	$e^- + N_2(E)$	$\sigma_{R2}(\epsilon)$	[5]	[1,2,3]
R3	$e^- + N$	$\rightarrow$	$e^- + N(E)$	$\sigma_{R3}(\epsilon)$	[5]	[1]
	Ionization					
R4	$e^- + N_2(X,V,E)$	$\rightarrow$	$e^- + e^- + N_2^+$	$\sigma_{R4}(\epsilon)$	[6]	[1,2]
R5	$e^- + H_2(X,V)$	$\rightarrow$	$e^- + e^- + H_2^+$	$\sigma_{R5}(\epsilon)$	[5]	[1,2]
R6	$e^- + N$	$\rightarrow$	$e^- + e^- + N^+$	$\sigma_{R6}(\epsilon)$	[5]	[1]

R7	$e^- + H$	$\rightarrow$	$e^- + e^- + H^+$	$\sigma_{R7}(\epsilon)$	[6] [1]
R8	$e^- + NH$	$\rightarrow$	$e^- + e^- + NH^+$	$\sigma_{R8}(\epsilon)$	[7] [1]
R9	$e^- + NH_2$	$\rightarrow$	$e^- + e^- + NH_2^+$	$\sigma_{R9}(\epsilon)$	[7] [1]
R10	$e^- + NH_3$	$\rightarrow$	$e^- + e^- + NH_3^+$	$\sigma_{R10}(\epsilon)$	[7] [1]

Dissociative Ionization

R11	$e^- + N_2(X,V)$	$\rightarrow$	$e^- + e^- + N^+ + N$	$\sigma_{R11}(\epsilon)$	[8] [1]
R12	$e^- + H_2$	$\rightarrow$	$e^- + e^- + H + H^+$	$\sigma_{R12}(\epsilon)$	[9] [1]
R13	$e^- + NH$	$\rightarrow$	$e^- + e^- + H + N^+$	$\sigma_{R13}(\epsilon)$	[7] [1]
R14	$e^- + NH_2$	$\rightarrow$	$e^- + e^- + H + NH^+$	$\sigma_{R14}(\epsilon)$	[7] [1]
R15	$e^- + NH_3$	$\rightarrow$	$e^- + e^- + H + NH_2^+$	$\sigma_{R15}(\epsilon)$	[7] [1]

Dissociation

R16	$e^- + H_2$	$\rightarrow$	$e^- + H + H$	$\sigma_{R16}(\epsilon)$	[9] [1]
R17	$e^- + N_2(X,V,E)$	$\rightarrow$	$e^- + N + N$	$\sigma_{R17}(\epsilon)$	[5] [1,2]
R18	$e^- + NH$	$\rightarrow$	$e^- + N + H$	$5.0 \times 10^{-8} T_e[\text{eV}]^{0.5} \exp(-8.6/T_e[\text{eV}])$	[10]
R19	$e^- + NH_2$	$\rightarrow$	$e^- + N + H_2$	$5.0 \times 10^{-8} T_e[\text{eV}]^{0.5} \exp(-7.6/T_e[\text{eV}])$	[10]
R20	$e^- + NH_2$	$\rightarrow$	$e^- + NH + H$	$5.0 \times 10^{-8} T_e[\text{eV}]^{0.5} \exp(-7.6/T_e[\text{eV}])$	[10]
R21	$e^- + NH_3$	$\rightarrow$	$e^- + NH_2 + H$	$5.0 \times 10^{-8} T_e[\text{eV}]^{0.5} \exp(-4.4/T_e[\text{eV}])$	[10]
R22	$e^- + NH_3$	$\rightarrow$	$e^- + NH + H_2$	$5.0 \times 10^{-8} T_e[\text{eV}]^{0.5} \exp(-5.5/T_e[\text{eV}])$	[10]

(Dissociative) recombination

R23	$e^- + N_2^+$	$\rightarrow$	$N + N$	$0.50 \times 1.8 \times 10^{-7}(300/T_e)^{0.39}$	[11]
R24	$e^- + N_2^+$	$\rightarrow$	$N + N(^2D^0)$	$0.45 \times 1.8 \times 10^{-7}(300/T_e)^{0.39}$	[11]
R25	$e^- + N_2^+$	$\rightarrow$	$N + N(^2P^0)$	$0.05 \times 1.8 \times 10^{-7}(300/T_e)^{0.39}$	[11]
R26	$e^- + N_3^+$	$\rightarrow$	$N_2 + N$	$2.0 \times 10^{-7}(300/T_e)^{0.5}$	[11]
R27	$e^- + N_3^+$	$\rightarrow$	$N_2(A^3) + N$	$6.91 \times 10^{-8} T_e[\text{eV}]^{-0.5}$	[12]
R28	$e^- + N_3^+$	$\rightarrow$	$N_2(B^3) + N$	$6.91 \times 10^{-8} T_e[\text{eV}]^{-0.5}$	[12]
R29	$e^- + N_4^+$	$\rightarrow$	$N_2 + N_2$	$2.3 \times 10^{-6}(300/T_e)^{0.53}$	[11]
R30	$e^- + N_4^+$	$\rightarrow$	$N_2 + N + N$	$3.13 \times 10^{-7} T_e[\text{eV}]^{-0.41}$	[12]
R31	$e^- + H_2^+$	$\rightarrow$	$H + H$	see footnote[4]	[10] [4]
R32	$e^- + H_3^+$	$\rightarrow$	$H + H + H$	see footnote[5]	[10] [5]
R33	$e^- + H_3^+$	$\rightarrow$	$H_2 + H$	see footnote[5]	[10] [5]
R34	$e^- + NH^+$	$\rightarrow$	$N + H$	$4.30 \times 10^{-8}(0.026/T_e[\text{eV}])^{0.5}$	[10]
R35	$e^- + NH_2^+$	$\rightarrow$	$NH + H$	$1.02 \times 10^{-7}(0.026/T_e[\text{eV}])^{0.4}$	[10]
R36	$e^- + NH_2^+$	$\rightarrow$	$N + H + H$	$1.98 \times 10^{-7}(0.026/T_e[\text{eV}])^{0.4}$	[10]
R37	$e^- + NH_3^+$	$\rightarrow$	$NH + H + H$	$1.55 \times 10^{-7}(0.026/T_e[\text{eV}])^{0.5}$	[10]
R38	$e^- + NH_3^+$	$\rightarrow$	$NH_2 + H$	$1.55 \times 10^{-7}(0.026/T_e[\text{eV}])^{0.5}$	[10]
R39	$e^- + NH_4^+$	$\rightarrow$	$NH_3 + H$	$8.01 \times 10^{-7}(0.026/T_e[\text{eV}])^{0.605}$	[10]
R40	$e^- + NH_4^+$	$\rightarrow$	$NH_2 + H + H$	$1.23 \times 10^{-7}(0.026/T_e[\text{eV}])^{0.605}$	[10]
R41	$e^- + N_2H^+$	$\rightarrow$	$N_2 + H$	$7.1 \times 10^{-7}(0.026/T_e[\text{eV}])^{0.72}$	[10]

Three-body recombination

#	Reaction		Rate coefficient	Ref.	
R42	$e^- + N^+ + e^-$	$\rightarrow$ $N + e^-$	$7.0 \times 10^{-20}(300/T_e)^{4.5}$	[11]	
R43	$e^- + N^+ + M$	$\rightarrow$ $N + M$	$6.0 \times 10^{-27}(300/T_e)^{1.5}$	[13]	[6]
R44	$e^- + N_2^+ + e^-$	$\rightarrow$ $N_2 + e^-$	$1.0 \times 10^{-19}(T_e/300)^{-4.5}$	[13]	
R45	$e^- + N_2^+ + M$	$\rightarrow$ $N_2 + M$	$2.49 \times 10^{-29}T_e[eV]^{-1.5}$	[12]	[6]
Attachment					
R46	$e^- + H_2(X, V)$	$\rightarrow$ $H + H^-$	$\sigma_{R46}(\epsilon)$	[14,15]	[1,7]

[1] The rate coefficient is calculated from the electron impact cross section $\sigma(\epsilon)$ using BOLSIG+.[2] The reference of the cross section is given.

[2] The cross section threshold energy is reduced when the reaction takes places from an excited state.

[3] The rate coefficients for de-excitation processes are calculated using detailed balancing.[2]

[4] The rate coefficient is a fit as a function of the electron temperature, given by: $k = 7.51 \times 10^{-9} - 1.12 \times 10^{-9}T_e[eV]^1 + 1.03 \times 10^{-10}T_e[eV]^2 - 4.15 \times 10^{-12}T_e[eV]^3 + 5.86 \times 10^{-14}T_e[eV]^4$.[10]

[5] The rate coefficient is a fit as a function of the electron temperature, given by: $k = 0.5 \times (8.39 \times 10^{-9} + 3.02 \times 10^{-9}T_e[eV]^1 - 3.80 \times 10^{-10}T_e[eV]^2 + 1.31 \times 10^{-11}T_e[eV]^3 + 2.42 \times 10^{-13}T_e[eV]^4 - 2.30 \times 10^{-14}T_e[eV]^5 + 3.55 \times 10^{-16}T_e[eV]^6)$.[10]

[6] The third body, M, is any neutrally charged gas phase species.

[7] The cross section data is resolved for each individual vibrational state.[14,15]

Table S2 Neutral-neutral collisions describing the plasma kinetics. The ground state and vibrational levels are indicated with X and V, respectively. The temperatures are given in Kelvin.

#	Reaction		Rate coefficient	Ref.	
Neutral-neutral collisions					
R47	$N_2(X, V) + M$	$\rightarrow$ $N + N + M$	$8.37 \times 10^{-4}(T_g/298)^{-3.50}\exp(-113710/T_g)$	[16]	[1,2]
R48	$N(^2D^0) + M$	$\rightarrow$ $N + M$	2.4×10^{-14}	[17]	[2]
R49	$N(^2P^0) + N$	$\rightarrow$ $N(^2D^0) + N$	1.8×10^{-12}	[11]	
R50	$N(^2P^0) + N_2$	$\rightarrow$ $N + N_2$	2.0×10^{-18}	[11]	
R51	$N_2(a'^1) + N$	$\rightarrow$ $N_2 + N$	2.0×10^{-11}	[17]	
R52	$N_2(a'^1) + N_2$	$\rightarrow$ $N_2 + N_2$	3.7×10^{-16}	[17]	
R53	$N_2(a'^1) + N_2$	$\rightarrow$ $N_2(B^3) + N_2$	1.9×10^{-13}	[11]	
R54	$N_2(A^3) + N$	$\rightarrow$ $N_2 + N(^2P^0)$	$4.0 \times 10^{-11}(300/T_g)^{0.667}$	[11]	
R55	$N_2(A^3) + N$	$\rightarrow$ $N_2 + N$	2.0×10^{-12}	[11]	
R56	$N_2(A^3) + N_2$	$\rightarrow$ $N_2 + N_2$	3.0×10^{-16}	[11]	
R57	$N_2(A^3) + N_2(A^3)$	$\rightarrow$ $N_2 + N_2(A^3)$	2.0×10^{-12}	[17]	
R58	$N_2(A^3) + N_2(A^3)$	$\rightarrow$ $N_2 + N_2(B^3)$	3.0×10^{-10}	[11]	
R59	$N_2(A^3) + N_2(A^3)$	$\rightarrow$ $N_2 + N_2(C^3)$	1.5×10^{-10}	[11]	
R60	$N_2(B^3) + N_2$	$\rightarrow$ $N_2 + N_2$	2.0×10^{-12}	[11]	
R61	$N_2(B^3) + N_2$	$\rightarrow$ $N_2(A^3) + N_2$	3.0×10^{-11}	[11]	
R62	$N_2(C^3) + N_2$	$\rightarrow$ $N_2(a'^1) + N_2$	1.0×10^{-11}	[11]	
R63	$N + NH$	$\rightarrow$ $H + N_2$	5×10^{-11}	[18]	
R64	$H + NH$	$\rightarrow$ $N + H_2$	$5.4 \times 10^{-11}\exp(-165/T_g)$	[18]	

R65	$NH + NH$	$\rightarrow$	$H_2 + N_2$	$5 \times 10^{-14}(T_g/300)$	[18]	[3]
R66	$NH + NH$	$\rightarrow$	$N + NH_2$	$1.7 \times 10^{-12}(T_g/300)^{1.5}$	[18]	[3]
R67	$NH + NH$	$\rightarrow$	$N_2 + H + H$	8.5×10^{-11}	[18]	[3]
R68	$H + NH_2$	$\rightarrow$	$H_2 + NH$	$6.6 \times 10^{-11}\exp(-1840/T_g)$	[18]	
R69	$N + NH_2$	$\rightarrow$	$N_2 + H + H$	1.2×10^{-10}	[18]	
R70	$N + NH_2$	$\rightarrow$	$N_2 + H_2$	1.2×10^{-10}	[18]	
R71	$NH + NH_2$	$\rightarrow$	$NH_3 + N$	1.66×10^{-12}	[18]	[4]
R72	$H_2(V) + N$	$\rightarrow$	$NH + H$	$4.0 \times 10^{-10}(T_g/300)^{0.5}\exp(-16600/T_g)$	[18]	[5]
R73	$H_2 + NH_2$	$\rightarrow$	$NH_3 + H$	$5.4 \times 10^{-11}\exp(-6492/T_g)$	[18]	
R74	$H + NH_3$	$\rightarrow$	$NH_2 + H_2$	$8.4 \times 10^{-14}(T_g/300)^{4.1}\exp(-4760/T_g)$	[18]	
R75	$N_2(A^3) + H$	$\rightarrow$	$N_2 + H$	5×10^{-11}	[18]	
R76	$N_2(A^3) + H_2$	$\rightarrow$	$N_2 + H + H$	$2 \times 10^{-10}\exp(-3500/T_g)$	[18]	
R77	$N_2(A^3) + NH_3$	$\rightarrow$	$N_2 + NH_3$	1.6×10^{-10}	[18]	
R78	$N_2(B^3) + H_2$	$\rightarrow$	$N_2(A^3) + H_2$	2.5×10^{-11}	[18]	
R79	$N_2(a'^1) + H$	$\rightarrow$	$N_2 + H$	1.5×10^{-11}	[18]	
R80	$N_2(a'^1) + H_2$	$\rightarrow$	$N_2 + H + H$	2.6×10^{-11}	[18]	
R81	$N + H_2(E)$	$\rightarrow$	$H + NH$	$4.0 \times 10^{-10}(T_g/300)^{0.5}$	[18]	
R82	$N(^2D^0) + H_2$	$\rightarrow$	$H + NH$	2.3×10^{-12}	[18]	
R83	$N(^2D^0) + NH_3$	$\rightarrow$	$NH + NH_2$	1.1×10^{-10}	[18]	
R84	$N(^2P^0) + H_2$	$\rightarrow$	$H + NH$	2.5×10^{-14}	[18]	
R85	$N + NH$	$\rightarrow$	$H + N + N$	$4.02 \times 10^{-10}(T_g/298)^{-0.20}\exp(-27303/T_g)$	[19]	
R86	$H_2 + NH$	$\rightarrow$	$H + NH_2$	$3.50 \times 10^{-11}\exp(-7758/T_g)$	[20]	
R87	$N_2 + H$	$\rightarrow$	$NH + N$	$5.27 \times 10^{-10}(T_g/298)^{-0.50}\exp(-74453/T_g)$	[19]	
R88	$NH_2 + N$	$\rightarrow$	$NH + NH$	$2.99 \times 10^{-13}\exp(-7600/T_g)$	[21]	
R89	$NH_2 + NH_2$	$\rightarrow$	$NH_3 + NH$	$5.07 \times 10^{-15}(T_g/298)^{-3.53}\exp(-278/T_g)$	[22]	
R90	$NH_3 + NH$	$\rightarrow$	$NH_2 + NH_2$	$2.33 \times 10^{-14}(T_g/298)^{-3.41}\exp(-7350/T_g)$	[22]	
R91	$H_2 + H$	$\rightarrow$	$H + H + H$	$2.54 \times 10^{-8}(T_g/298)^{-0.10}\exp(-52561/T_g)$	[23]	
R92	$H_2 + N_2$	$\rightarrow$	$H + H + N_2$	$2.61 \times 10^{-8}(T_g/298)^{-1.40}\exp(-52561/T_g)$	[23]	
R93	$H_2 + H_2$	$\rightarrow$	$H + H + H_2$	$2.61 \times 10^{-8}(T_g/298)^{-0.70}\exp(-52561/T_g)$	[23]	
R94	$NH + M$	$\rightarrow$	$H + N + M$	$2.99 \times 10^{-10}\exp(-37647/T_g)$	[24]	
R95	$NH_2 + M$	$\rightarrow$	$H + NH + M$	$1.99 \times 10^{-9}\exp(-38248/T_g)$	[24]	
R96	$NH_3 + M$	$\rightarrow$	$H + NH_2 + M$	$4.17 \times 10^{-8}\exp(-47149/T_g)$	[25]	[6]
R97	$NH_3 + M$	$\rightarrow$	$H_2 + NH + M$	$1.05 \times 10^{-9}\exp(-47029/T_g)$	[25]	[6]

Three-body collisions

R98	$N + N + M$	$\rightarrow$	$N_2 + M$	$1.38 \times 10^{-33}\exp(502.978/T_g)$	[26]	[2]

R99	$N + N + N$	$\rightarrow$	$N_2(A^3) + N$	1.0×10^{-32}	[11]	
R100	$N + N + N$	$\rightarrow$	$N_2(B^3) + N$	1.4×10^{-32}	[11]	
R101	$N + N + N_2$	$\rightarrow$	$N_2(A^3) + N_2$	1.7×10^{-33}	[11]	
R102	$N + N + N_2$	$\rightarrow$	$N_2(B^3) + N_2$	2.4×10^{-33}	[11]	
R103	$N + N + H_2$	$\rightarrow$	$N_2 + H_2$	$(1/380) \times 8.3 \times 10^{-34} \exp(500/T_g)$	[18]	[7]
R104	$H + H + N_2$	$\rightarrow$	$H_2 + N_2$	$(1/380) \times 8.3 \times 10^{-33}(300/T_g)$	[18]	[7]
R105	$H + N + M$	$\rightarrow$	$NH + M$	$(1/380) \times 1.0 \times 10^{-33}$	[18]	[7,8]
R106	$N + H_2 + M$	$\rightarrow$	$NH_2 + M$	$(1/380) \times 1.0 \times 10^{-34}$	[18]	[7,8]
R107	$H + NH + M$	$\rightarrow$	$NH_2 + M$	$(1/380) \times 1.0 \times 10^{-32}$	[18]	[7,8]
R108	$H + NH_2 + M$	$\rightarrow$	$NH_3 + M$	$(1/380) \times 5.5 \times 10^{-30}$	[18]	[7,8]
R109	$NH + H_2 + M$	$\rightarrow$	$NH_3 + M$	$(1/380) \times 2.5 \times 10^{-35}(T_g/300) \exp(1700/T_g)$	[18]	[7,8]
R110	$N + N + H_2$	$\rightarrow$	$N_2(A^3) + H_2$	$(1/380) \times 1.7 \times 10^{-33}$	[18]	[7]
R111	$N + N + H$	$\rightarrow$	$N_2(A^3) + H$	$(1/380) \times 1.0 \times 10^{-32}$	[18]	[7]
R112	$N + N + H_2$	$\rightarrow$	$N_2(B^3) + H_2$	$(1/380) \times 2.4 \times 10^{-33}$	[18]	[7]
R113	$N + N + H$	$\rightarrow$	$N_2(B^3) + H$	$(1/380) \times 1.4 \times 10^{-32}$	[18]	[7]
R114	$H + H + H_2$	$\rightarrow$	$H_2 + H_2$	$(1/380) \times 8.8 \times 10^{-33}(300/T_g)^{0.6}$	[18]	[7]

Ionization processes

R115	$N + N$	$\rightarrow$	$e^- + N_2^+$	$2.7 \times 10^{-11} \exp(-67400/T_g)$	[11]
R116	$N_2(a'^1) + N_2(a'^1)$	$\rightarrow$	$e^- + N_2^+ + N_2$	5.0×10^{-13}	[17]
R117	$N_2(a'^1) + N_2(a'^1)$	$\rightarrow$	$e^- + N_4^+$	1.0×10^{-11}	[11]
R118	$N_2(a'^1) + N_2(a'^1)$	$\rightarrow$	$e^- + N_4^+$	4.0×10^{-12}	[11]
R119	$N_2(A^3) + N_2(a'^1)$	$\rightarrow$	$e^- + N_2^+ + N_2$	1.0×10^{-12}	[17]

Radiative decay

R120	$N_2(A^3)$	$\rightarrow$	N_2	0.5	[11]
R121	$N_2(B^3)$	$\rightarrow$	$N_2(A^3)$	1.34×10^5	[11]
R122	$N_2(a'^1)$	$\rightarrow$	N_2	1.0×10^2	[11]
R123	$N_2(C^3)$	$\rightarrow$	$N_2(B^3)$	2.45×10^7	[11]

[1] The rate coefficient is scaled according to the Fridmann-Macheret alpha-model[27] with $\alpha = 1$.[16]

[2] The third body, M, is any neutrally charged gas phase species.

[3] R65, R66 and R67, are adopted from reference 18, however the product channel R65 can be considered very unlikely, as also reflected by the rate coefficients.

[4] A more likely reaction channel is $NH + NH_2 \rightarrow N_2H_2 + H$, however the N_2H_2 species is not described in our model.

[5] The reaction only occurs for the vibrational levels.[18] The reported rate coefficient is scaled according to the Fridmann-Macheret alpha-model[27] with $\alpha = 0.3$.[18]

[6] The adopted rate coefficients of R96 and R97 are related by $k_{R96}/k_{R97} \approx 40$, following the recommendations of Hanson et al.[25]

[7] The rate coefficients of the three-body collisions are multiplied by $(1/380)$ to account for the reaction taking place at atmospheric pressure,[28] opposed to low pressure.[18]

[8] The third body, M, is $N_2(X)$, $N_2(V)$, $H_2(X)$ or $H_2(V)$.

Table S3. Ion-neutral collisions describing the plasma kinetics. The ground state and vibrational levels are indicated with X and V, respectively. The effective ion temperature T_{ion} [11] is given in Kelvin.

#	Reaction	Rate coefficient	Ref.
	Ion-neutral collisions		
R124	$N^+ + H_2 \rightarrow NH^+ + H$	5.0×10^{-10}	[29]
R125	$N^+ + NH_3 \rightarrow NH_2^+ + NH$	$0.20 \times 2.35 \times 10^{-9}$	[29]
R126	$N^+ + NH_3 \rightarrow NH_3^+ + N$	$0.71 \times 2.35 \times 10^{-9}$	[29]
R127	$N^+ + NH_3 \rightarrow N_2H^+ + H_2$	$0.09 \times 2.35 \times 10^{-9}$	[29]
R128	$N_2^+ + N \rightarrow N^+ + N_2$	$7.2 \times 10^{-13}(T_{ion}/300)$	[11]
R129	$N_2^+ + H_2 \rightarrow N_2H^+ + H$	2.00×10^{-9}	[10]
R130	$N_2^+ + N_2(A^3) \rightarrow N_3^+ + N$	3.0×10^{-10}	[30]
R131	$N_2^+ + NH_3 \rightarrow NH_3^+ + N_2$	1.95×10^{-9}	[10]
R132	$N_3^+ + N \rightarrow N_2^+ + N_2$	6.6×10^{-11}	[11]
R133	$N_4^+ + N \rightarrow N^+ + N_2 + N_2$	1.0×10^{-11}	[11]
R134	$N_4^+ + N_2 \rightarrow N_2^+ + N_2 + N_2$	$2.1 \times 10^{-16} \exp(T_{ion}/121)$	[11]
R135	$H^+ + NH_3 \rightarrow NH_3^+ + H$	5.20×10^{-9}	[29]
R136	$H_2^+ + H \rightarrow H^+ + H_2$	6.4×10^{-10}	[10]
R137	$H_2^+ + H_2 \rightarrow H_3^+ + H$	2.0×10^{-9}	[10]
R138	$H_2^+ + N_2 \rightarrow N_2H^+ + H$	2.00×10^{-9}	[29]
R139	$H_2^+ + NH_3 \rightarrow NH_3^+ + H_2$	5.70×10^{-9}	[29]
R140	$NH^+ + H_2 \rightarrow H_3^+ + N$	$0.15 \times 1.23 \times 10^{-9}$	[29]
R141	$NH^+ + H_2 \rightarrow NH_2^+ + H$	$0.85 \times 1.23 \times 10^{-9}$	[29]
R142	$NH^+ + NH_3 \rightarrow NH_3^+ + NH$	$0.75 \times 2.40 \times 10^{-9}$	[29]
R143	$NH^+ + NH_3 \rightarrow NH_4^+ + N$	$0.25 \times 2.40 \times 10^{-9}$	[29]
R144	$NH^+ + N_2 \rightarrow N_2H^+ + N$	6.50×10^{-10}	[29]
R145	$NH_2^+ + H_2 \rightarrow NH_3^+ + H$	1.95×10^{-10}	[29]
R146	$NH_2^+ + NH_3 \rightarrow NH_3^+ + NH_2$	$0.5 \times 2.30 \times 10^{-9}$	[29]
R147	$NH_2^+ + NH_3 \rightarrow NH_4^+ + NH$	$0.5 \times 2.30 \times 10^{-9}$	[29]
R148	$NH_3^+ + NH_3 \rightarrow NH_4^+ + NH_2$	2.10×10^{-9}	[29]
R149	$N_2H^+ + NH_3 \rightarrow NH_4^+ + N_2$	2.3×10^{-9}	[29]
	Ion-neutral three-body collisions		
R150	$N_2^+ + N + N_2 \rightarrow N_3^+ + N_2$	$9.0 \times 10^{-30} \exp(400/T_{ion})$	[11]
R151	$N^+ + N_2 + N_2(X,V) \rightarrow N_3^+ + N_2$	$1.7 \times 10^{-29}(300/T_{ion})^{2.1}$	[11]
R152	$N_2^+ + N_2 + N_2(X,V) \rightarrow N_4^+ + N_2$	$5.2 \times 10^{-29}(300/T_{ion})^{2.2}$	[11]
R153	$N^+ + N + N_2 \rightarrow N_2^+ + N_2$	1.0×10^{-29}	[11]

Table S4. Negative-positive ion recombination reactions describing the plasma kinetics. The ground state and vibrational levels are indicated with X and V, respectively. The temperatures are given in Kelvin.

#	Reaction	Rate coefficient	Ref.
	H⁻ recombination		
R154	$H^- + H_2^+ \rightarrow H + H + H$	$2.0 \times 10^{-7}(300/T_g)$	[18]
R155	$H^- + H_3^+ \rightarrow H_2 + H + H$	$2.0 \times 10^{-7}(300/T_g)$	[18]
R156	$H^- + N_2^+ \rightarrow N_2 + H$	$2.0 \times 10^{-7}(300/T_g)$	[18]
R157	$H^- + N_4^+ \rightarrow N_2 + N_2 + H$	$2.0 \times 10^{-7}(300/T_g)$	[18]
R158	$H^- + N_2H^+ \rightarrow H_2 + N_2$	$2.0 \times 10^{-7}(300/T_g)$	[18]
	H⁻ three-body recombination		
R159	$H^- + H_2^+ + M \rightarrow H_2 + H + N_2$	$(1/380) \times 2 \times 10^{-25}(300/T_g)^{2.5}$	[18] [1,2]
R160	$H^- + H_3^+ + M \rightarrow H_2 + H_2 + M$	$(1/380) \times 2 \times 10^{-25}(300/T_g)^{2.5}$	[18] [1,2]
R161	$H^- + N_2^+ + M \rightarrow N_2 + H + M$	$(1/380) \times 2 \times 10^{-25}(300/T_g)^{2.5}$	[18] [1,2]
R162	$H^- + N_4^+ + M \rightarrow N_2 + N_2 + H + M$	$(1/380) \times 2 \times 10^{-25}(300/T_g)^{2.5}$	[18] [1,2]
R163	$H^- + N_2H^+ + M \rightarrow H_2 + N_2 + M$	$(1/380) \times 2 \times 10^{-25}(300/T_g)^{2.5}$	[18] [1,2]

[1] The rate coefficients of the three-body collisions are multiplied by (1⁄380) to account for the reaction taking place at atmospheric pressure,[28] opposed to low pressure.[18]
[2] The third body, M, is $N_2(X)$, $N_2(V)$, $H_2(X)$ or $H_2(V)$.

Table S5. Vibrational processes describing the plasma kinetics. The calculations of the rate coefficients can be found in the listed references.

#	Reaction		Ref.
	Excitation and de-excitation		
R164	$e + N_2(v) \leftrightarrow N_2(v' > v) + e$	$v = 1 \ldots 24$	[15]
R165	$e + H_2(v) \leftrightarrow H_2(v' > v) + e$	$v = 1 \ldots 14$	[31,32]
	Vibrational-translational relaxation		
R166	$N_2(v) + N \leftrightarrow N_2(v' < v) + N$	$v = 1 \ldots 24$	[33]
R167	$N_2(v) + N_2 \leftrightarrow N_2(v-1) + N_2$	$v = 1 \ldots 24$	[34]
R168	$H_2(v) + H_2 \leftrightarrow H_2(v-1) + H_2$	$v = 1 \ldots 14$	[11]
R169	$H_2(v) + H \leftrightarrow H_2(v-1) + H$	$v = 1 \ldots 14$	[18] [1]
R170	$H_2(v) + H \leftrightarrow H_2 + H$	$v = 1 \ldots 14$	[18] [1]
R171	$N_2(v) + H_2 \leftrightarrow N_2(v-1) + H_2$	$v = 1 \ldots 24$	[18]
R172	$N_2(v) + H \leftrightarrow N_2(v-1) + H$	$v = 1 \ldots 24$	[18] [1]
R173	$N_2(v) + H \leftrightarrow N_2 + H$	$v = 1 \ldots 24$	[18] [1]
	Vibrational-vibrational relaxation		
R174	$N_2(v+1) + N_2(w) \leftrightarrow N_2(v) + N_2(w+1)$	$v = 1 \ldots 24, w < v$	[34]
R175	$H_2(v+1) + H_2(w) \leftrightarrow H_2(v) + H_2(w+1)$	$v = 1 \ldots 14, w < v$	[11]
R176	$H_2(v) + N_2(w-1) \leftrightarrow H_2(v-1) + N_2(w)$	$v = 1 \ldots 14, w = 1 \ldots 24$	[18]
R177	$N_2(v) + H_2(w-1) \leftrightarrow N_2(v-2) + H_2(w)$	$v = 2 \ldots 24, w = 1 \ldots 24$	[18]

[1] Only the single quantum processes are included separately (R156 and R159), the multi quantum processes are included by an effective sum (R157 and R160).

Table S6. Surface reactions included in the plasma kinetics model. The ground state, vibrational levels and electronically excited states are indicated with X, V and E, respectively. The sticking coefficients, γ, diffusion energy barrier, E_d, and the activation energy, E_a, are given. For the rate coefficient expressions we refer to [3].

#	Reaction			Ref.
	Wall relaxation			
R178	$N_2(A^3)$	$\rightarrow$	N_2	$\gamma = 1 \times 10^{-3}$ [18]
R179	$N_2(A^1)$	$\rightarrow$	$N_2(B^3)$	$\gamma = 1 \times 10^{-3}$ [18]
R180	$H_2(E)$	$\rightarrow$	H_2	$\gamma = 1 \times 10^{-3}$ [18]
R181	$N_2(V)$	$\rightarrow$	$N_2(V-1)$	$\gamma = 4.5 \times 10^{-4}$ [18]
R182	$H_2(V)$	$\rightarrow$	$H_2(V-1)$	$\gamma = 1 \times 10^{-4}$ [18]
	Direct adsorption			
R183	$N(X, E) + Surface$	$\rightarrow$	$N(s)$	$\gamma = 1$ [10]
R184	$H + Surface$	$\rightarrow$	$H(s)$	$\gamma = 1$ [10]
R185	$NH + Surface$	$\rightarrow$	$NH(s)$	$\gamma = 1$ [10]
R186	$NH_2 + Surface$	$\rightarrow$	$NH_2(s)$	$\gamma = 1$ [10]
	Eley-Rideal			
R187	$N(X, E) + N(s)$	$\rightarrow$	N_2	$\gamma = 6 \times 10^{-3}$ [10]
R188	$H + H(s)$	$\rightarrow$	H_2	$\gamma = 1.5 \times 10^{-3}$ [10]
R189	$N(X, E) + H(s)$	$\rightarrow$	$NH(s)$	$\gamma = 1 \times 10^{-2}$ [10]
R190	$NH + H(s)$	$\rightarrow$	$NH_2(s)$	$\gamma = 1 \times 10^{-2}$ [10]
R191	$H + N(s)$	$\rightarrow$	$NH(s)$	$\gamma = 8 \times 10^{-3}$ [10]
R192	$H + NH(s)$	$\rightarrow$	$NH_2(s)$	$\gamma = 8 \times 10^{-3}$ [10]
	Eley-Rideal: NH$_3$ formation			
R193	$NH_2 + H(s)$	$\rightarrow$	NH_3	$\gamma = 1 \times 10^{-2}$ [10]
R194	$H + NH_2(s)$	$\rightarrow$	NH_3	$\gamma = 8 \times 10^{-3}$ [10]
R195	$H_2(X, V) + NH(s)$	$\rightarrow$	NH_3	$\gamma = 8 \times 10^{-4}$ [10]
	Langmuir-Hinshelwood			
R196	$N(s) + H(s)$	$\rightarrow$	$NH(s)$	$E_a = 1.099$ eV, $E_d = 0.2$ eV [28]
R197	$NH(s) + H(s)$	$\rightarrow$	$NH_2(s)$	$E_a = 0.3$ eV, $E_d = 0.2$ eV [10]
R198	$NH_2(s) + H(s)$	$\rightarrow$	NH_3	$E_a = 0.2$ eV, $E_d = 0.2$ eV [10]
	Dissociative adsorption			
R199	$N_2(X, V) + Surface$	$\rightarrow$	$N(s) + N(s)$	See references [35,36]
R200	$N_2(E) + Surface$	$\rightarrow$	$N(s) + N(s)$	$\gamma = 1 \times 10^{-1}$ [28]
R201	$H_2(X) + Surface$	$\rightarrow$	$H(s) + H(s)$	$\gamma = 1 \times 10^{-3}$ [28]
R202	$H_2(v = 1) + Surface$	$\rightarrow$	$H(s) + H(s)$	$\gamma = 1 \times 10^{-2}$ [28]
R203	$H_2(v = 2) + Surface$	$\rightarrow$	$H(s) + H(s)$	$\gamma = 5 \times 10^{-2}$ [28]
R204	$H_2(v \geq 3) + Surface$	$\rightarrow$	$H(s) + H(s)$	$\gamma = 1 \times 10^{-1}$ [28]
R205	$H_2(E) + Surface$	$\rightarrow$	$H(s) + H(s)$	$\gamma = 1$ [28]

The sticking coefficients (γ) for the wall relaxation of the vibrationally excited molecules were adopted from Gordiets et al.[18] The authors assumed $\gamma = 4.5 \times 10^{-4}$ for $N_2(V)$ (Reaction R181) based on Black et al., who performed a detailed study on the deactivation coefficient of $N_2(V=1)$ upon collisions with various surfaces, including stainless steel.[37] The value of $\gamma = 1 \times 10^{-4}$ for $H_2(V)$ (R182) is based on Heidner et al., who considered multiple de-excitation channels in flow tube experiments.[38] The relaxation of $N_2(E)$ (specifically metastable N_2, R178 and R179) was estimated by Gordiets et al. upon comparison between their predictions and experiments.[18] Relaxation of $H_2(E)$ (R180) is assumed equal, after Hong et al.[28]

Direct adsorption sticking coefficients (R183-R186) are adopted from Carrasco et al. who selected $\gamma = 1$ as a generally high value representing transition metals [10].

The Eley-Rideal (ER) sticking probability of $\gamma = 1.5 \times 10^{-3}$ between H and H(s) (R188) was adopted from Carrasco et al. who used the value yielding best agreement in their earlier experimental study, in which the apparatus had stainless steel walls.[10,39] The value of $\gamma = 6 \times 10^{-3}$ for N_2 (R187) was estimated by Carrasco et al.[10] The remaining sticking probabilities of ER type reactions (R189-R195) were adopted from the same study, where the values were chosen based on agreement with experimental data, due to a lack of reported values. Specifically, the ER reaction with H_2 as the gas phase reactant (R195) was chosen as significantly lower (order of magnitude 10^{-4} compared to $10^{-2} \dots 10^{-3}$). Note that Hong et al. report three unique sets of sticking probabilities for three types of surfaces (aluminium oxide, nanodiamond coated alumina and metal).[28]

The diffusion energy barrier of 0.2 eV for Langmuir-Hinshelwood (LH) type reactions (R196-R198) is adopted from Carrasco et al. who assumed this value based on the typical characteristics of chemisorbed H atoms on Fe.[10,28,40] The activation barrier for $NH_2(s)$ formation (R197) was taken as 0.3 eV based on detailed surface kinetics studies,[41,42] while for the production of NH_3, a barrier of 0.2 eV was adopted.[10] For the elementary LH step between N(s) and H(s) (R196), an activation energy of 1.099 eV is used, after Hong et al.[28,41] They used the H atom diffusion barrier because the N atom diffusion barrier was reported as significantly higher (0.9 eV compared to 0.2 eV).[28]

The sticking coefficients for N_2 dissociative adsorption (R199) are resolved for the vibrational levels based on the studies by Hansen et al. Their calculations generally represent metallic surfaces.[35,36] The sticking probabilities of the dissociative adsorption of electronically excited N_2 and all H_2 molecules (R200-R205) were adopted from Hong et al., following their assumptions.[28] We assumed their $H_2(v = 3)$ sticking probability also for any higher level (R204).

From the above, it is clear that the surface kinetics are subject to many assumptions and thus also to uncertainties. That includes the exact surface described. We summarize the above as a metal surface, most representative of iron, merely for reference and context. Indeed the exact surface characteristics, such as step or surface sites, are not captured. This would require a more detailed model, such as micro-kinetics models.[43–45] This type of model uses surface reaction rates derived from density functional theory calculations and generally

solves those reaction rates in steady state conditions and does not include a full gas phase chemistry. To our knowledge, such micro-kinetics models have not yet been combined with a full time dependent plasma kinetics model. The present study, albeit with a less accurate surface description, focusses mainly on giving novel insight in the temporal discharge behaviour (i.e. the role of the micro-discharges and their afterglows). This study thus allows to better demarcate future studies, considering the increased number of degrees of freedom in a combined model (i.e. surface kinetics + plasma kinetics, introducing the exact surface, described by the surface binding energy).[43]

Nevertheless, the surface kinetics without radical-surface interactions (i.e. without radical adsorption and ER reactions) in our model provided similar NH_3 turnover frequencies as Mehta et al.[44] Indeed, our steady state NH_3 turnover frequencies are calculated to be 1.39×10^{-8} s^{-1} and 1.44×10^{-8} s^{-1} when vibrational dissociative adsorption is neglected and included, respectively. Considering that our surface kinetics are an approximation, we believe that this turnover frequency of 10^{-8} s^{-1} is in good agreement with the left side of the volcano plots by Mehta et al. (see figure S1: our results are indicated with a red dot).
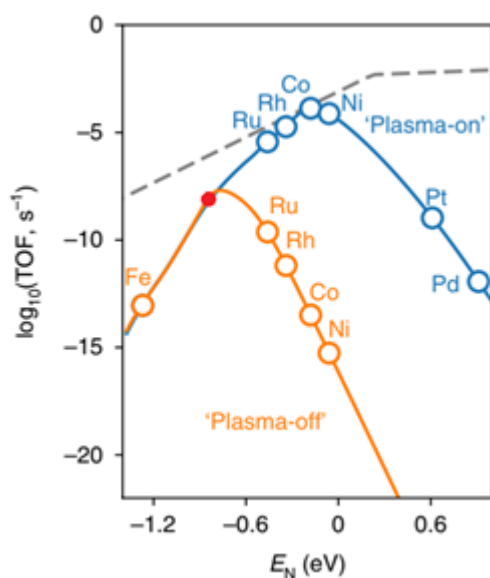

Figure S1. Comparison of our calculated turnover frequency (red dot) against the volcano curves of Mehta et al. Adapted by permission from Springer Nature: Nature Catalysis, Overcoming ammonia synthesis scaling relations with plasma-enabled catalysis, Mehta et al, 2018.

S.1.2. Translation of Experimentally Measured Current and Voltage Characteristics to the Model Conditions

We measured the charge-voltage characteristics, i.e. Lissajous figures, to (1) calculate the actual plasma current and gas voltage from the measured current and applied voltage, and (2) determine the partial discharging [46]. The Lissajous figures of the N_2/H_2 plasma are given in figure S2(a). In addition, in figure S2(b), the Lissajous figure for a measurement in pure argon is plotted, for which it is assumed that the plasma reactor is fully discharging [47]. With those figures, we can determine the dissipated plasma power, P_{diss}, and the partial discharging factor, β, using the following equations [46].

$$P_{diss} = W f_D \tag{S1}$$

$$W = 2U_b \Delta Q_D \tag{S2}$$

$$\Delta Q_D = \frac{Q_0}{1 - C_{cell}/C_{diel}} \tag{S3}$$

$$U_b = \left(1 + \frac{\alpha}{\beta} \frac{C_{cell}}{C_{diel}}\right) \Delta U \tag{S4}$$

$$\alpha + \beta = 1 \tag{S5}$$

$$\alpha = \frac{C_{diel} - \zeta_{diel}}{C_{diel} - C_{cell}} \tag{S6}$$

where W is the work done by the plasma, f_D is the discharge frequency, U_b is the burning voltage, ΔQ_D is the charge transferred by the discharge, Q_0 is the measured charge transferred, ΔU is the measured burning voltage, C_{diel} is the capacitance of the dielectric, C_{cell} is the capacitance of the reactor and ζ_{diel} is the effective dielectric capacitance.
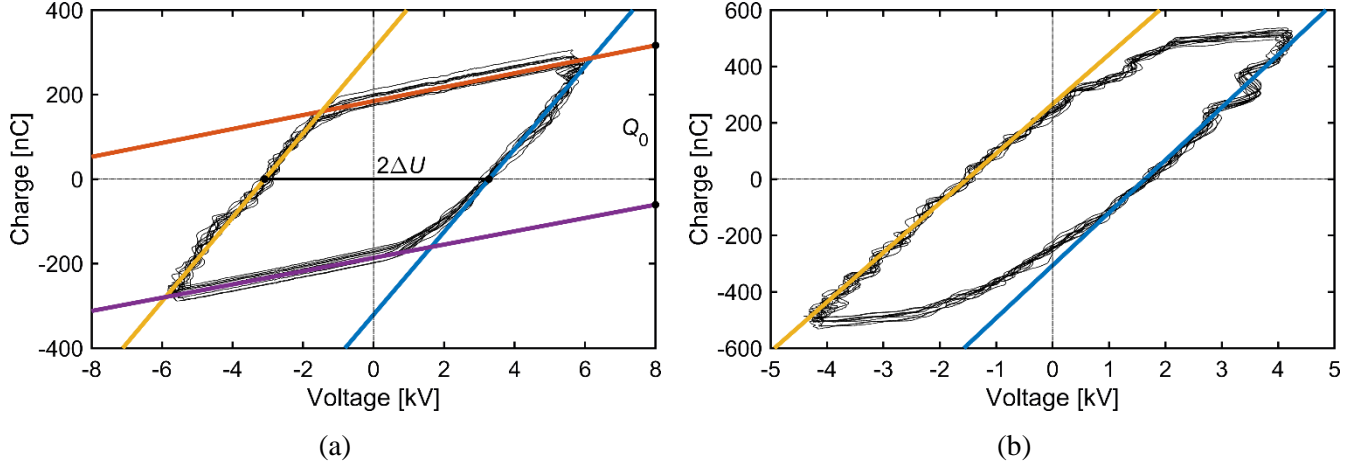
Figure S2. Lissajous figure measured in our PB DBD and a 1:3 N_2:H_2 gas mixture (a) and operated with argon only (b). From those measurements, $\Delta U = 3066.7$ V and $Q_0 = 385.72$ nC are determined (a). The capacitances $\zeta_{diel} = 88.87$ pF and $C_{cell} = 16.468$ pF are determined from the two steepest and the two slighter slopes in (a), respectively. In addition $C_{diel} = 181.28$ pF is determined according to the plotted slopes in (b).

The plasma current i_{plasma} and gas voltage U_{gas} are given in figure S3, calculated with [46]

$$i_{plasma}(t) = \frac{1}{1 - C_{cell}/C_{diel}} \left[\frac{dQ(t)}{dt} - C_{cell} \frac{dV(t)}{dt} \right] \tag{S7}$$

$$U_{gas}(t) = \left(1 + \frac{\alpha}{\beta} \frac{C_{cell}}{C_{diel}} \right) V(t) - \frac{1}{\beta C_{diel}} Q(t) \tag{S8}$$
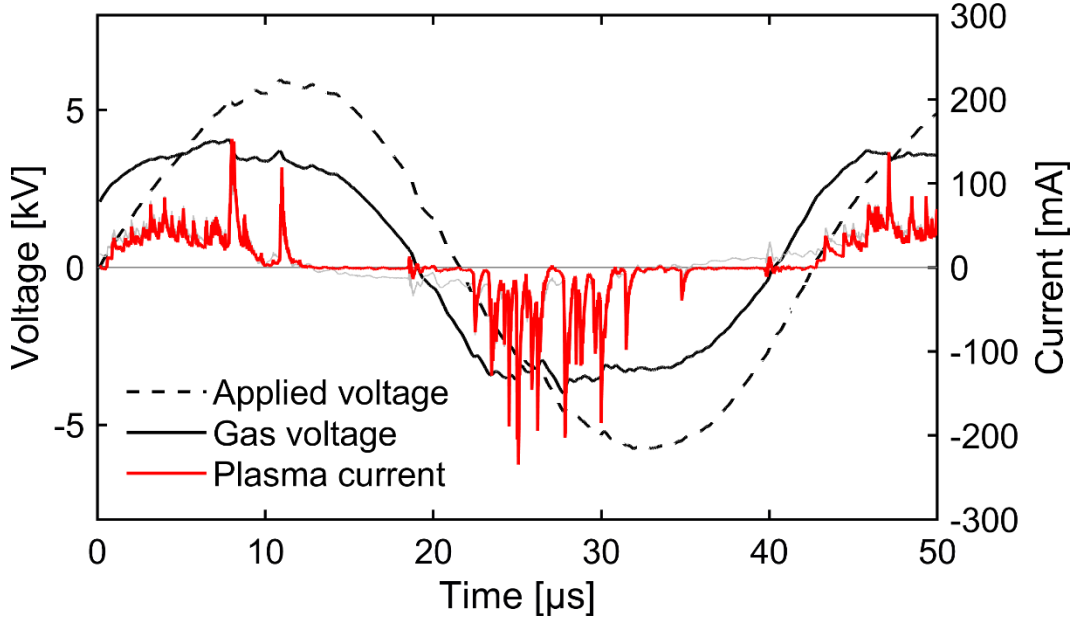

Figure S3. Plasma current and gas voltage, as well as the actual applied voltage, in our PB DBD and a 1:3 N_2:H_2 gas mixture.

The plasma current and gas voltage are used to calculate the instantaneous plasma power, which is shown in figure S4. Based on this figure (black line), we defined the average life-time of the micro-discharges as 200 ns (100 ns at FWHM), and we assume 25 micro-discharge per discharge half cycle.
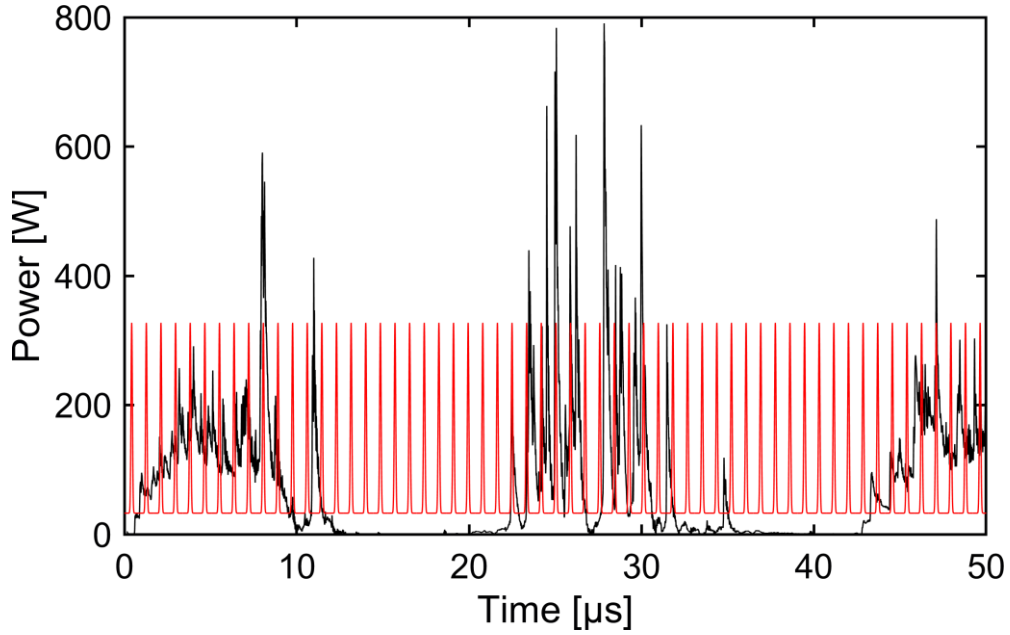
Figure S4. Instantaneous plasma power measured in our PB DBD and a 1:3 N_2:H_2 gas mixture, as well as the model representation of the instantaneous plasma power (red line).

The average instantaneous maximum power, i.e., if all micro-discharge peaks would be of the same height, is given by [3]

$$P_{max} = \frac{P_{diss}}{(1-\gamma)N_{MD}f_D\tau_{MD} + \gamma} \tag{S9}$$

$$P_{min} = \gamma P_{max}, \qquad \gamma \in [0,1] \tag{S10}$$

Where N_{MD} is the number of micro-discharges per discharge half cycle, f_D is the discharge frequency, τ_{MD} is the micro-discharge life-time, P_{max} and P_{min} are the average instantaneous maximum and minimum power, respectively, and γ is a distribution factor which defines the eventual minimum and maximum instantaneous power and power density (see section S.1.3 below). Table S7 summarizes all parameters introduced in section S.1.2, together with the values assumed in our model of the most relevant parameters.

Table S7. Summary of the parameters explained in section S.1.2.

Symbol	Description	Determination	Value	Units
P_{diss}	Average dissipated plasma power	Eq. S1	68	W
W	Work done by the plasma	Eq. S2		
f_D	Discharge frequency	Experiments	23.5	kHz
U_b	Burning voltage	Eq. S4		
ΔQ_D	Charge transferred by the discharge	Eq. S3		
Q_0	ΔQ_D, as measured	Figure S2(a)		
C_{cell}	Capacitance of the reactor	Figure S2(a)		
C_{diel}	Capacitance of the dielectric	Figure S2(b)		
α	Non-discharging fraction	Eq. S6		
β	Partial discharging fraction	Eq. S5	0.44	
ΔU	U_b, as measured	Figure S2(a)		
ζ_{diel}	Effective dielectric capacitance	Figure S2(a)		
N_{MD}	Number of micro-discharges per discharge half cycle	Figure S4	25	
τ_{MD}	Micro-discharge life time	Figure S4	200	ns
γ	Power distribution factor	Chosen	0.1	
P_{max}	Average maximum instantaneous power	Eq. S9	332	W
P_{min}	Average minimum instantaneous power	Eq. S10	33	W

It should be noted that the distribution factor, γ, is different from the definition in our previous work, in which we did not consider the experimentally measured instantaneous plasma power. With the more direct translation of the experimental current and voltage characteristics, we found that the relevant order of magnitude of the distribution factor is now in the range between 0.1 and 1, instead of between 10^{-6} and 1 as in our previous work [3]. We chose $\gamma = 0.1$, such that P_{max} is in reasonable agreement with the experimental measurement (cf. the red curve in figure S4). Lower γ values would result in very high P_{max}, i.e. 540 W for $\gamma = 0.01$.

Figure S4 represents all the micro-discharges (red line) over a time of 50 μs. In our model we consider an interpulse time of 76.8 ms, because the gas molecules do not feel all the micro-discharges when they travel through the reactor, i.e. we consider the number of micro-discharges of a single discharge period, but distributed over the longer gas residence time.

S.1.3. Relationship Between Instantaneous Power and Power Density: Choice of Discharge Volumes

The model description of the instantaneous power (cf. the red line in figure S4) consists of micro-discharge pulses and a constant, minimum, power value. We assign the latter to a uniform plasma component that is also present in between the micro-discharges. We thus need to define a discharge volume for both the micro-discharges and the uniform plasma. We assign the following volume to the uniform plasma:

$$V_U = \beta(1 - \alpha_{packing})V_R \qquad \text{(S11)}$$

i.e., the uniform discharge volume, V_U, is the reactor volume, V_R, corrected for packing with the packing factor, $\alpha_{packing}$, as well as corrected for partial discharging of the plasma reactor, β. We chose $\alpha_{packing} = 0.68$, i.e. corresponding to a body-centred cubic structure, which is not the most optimal packing, but more likely to occur in practice. Indeed, the hexagonal close-packed structure, with $\alpha_{packing} = 0.74$, i.e. most optimal packing, is assumed to be unlikely. This was based on counting the number of beads in our reactor after the standard preparation procedure (e.g. including a vibrating step to ensure a dense packing). Equation S11 yields a uniform plasma discharge volume of 2.8 cm^3.

Furthermore, we attributed the size of typical voids in the assumed packed bed structure to the discharge volume of individual micro-discharges, such that the micro-discharge volume, V_{MD}, depends on the packing bead radius, r_{bead}

$$V_{MD} = \frac{4}{3}\pi(0.29r_{bead})^3 \qquad \text{(S12)}$$

For a packing bead radius of 0.95 mm, Equation S12 yields a micro-discharge volume of 8.8×10^{-5} cm^3.

Using the above discharge volumes for the micro-discharges and the uniform plasma, we calculate the maximum and minimum power density in the model as 3.4×10^6 and 11.8 W/cm^3, respectively.

S.2. Surface Coverages and Gas Phase Concentrations in the Micro-Discharge
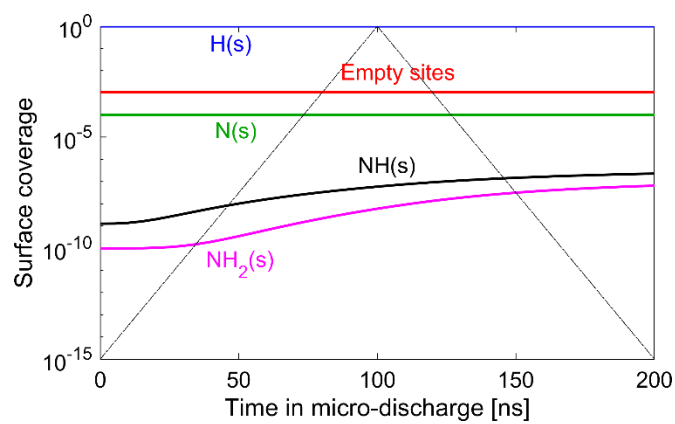
(a)
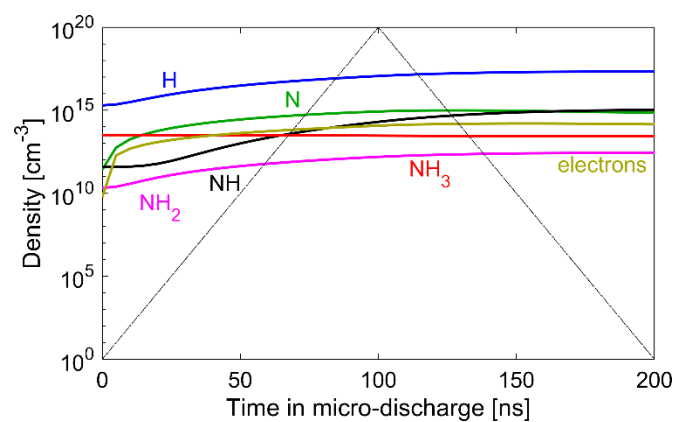
(b)

Figure S5. Surface coverages and fraction of empty surface sites (a), and concentrations of the neutral gas phase species and electrons (b), as a function of time in the first micro-discharge. This figure corresponds to figure 1 in the main paper.

Figure S6. Number densities of the N_2 (solid lines) and H_2 (dashed lines) molecules in the ground state and the sum of the electronically and vibrationally excited states, as a function of time in the first micro-discharge. This figure corresponds to figure 2 in the main paper.

Figure S7. H_2 vibrational distribution function (VDF) at various moments in the micro-discharge, as well as the Boltzmann distribution at the gas temperature (400 K).

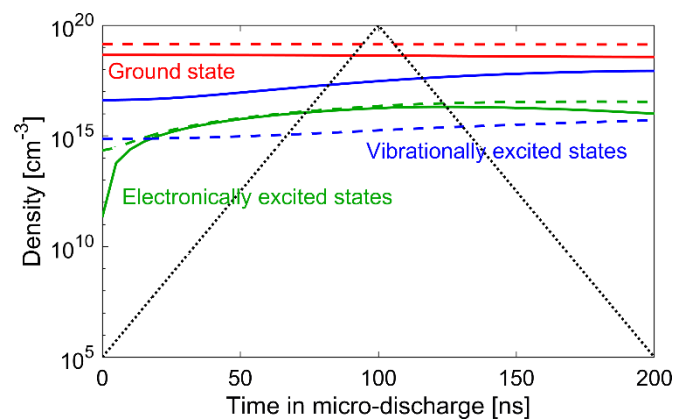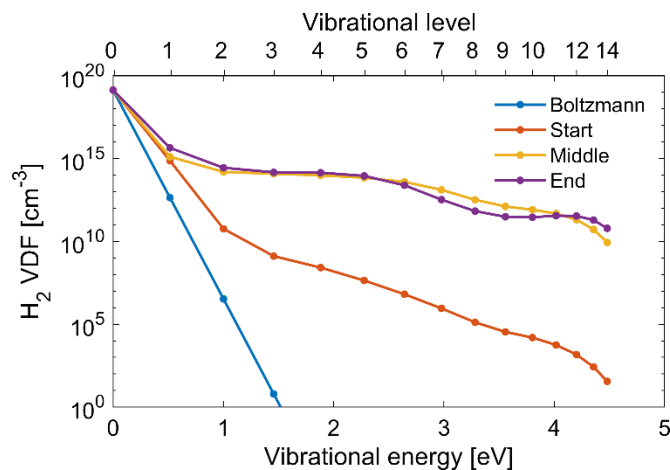Table S8. Typical species densities in cm^{-3} of the various surface adsorbed species and plasma radicals in both the micro-discharge and afterglow. The equivalent coverages are given between brackets.

Species	Micro-discharge (at maximum power density)	Afterglow (end)
$NH_2(s)$	8.6×10^8 (6.0×10^{-9})	6.1×10^6 (4.3×10^{-11})
$NH(s)$	8.5×10^9 (5.9×10^{-8})	3.0×10^7 (2.1×10^{-10})
$H(s)$	1.4×10^{17} (1.0)	1.4×10^{17} (1.0)
$N(s)$	1.5×10^{13} (1.0×10^{-4})	2.4×10^{13} (1.7×10^{-4})
Surface	1.5×10^{14} (1.1×10^{-3})	1.4×10^{14} (9.9×10^{-4})
NH_3	2.9×10^{13}	6.9×10^{14}
NH_2	1.6×10^{12}	1.9×10^{12}
NH	2.0×10^{14}	1.5×10^{11}
H	1.2×10^{17}	1.0×10^{14}
N	8.4×10^{14}	8.1×10^{10}
H_2	1.4×10^{19}	1.4×10^{19}
N_2	4.3×10^{18}	4.6×10^{18}
e^-	1.2×10^{14}	1.2×10^{10}

S.3. Calculated Plasma Parameters

The N_2 vibrational temperature (figure S8(a)) is calculated to be slightly above 2100 K during the micro-discharges, and it relaxes back to above the gas temperature (700 K compared to 400 K) over approximately 1 ms. The H_2 vibrational temperature behaves similarly but reaches lower values, i.e. 600 K and 1100 K in the afterglow and micro-discharge, respectively. Figure S8(b) illustrates the calculated reduced electric field (E/N) and electron temperature (T_e), as a function of time. The maximum E/N was calculated to be 105 Td in each micro-discharge (and the maximum electron temperature was 5.9 eV. After the micro-discharges, both values significantly drop to virtually zero, but then rise again, and reach constant values in the entire afterglows, around E/N = 6 Td and T_e = 0.7 eV.
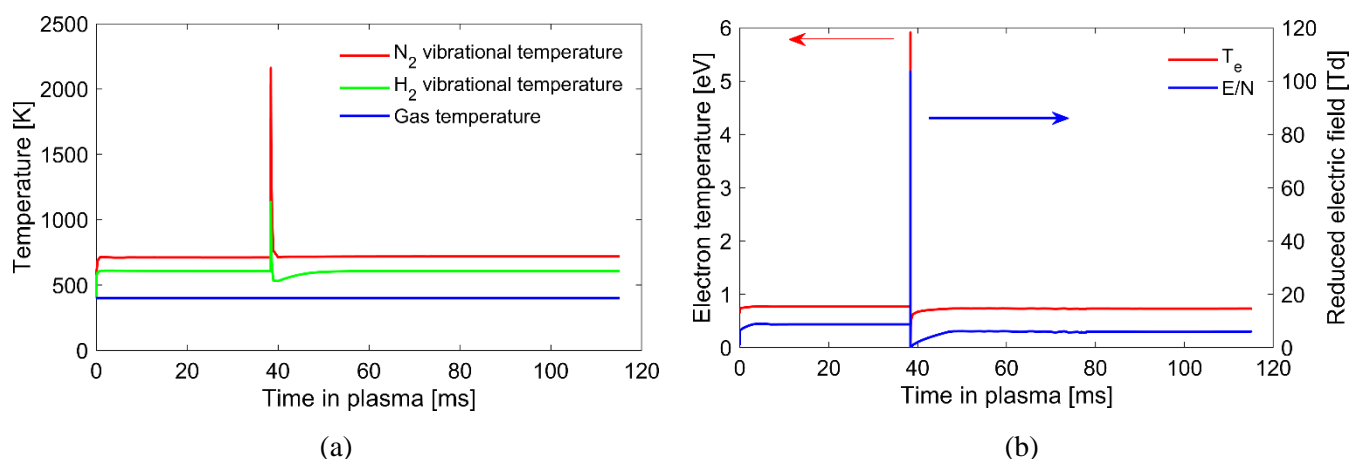
Figure S8. N_2 and H_2 vibrational temperature (a) and reduced electric field and electron temperature (b) as a function of time in the plasma, from the start of the plasma to the end of the first micro-discharge and afterglow pair. The maximum values of the reduced electric field and electron temperature are 105 Td and 5.9 eV, respectively. The micro-discharge with a 200 ns duration takes place at 38.4 ms.

S.4. NH₃ Formation: Detailed Analysis of the Reaction Rates and Determination of the Rate-Limiting Step

Figure S9(a) depicts the actual reaction rates of the main NH_3 (and precursor) formation reactions as a function of time from the start of the plasma until the end of the first afterglow. The main NH_3 formation reaction is the elementary LH step of NH_2(s) with H(s); blue curve. Similarly, NH_2(s) is mainly formed from the LH reaction of NH(s) with H(s); red curve. NH(s), however, is formed from elementary ER steps, either by gas phase N with H(s), or by gas phase H with N(s); black curve in figure S9(a). This process is predominant in the micro-discharges (cf. figure S9(b)). In addition, we also plot the formation rate of NH_2(s) from gas phase NH and H(s) (ER mechanism; green curve), as it is also important in the micro-discharges (cf. figure S9(b)). Similarly, the ER formation of NH_3 by NH_2 and H(s) is also plotted (dark yellow curve), becoming important in the late afterglow.
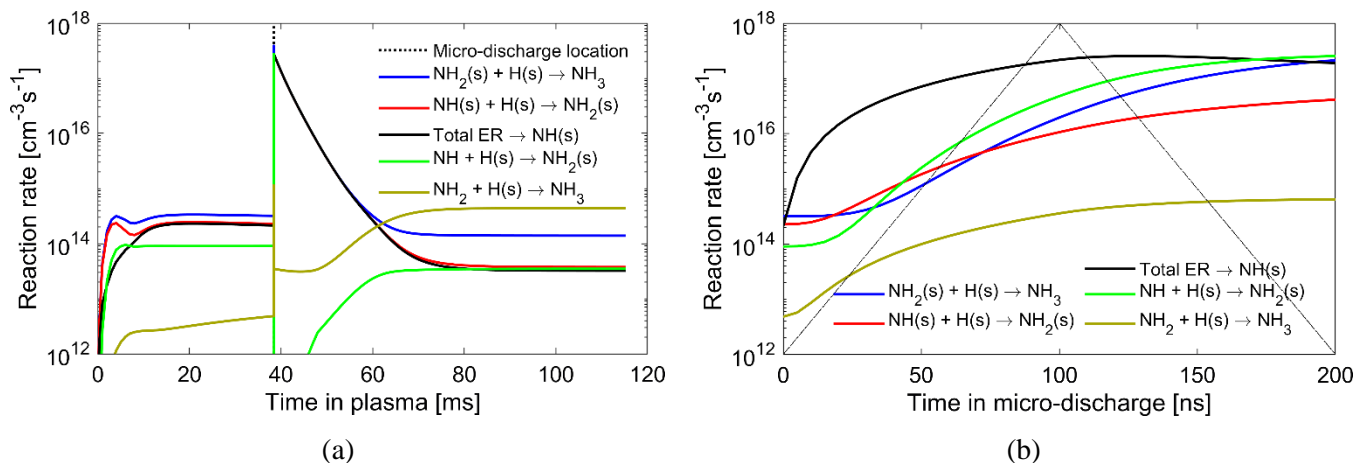
Figure S9. Main reaction rates for the formation of NH_3, $NH_2(s)$ and $NH(s)$ as a function of time in the plasma, from the start of the plasma to the end of the first micro-discharge and afterglow pair (a), and as a function of time in the first micro-discharge (b). "Total ER → NH(s)" stands for the sum of both reactions N + H(s) and H + N(s) reactions. In (a) the blue, red and black curve mostly overlap with each other. In (a), the micro-discharge with a 200 ns duration takes place at 38.4 ms.

Directly after the micro-discharge, we see in figure S9(a) a complete overlap between the reactions forming NH_3, $NH_2(s)$ and $NH(s)$ (blue, red and black curves). This means that the intermediate products, $NH(s)$ and $NH_2(s)$, are immediately converted towards NH_3. During the micro-discharges, there is no overlap between the various reaction rates, and the earlier products are generally formed at a higher rate (black and green curves are higher than blue curve). Note that in addition to the reactions in figure S9(b), NH_3 is net destroyed during the micro-discharges due to electron impact dissociation (cf. figure 2 in the main paper). Towards the end of the afterglow, the NH_3 formation is faster than the $NH_2(s)$ formation, and the latter is slightly faster than $NH(s)$ formation, meaning that both $NH_2(s)$ and $NH(s)$ are slightly being depleted in the afterglow, as discussed in section 3.2 in the main paper.

To find the rate-limiting step, we further investigate the formation of $NH(s)$ in figure S10, where we plot the rates of the individual ER reaction steps as a function of time, again from the start of the plasma until the end of the first afterglow (figure S10(a)) and in the micro-discharge (figure S10(b)). The ER reaction of N with $H(s)$ is generally faster, especially in the micro-discharges, and generally determines the total $NH(s)$ formation, except before the first micro-discharge, where the ER reaction of H with $N(s)$ seems more important. This is attributed to the relatively high dissociation of H_2 at the very beginning (see figure S13 below).

(a)   (b)

Figure S10. Reaction rates for the formation of NH(s) as a function of time in the plasma, from the start of the plasma to the end of the first micro-discharge and afterglow pair (a), and as a function of time in the first micro-discharge (b). In (a), the micro-discharge with a 200 ns duration takes place at 38.4 ms.

Based on figures S9 and S10, we can identify the elementary ER reaction step between N and H(s) as the limiting reaction in NH_3 formation, i.e. N_2 dissociation in the plasma and H_2 or H (dissociative) adsorption are required for this. Similarly, the alternative ER reaction requires N(s). In figure S11, we show that the rate of this reaction overlaps with the direct adsorption of N, shortly after the micro-discharge. Thus, N atoms are required in both NH(s) formation pathways.

(a)   (b)

Figure S11. Reaction rates for the formation and consumption of N(s) as a function of time in the plasma, from the start of the plasma to the end of the first micro-discharge and afterglow pair (a), and as a function of time in the first micro-discharge (b). In (a), the micro-discharge with a 200 ns duration takes place at 38.4 ms.

Unlike N(s), which is only significantly formed by direct adsorption and only reacts further to the desired products (NH(s)), the formation and consumption of H(s) is more complex. In the afterglow, we found that the net H(s) formation rate, attributed to direct adsorption (red curve in figure S12) overlaps in the afterglow with the total H(s) consumption rate to the desired products (blue curve). The contributions of individual processes to the net H(s) formation is given in figure S13.

During the micro-discharges (figure S12(b) and S13(b)), more H(s) is destroyed than formed. Indeed, this is due to the importance of H + H(s) → H₂. The dissociative adsorption (H₂ → 2 H(s)) has the lowest reaction rate once a micro-discharge occurred and the net formation of H₂ is then always higher, this means that the net H(s) formation is not determined by the dissociative adsorption anymore. However, the H(s) coverage is never significantly influenced after the initial coverage, due to the predominant dissociative adsorption before the first micro-discharge, and it is always nearly 1 (cf. figure 1(a) in the main paper and figure S5(a)).

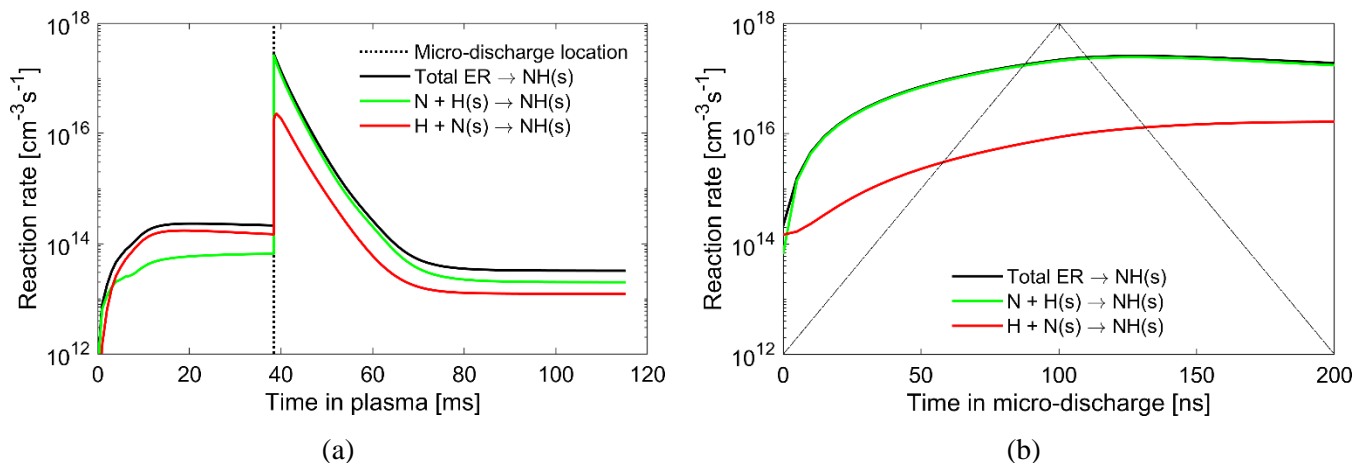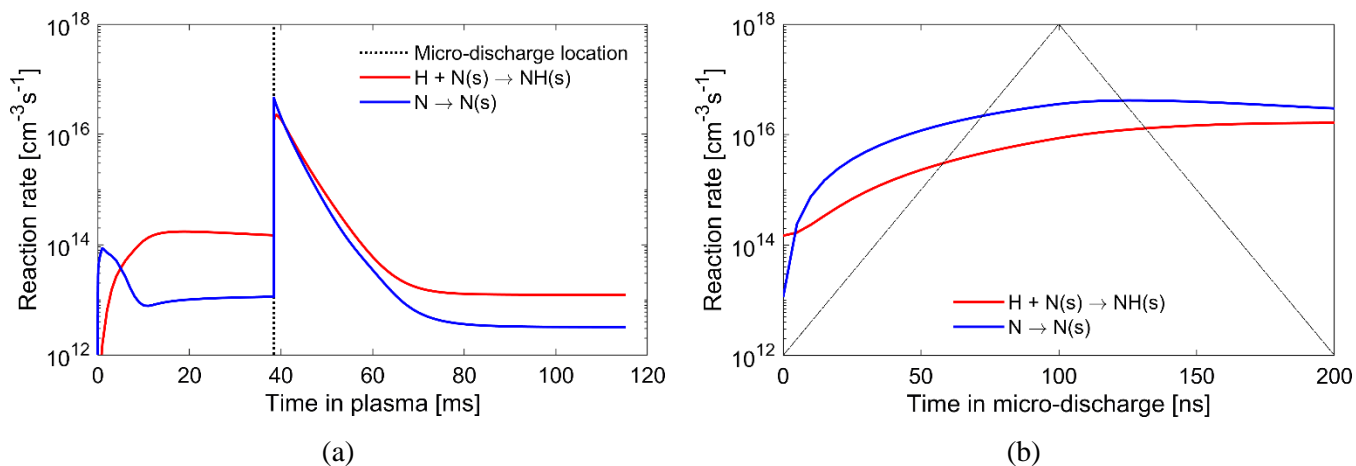
(a)

(b)
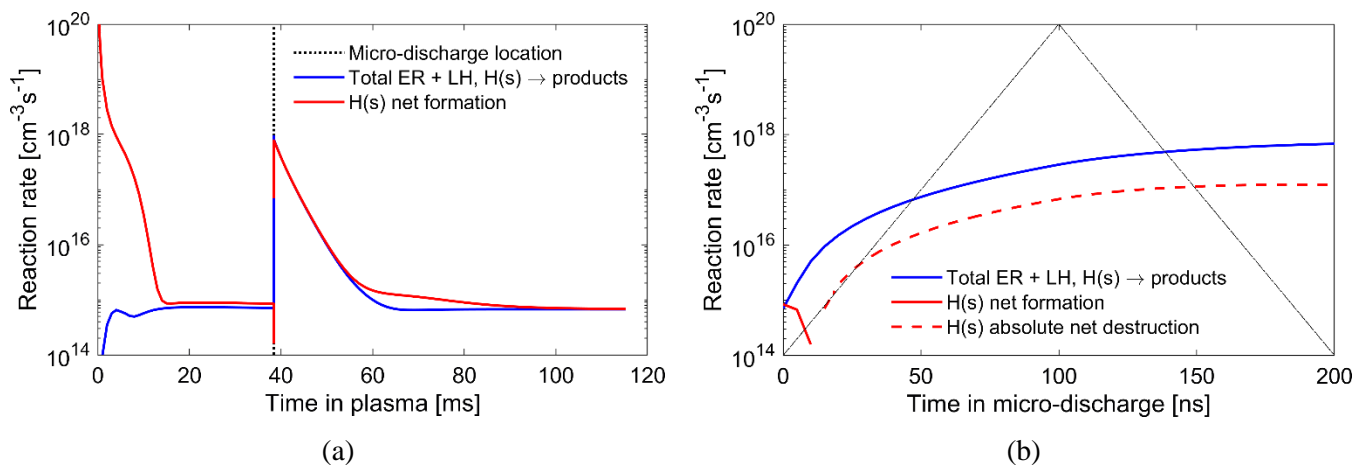
Figure S12. Total and net reaction rates for the formation and consumption of H(s) as a function of time in the plasma, from the start of the plasma to the end of the first micro-discharge and afterglow pair (a), and as a function of time in the first micro-discharge (b). In (a), the micro-discharge with a 200 ns duration takes place at 38.4 ms.

(a)

(b)
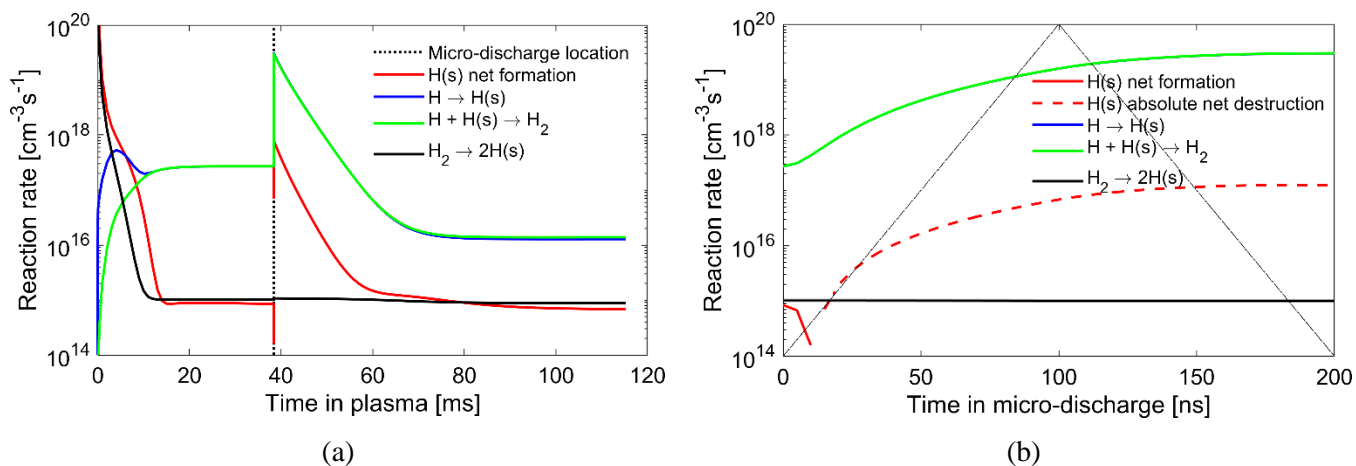
Figure S13. Net formation of H(s) and the individual reactions that determine the net formation as a function of time in the plasma, from the start of the plasma to the end of the first micro-discharge and afterglow pair (a), and as a function of time in the first micro-discharge (b). The green and blue curves generally overlap (i.e., H → H(s) and H + H(s) → H₂). In (a), the micro-discharge with a 200 ns duration takes place at 38.4 ms.

We show in figure S14 the rates of direct adsorption of N and H atoms and compare it to the dissociation rates of N_2 and H_2. The dissociation rates of both N_2 and H_2 (i.e., upon electron impact) exhibit a sharp peak in the micro-discharge (red curves), followed by a pronounced drop, because the electric field reduces to near 0 directly after the micro-discharge (cf. section S.3 above). In the micro-discharges, the H_2 dissociation rate is 3 orders of magnitude higher, and consequently H adsorption is also 3 orders of magnitude faster than N

adsorption. Directly after the micro-discharges, the ER reaction between H and N(s) (green dashed curve) clearly overlaps with direct adsorption of N (blue solid line). The dissociation of H_2 eventually overlaps with the direct adsorption of H in the afterglows (red and blue dashed lines), while the N_2 dissociation overlaps more with the ER reaction between N and H(s) (red and green solid lines). However, due to the quenching of H(s) back to H_2, we need to consider the net formation of H(s). This reaction rate is higher than for the ER reaction between N and H(s) (green curve). Instead, the net H(s) formation overlaps with the sum of all the ER and LH reactions that lead towards NH_3 and which require H(s) (cf. figure S12(a)).

(a)   (b)
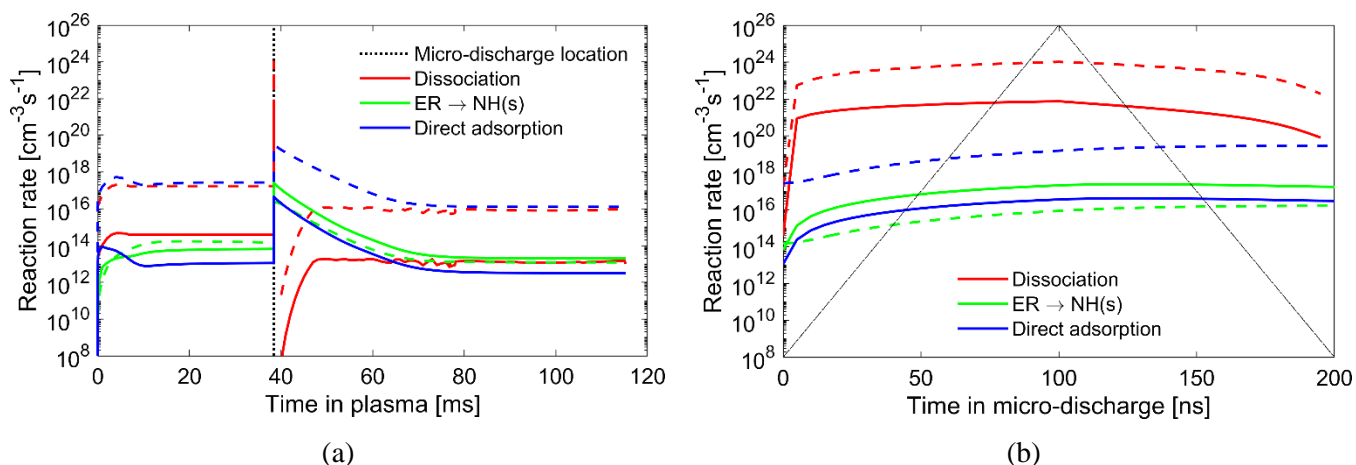
Figure S14. Gas phase dissociation and atomic adsorption reaction rates for nitrogen (solid lines) and hydrogen (dashed lines) as a function of time in the plasma, from the start of the plasma to the end of the first micro-discharge and afterglow pair. The curves of "ER $\rightarrow$ NH(s)" are defined according the gas phase atom, i.e. N + H(s) is the solid curve and H + N(s) is the dashed curve. In (a), the micro-discharge with a 200 ns duration takes place at 38.4 ms.

Based on the above, we identify the adsorption of N and H atoms, both in ER reactions and direct adsorption, as rate-limiting. Consequently, electron impact dissociation of N_2 or H_2 in the plasma can be the overall rate-limiting step. In order to further specify the rate-limiting step, we performed calculations in which the rate coefficients for the atomic adsorption processes or for electron impact gas phase dissociation are multiplied by a factor 2. The adjusted reactions are listed in table S10 and the results are compared in figure S15.

Table S9. The test cases to confirm the rate-limiting reaction step. In each case the rate coefficient of the listed reactions was multiplied by a factor two.

Case	Modified reactions
Reference	None
Increased H_2 dissociation	$e^- + H_2(X,V) \rightarrow e^- + H + H$
Increased H atom adsorption	$H + Surface \rightarrow H(s)$ $H + H(s) \rightarrow H_2$ $H + N(s) \rightarrow NH(s)$ $H + NH(s) \rightarrow NH_2(s)$ $H + NH_2(s) \rightarrow NH_3$
Increased N_2 dissociation	$e^- + N_2(X,E,V) \rightarrow e^- + N + N$
Increased N atom adsorption	$N + Surface \rightarrow N(s)$ $N + H(s) \rightarrow NH(s)$ $N + N(s) \rightarrow N_2$
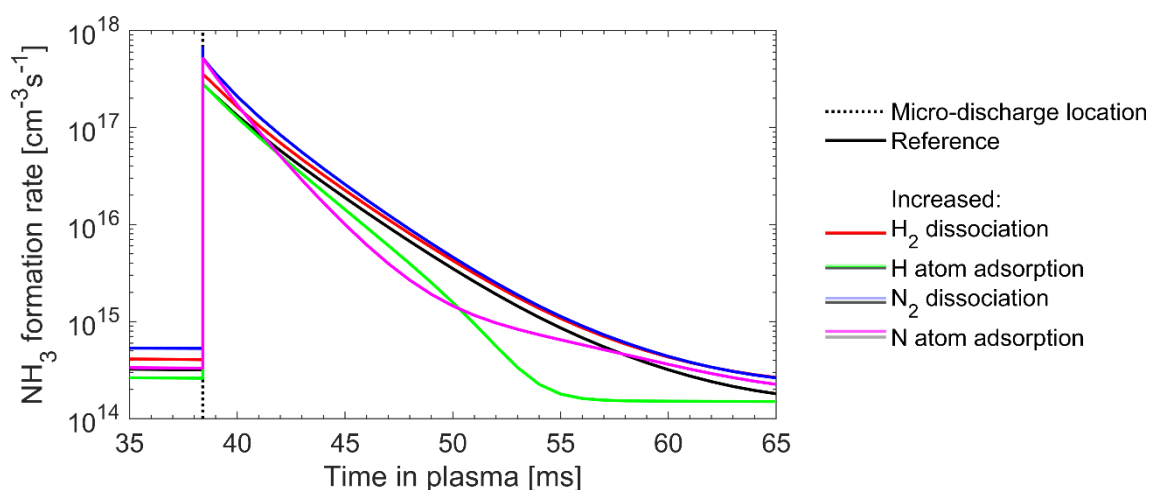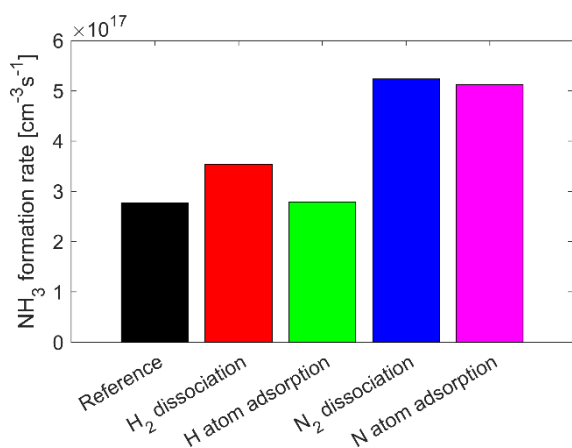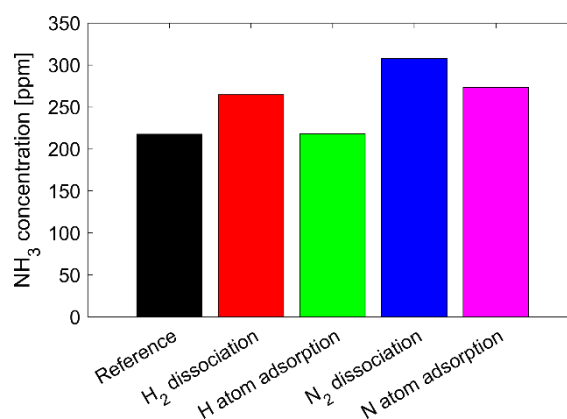
Figure S15. Comparisons of the various test cases presented in table S8 in which we increase the rate coefficients of specific reactions by a factor 2 (cf. table S8), showing the effect on the NH_3 formation rate, i.e. the reaction rate of $NH_2(s) + H(s) \rightarrow NH_3$, as a function of time (a), and 15 μs after the micro-discharge (b), and the eventual NH_3 concentration (c). In (a), the micro-discharge with a 200 ns duration takes place at 38.4 ms.

It is clear from figure S15(a) that the increased rate coefficient of the feed gas dissociation and of the atomic adsorption influences the final NH_3 synthesis reaction step ($NH_2(s) + H(s) \rightarrow NH_3$). Most notably, the slope of the increased N adsorption is steeper, due to faster depletion of gas phase N atoms. Only an increased H atom adsorption does not increase the NH_3 formation rate throughout the afterglow, which is attributed to the faster H atom recombination rate by $H + H(s) \rightarrow H_2$.

In figure S15(b) the NH_3 formation rates are compared shortly after the micro-discharge. Clearly both an increase in N_2 dissociation and N atom adsorption by a factor 2 effectively enhance the NH_3 formation rate by the same factor 2, directly after the micro-discharge. However, as noted before, the NH_3 formation rate with increased N atom adsorption rates will fall below the reference, due to the faster depletion of N atoms in the gas. An increase in the H_2 dissociation by a factor 2 also enhances the NH_3 formation rate, but only by a factor

1.3, due to a slight increase in H(s), and thus all further hydrogenation processes on the surface (N + H(s) → NH(s), NH(s) + H(s) → NH₂(s) and NH₂(s) → NH₃). The increase by a factor 1.3, instead of 2, approximately follows by considering all these three hydrogenation processes (i.e., $\sqrt[3]{2} = 1.26$).

In figure S15(c) the eventual NH₃ concentration is shown. Here the factor 2 increase is not directly reflected, due to how steady state is reached, i.e. because the overall system is non-linear in time. An increased gas phase H₂ dissociation enhances the NH₃ concentration by a factor 1.22. N atom adsorption increases the NH₃ concentration slightly more (factor 1.27), mainly due to an increase in N + H(s) → NH(s). H atom adsorption does not increase the NH₃ formation rate and the eventual NH₃ concentration is equal. The largest benefit is seen from an increased electron impact N₂ dissociation in the gas phase, enhancing the NH₃ concentration by a factor 1.41.

Based on the above analysis, electron impact N₂ dissociation in the plasma, followed by N atom adsorption at the surface, is identified as the rate-limiting step determining the NH₃ yield. H₂ dissociation in the plasma can also increase the formed NH₃, but to a lesser extent, as the H(s) precursor is required in multiple reaction steps. In addition, the surface is always generally covered with H(s) (see figure 1(a) in the main paper) and H₂ is easier to dissociate than N₂ (i.e. a dissociation threshold of 4.5 eV and 9.8 eV, respectively), thus the rate-limiting behaviour of the NH₃ synthesis in a DBD is attributed to nitrogen.

S.5. N₂ Dissociative Adsorption Compared Against N Atom Direct Adsorption

Figure S16. Comparison of N(s) formation rates from the various atomic adsorption and dissociative adsorption processes, resolved for the ground state species (X), electronically excited states (E) and vibrational levels (V), as a function of time in the plasma, from the start of the plasma to the end of the first micro-discharge and afterglow pair. The micro-discharge with a 200 ns duration takes place at 38.4 ms.
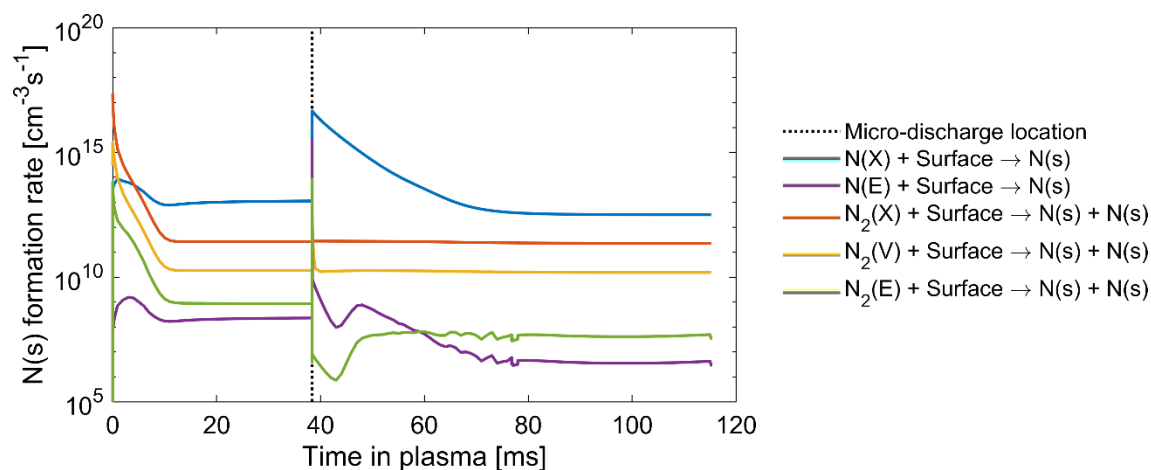
S.6. Data Used in the Assessment of the Reaction Mechanisms

We present the data based on which we assessed the reaction mechanisms presented in the main paper. We based ourself on the N_xH_y gas phase species (i.e. N, H, NH, NH_2 and NH_3), the surface adsorbed and related species (i.e. Surface (free sites), N(s), H(s) NH(s) and NH_2(s)) and the electrons and feed gas (i.e. e⁻ and H_2 and N_2, respectively). In addition, any other relevant species that is dictated by the significant reactions are also presented (i.e. electronically excited molecules: H_2(E) and N_2(E) and ions: N_2^+, H_2^+, N_2H^+ and H_3^+). We first considered separately whether or not the species is produced or destroyed during the micro-discharge and during the afterglow (cf. also figure 4 in the main paper). The reaction rates, source terms and the reactions themselves were carefully inspected to determine whether or not the single reaction could be considered, and if indeed only the production or destruction had to be considered during a single phase of the discharge (i.e. the micro-discharges and their afterglows).

The above analysis was based on the relative information instead of the absolute rates, i.e. the production-to-destruction ratio and the contribution of a reaction to either the production or destruction of a specific species. This is because the total source terms, and thus the typical reaction rates, can differ by orders of magnitude between the various species (cf. figure 4 and 5 in the main paper). In table S10 and S11 we present the reactions and their contribution to either the production or destruction of a species during the micro-discharge and the afterglow, respectively. In addition we note how we considered the species, based on the production-to-destruction ratio. The (individual) vibrational levels of both the N_2 and H_2 molecules, as well as the N_2 electronic states, N_2(E), are not resolved in table S9 of the micro-discharges, as those species typically show fast excitation and de-excitation processes between the various levels or states. Similarly, in addition in the afterglow (table S10), the H_2(X) and N_2(X) ground states are populated (and depopulated) by the various vibrational interactions and (de-)excitation processes and H_2(E) is mainly quenched back to the feed gas. Those interactions were not considered in detail, however typical vibrational distribution functions were shown in figure 3 and S6 for N_2 and H_2, respectively.

For context, we provide the reaction rates of the listed reactions in table S12, time averaged over the first micro-discharge and over the afterglow. Some reactions were not explicitly mentioned in the main paper (numbered in the tables with n.a.), those reactions typically quench any desired product back to the feed gas or indicate the population of electronically excited states or vibrational levels, which lead to the subsequent interactions between those states or levels.

Table S10. The various species considered in the assessment of the reaction mechanisms and the most significant reactions and their contribution to the production (+) and/or destruction (−) of this species in the micro-discharges. Either the production, destruction or both are given, depending on the specific consideration made, which is based on the production-to-destruction ratio (P/D).

Species	Consideration	(# main paper) Reaction	Contribution
$NH_2(s)$	Most significantly produced (P/D = 1.8)	(13) $NH + H(s) \rightarrow NH_2(s)$	0.86 (+)
		(19) $NH(s) + H(s) \rightarrow NH_2(s)$	0.14 (+)
$NH(s)$	Most significantly produced (P/D = 12)	(16) $N + H(s) \rightarrow NH(s)$	0.84 (+)
$H(s)$	Produced and destroyed (P/D = 0.98)	(14) $H + Surface \rightarrow H(s)$	1.00 (+)
		(15) $H + H(s) \rightarrow H_2$	0.98 (−)
$N(s)$	Most significantly produced (P/D = 3.2)	(17) $N + Surface \rightarrow N(s)$	0.96 (+)
Surface	Produced and destroyed (P/D = 1.01)	(15) $H + H(s) \rightarrow H_2 + Surface$	0.99 (+)
		(14) $H + Surface \rightarrow H(s)$	1.00 (−)
NH_3	Most significantly destroyed (P/D = 0.08)	(21) $e^- + NH_3 \rightarrow e^- + NH_2 + H$	0.56 (−)
		(22) $e^- + NH_3 \rightarrow e^- + NH + H_2$	0.32 (−)
NH_2	Produced and destroyed (P/D = 18)	(21) $e^- + NH_3 \rightarrow e^- + NH_2 + H$	0.92 (+)
NH	Most significantly produced (P/D = 3.1)	(12) $N + H_2(E) \rightarrow H + NH$	0.99 (+)
H	Most significantly produced (P/D = 421)	(6) $e^- + H_2(X,V,E) \rightarrow e^- + H + H$	0.89 (+)
		(10) $N_2(E) + H_2 \rightarrow N_2 + H + H$	0.10 (+)
N	Most significantly produced (P/D = 1.4)	(5) $e^- + N_2(X,V,E) \rightarrow e^- + N + N$	0.78 (+)
$H_2(X)$	Most significantly destroyed (P/D = 0.03)	(6) $e^- + H_2(X) \rightarrow e^- + H + H$	0.63 (−)
		(11) $e^- + H_2 \rightarrow e^- + H_2(E)$	0.27 (−)
$H_2(E)$	Most significantly produced (P/D = 6.0)	(11) $e^- + H_2 \rightarrow e^- + H_2(E)$	1.00 (+)
$N_2(X)$	Most significantly destroyed (P/D = 0.13)	(n. a.) $e^- + N_2(X) \rightarrow e^- + N_2(V)$	0.94 (−)
e^-	Most significantly produced (P/D = 3.1)	(7) $e^- + N_2 \rightarrow e^- + e^- + N_2^+$	0.65 (+)
		(8) $e^- + H_2 \rightarrow e^- + e^- + H_2^+$	0.17 (+)
N_2^+	Produced and destroyed (P/D = 1.00)	(7) $e^- + N_2 \rightarrow e^- + e^- + N_2^+$	0.52 (+)
		(n. a.) $e^- + N_2(E) \rightarrow e^- + e^- + N_2^+$	0.44 (+)
		(28) $N_2^+ + H_2 \rightarrow N_2H^+ + H$	0.98 (−)
H_2^+	Produced and destroyed (P/D = 1.00)	(8) $e^- + H_2 \rightarrow e^- + e^- + H_2^+$	1.00 (+)
		(27) $H_2^+ + H_2 \rightarrow H_3^+ + H$	0.76 (−)
		(n. a.) $H_2^+ + N_2 \rightarrow N_2H^+ + H$	0.24 (−)
H_3^+	Most significantly produced (P/D = 5.8)	(27) $H_2^+ + H_2 \rightarrow H_3^+ + H$	1.00 (+)
N_2H^+	Most significantly produced (P/D = 2.1)	(28) $N_2^+ + H_2 \rightarrow N_2H^+ + H$	0.67 (+)
		(n. a.) $H_2^+ + N_2 \rightarrow N_2H^+ + H$	0.33 (+)

Table S11. The various species considered in the assessment of the reaction mechanisms and the most significant reactions and their contribution to the production (+) and/or destruction (−) of this species in the afterglows of the micro-discharges. Either the production, destruction or both are given, depending on the specific consideration made which is based on the production-to-destruction ratio (P/D).

Species	Consideration	(# main paper) Reaction	Contribution
$NH_2(s)$	Produced and destroyed (P/D = 1.00)	(19) $NH(s) + H(s) \rightarrow NH_2(s)$	0.99 (+)
		(20) $NH_2(s) + H(s) \rightarrow NH_3$	1.00 (−)
$NH(s)$	Produced and destroyed (P/D = 1.00)	(16) $N + H(s) \rightarrow NH(s)$	0.86 (+)
		(18) $H + N(s) \rightarrow NH(s)$	0.14 (+)
		(19) $NH(s) + H(s) \rightarrow NH_2(s)$	1.00 (−)
$H(s)$	Produced and destroyed (P/D = 1.00)	(14) $H + Surface \rightarrow H(s)$	1.00 (+)
		(15) $H + H(s) \rightarrow H_2$	0.98 (−)
$N(s)$	Produced and destroyed (P/D = 1.1)	(17) $N + Surface \rightarrow N(s)$	1.00 (+)
		(18) $H + N(s) \rightarrow NH(s)$	1.00 (−)
Surface	Produced and destroyed (P/D = 1.00)	(15) $H + H(s) \rightarrow H_2 + Surface$	0.98 (+)
		(14) $H + Surface \rightarrow H(s)$	1.00 (−)
NH_3	Most significantly produced (P/D = 8.7)	(20) $NH_2(s) + H(s) \rightarrow NH_3$	0.88 (+)
NH_2	Produced and destroyed (P/D = 1.00)	(21) $e^- + NH_3 \rightarrow e^- + NH_2 + H$	0.29 (+)
		(n. a.) $N + H_2 + M \rightarrow NH_2 + M$	0.66 (+)
		(n. a.) $H + NH_2 \rightarrow H_2 + NH$	0.33 (−)
		(n. a.) $N + NH_2 \rightarrow N_2 + H_2$	0.19 (−)
		(n. a.) $N + NH_2 \rightarrow N_2 + H + H$	0.19 (−)
		(23) $NH_2 + H(s) \rightarrow NH_3$	0.10 (−)
NH	Produced and destroyed (P/D = 0.97)	(12) $N + H_2(E) \rightarrow H + NH$	0.99 (+)
		(n. a.) $H + NH \rightarrow N + H_2$	0.98 (−)
H	Most significantly destroyed (P/D = 0.14)	(14) $H + Surface \rightarrow H(s)$	0.35 (−)
		(15) $H + H(s) \rightarrow H_2$	0.35 (−)
		(n. a.) $H + H + H_2 \rightarrow H_2 + H_2$	0.13 (−)
		(n. a.) $H + NH \rightarrow N + H_2$	0.13 (−)
N	Produced and destroyed (P/D = 0.98)	(n. a.) $H + NH \rightarrow N + H_2$	1.00 (+)
		(12) $N + H_2(E) \rightarrow H + NH$	0.96 (−)
e^-	Most significantly destroyed (P/D = 0.008)	(24) $e^- + H_3^+ \rightarrow H_2 + H$	0.30 (−)
		(25) $e^- + H_3^+ \rightarrow H + H + H$	0.30 (−)
		(26) $e^- + N_2H^+ \rightarrow N_2 + H$	0.37 (−)
N_2^+	Produced and destroyed (P/D = 0.98)	(n. a.) $N_2(E) + N_2(E) \rightarrow N_2^+ + N_2 + e^-$	1.00 (+)
		(28) $N_2^+ + H_2 \rightarrow N_2H^+ + H$	0.98 (−)
H_2^+	Most significantly destroyed (P/D = 0.008)	(27) $H_2^+ + H_2 \rightarrow H_3^+ + H$	0.78 (−)
		(n. a.) $H_2^+ + N_2 \rightarrow N_2H^+ + H$	0.21 (−)
H_3^+	Most significantly destroyed (P/D = 3×10⁻⁶)	(24) $e^- + H_3^+ \rightarrow H_2 + H$	0.50 (−)
		(25) $e^- + H_3^+ \rightarrow H + H + H$	0.50 (−)
N_2H^+	Most significantly destroyed (P/D = 0.0002)	(26) $e^- + N_2H^+ \rightarrow N_2 + H$	1.00 (−)

Table S12. The time averaged reaction rates, of the reactions in table S10 and S11, during a micro-discharge and its afterglow.

(# main paper) Reaction	Reaction rate (cm^{-3}s^{-1}), time averaged over the:	
	Micro-discharge	Afterglow
(4) $H_2 + \text{Surface} \rightarrow H(s) + H(s)$	1.01×10^{15}	9.46×10^{14}
(5) $e^- + N_2(X, V, E) \rightarrow e^- + N + N$	4.63×10^{21}	1.19×10^{13}
(6) $e^- + H_2(X, V, E) \rightarrow e^- + H + H$	4.81×10^{23}	7.72×10^{15}
(7) $e^- + N_2 \rightarrow e^- + e^- + N_2^+$	1.78×10^{20}	7.80×10^6
(8) $e^- + H_2 \rightarrow e^- + e^- + H_2^+$	6.84×10^{20}	3.65×10^7
(9) $e^- + N_2 \rightarrow e^- + N_2(E)$	2.45×10^{23}	6.41×10^{15}
(10) $N_2(E) + H_2 \rightarrow N_2 + H + H$	5.59×10^{22}	1.64×10^{16}
(11) $e^- + H_2 \rightarrow e^- + H_2(E)$	2.04×10^{23}	1.81×10^{15}
(12) $N + H_2(E) \rightarrow H + NH$	7.81×10^{21}	4.17×10^{17}
(13) $NH + H(s) \rightarrow NH_2(s)$	8.77×10^{16}	3.89×10^{13}
(14) $H + \text{Surface} \rightarrow H(s)$	1.55×10^{19}	1.17×10^{18}
(15) $H + H(s) \rightarrow H_2$	1.55×10^{19}	1.15×10^{18}
(16) $N + H(s) \rightarrow NH(s)$	1.49×10^{17}	7.36×10^{15}
(17) $N + \text{Surface} \rightarrow N(s)$	2.57×10^{16}	1.30×10^{15}
(18) $H + N(s) \rightarrow NH(s)$	8.46×10^{15}	1.18×10^{15}
(19) $NH(s) + H(s) \rightarrow NH_2(s)$	1.47×10^{16}	8.51×10^{15}
(20) $NH_2(s) + H(s) \rightarrow NH_3$	5.57×10^{16}	8.60×10^{15}
(21) $e^- + NH_3 \rightarrow e^- + NH_2 + H$	1.36×10^{19}	8.54×10^{14}
(22) $e^- + NH_3 \rightarrow e^- + NH + H_2$	7.73×10^{18}	1.88×10^{14}
(23) $NH_2 + H(s) \rightarrow NH_3$	3.40×10^{14}	3.09×10^{14}
(24) $e^- + H_3^+ \rightarrow H_2 + H$	4.29×10^{19}	5.53×10^{14}
(25) $e^- + H_3^+ \rightarrow H + H + H$	4.29×10^{19}	5.53×10^{14}
(26) $e^- + N_2H^+ \rightarrow N_2 + H$	2.30×10^{20}	6.85×10^{14}
(27) $H_2^+ + H_2 \rightarrow H_3^+ + H$	5.19×10^{20}	3.36×10^9
(28) $N_2^+ + H_2 \rightarrow N_2H^+ + H$	3.38×10^{20}	1.38×10^{11}
(n. a.) $H + NH_2 \rightarrow H_2 + NH$	1.63×10^{17}	9.67×10^{14}
(n. a.) $N + NH_2 \rightarrow N_2 + H_2$	1.43×10^{17}	5.75×10^{14}
(n. a.) $N + NH_2 \rightarrow N_2 + H + H$	1.43×10^{17}	5.75×10^{14}
(n. a.) $e^- + N_2(E) \rightarrow e^- + e^- + N_2^+$	1.53×10^{20}	4.98×10^8
(n. a.) $H_2^+ + N_2 \rightarrow N_2H^+ + H$	1.64×10^{20}	9.23×10^8
(n. a.) $N + H_2 + M \rightarrow NH_2 + M$	1.06×10^{15}	1.94×10^{15}
(n. a.) $H + NH \rightarrow N + H_2$	2.51×10^{21}	4.25×10^{17}
(n. a.) $H + H + H_2 \rightarrow H_2 + H_2$	5.03×10^{18}	2.23×10^{17}

The data presented in table S10 and S11 also gives some insight in the sensitivity of the overall assessed reaction mechanisms to changes in the underlying rate coefficients of either the involved reactions themselves or of other reactions also present in the chemistry set (cf. table S1-S6). Indeed, reaction rate coefficients always have an uncertainty, typically in the order of 30%.[48,49] In general, if we concluded that there is only one significant reaction relevant to the production or destruction of one species, while the contribution of this reaction is just slightly above 0.5 (i.e. 50%), then it is clear that a slight change in this or other reactions could change the actual main reaction taking place. On the other hand, if we find a large contribution to the overall production or destruction (i.e. contributions of 0.8, or 80%, and up), then it is less likely that other reactions that were not part of our assessed reaction mechanisms (which thus have very low contributions) would become the most important, even when the uncertainties in the rate coefficients are considered. In table S10 and S11, the lowest

considered contribution to the production or destruction of a species, for determining the reaction mechanisms, is 0.81, i.e. 81%, which is the sum of the four reactions $(0.33 + 0.19 + 0.19 + 0.1)$ accounting for the destruction of NH_2 in the afterglow (cf. table S11).

S.7. Influence of Langmuir-Hinshelwood Reactions and Alternative Reaction Mechanisms

Because the adopted Langmuir-Hinshelwood activation energies are subject to uncertainties, we calculate several hypothetical cases in which we change the activation energy and thus the rate coefficients governing the reactions, as shown in table S13. The diffusion barrier is kept constant, as reported in table S6. We cover cases in which the reactions are slower and faster. Results are given in table S14.

Table S13. Summary of the calculations performed to investigate the influence of the LH reactions.

Case	Reaction			Activation energy	Rate coefficient cm^3s^{-1}	s^{-1}
Adopted chemistry	$H(s) + N(s)$	$\rightarrow$	$NH(s)$	$E_a = 1.099$ eV	7.5×10^{-22}	1.1×10^{-4}
	$H(s) + NH(s)$	$\rightarrow$	$NH_2(s)$	$E_a = 0.3$ eV	8.8×10^{-12}	1.3×10^6
	$H(s) + NH_2(s)$	$\rightarrow$	NH_3	$E_a = 0.2$ eV	1.6×10^{-10}	2.3×10^7
Equal barriers	$H(s) + N(s)$	$\rightarrow$	$NH(s)$	$E_a = 1.0$ eV	1.3×10^{-20}	1.9×10^{-3}
	$H(s) + NH(s)$	$\rightarrow$	$NH_2(s)$	$E_a = 1.0$ eV	1.3×10^{-20}	1.9×10^{-3}
	$H(s) + NH_2(s)$	$\rightarrow$	NH_3	$E_a = 1.0$ eV	1.3×10^{-20}	1.9×10^{-3}
Increased barriers	$H(s) + N(s)$	$\rightarrow$	$NH(s)$	$E_a = 2.0$ eV	3.3×10^{-33}	4.8×10^{-16}
	$H(s) + NH(s)$	$\rightarrow$	$NH_2(s)$	$E_a = 2.0$ eV	3.3×10^{-33}	4.8×10^{-16}
	$H(s) + NH_2(s)$	$\rightarrow$	NH_3	$E_a = 2.0$ eV	3.3×10^{-33}	4.8×10^{-16}
Barrierless	$H(s) + N(s)$	$\rightarrow$	$NH(s)$	$E_a = 0.0$ eV	5.3×10^{-8}	7.6×10^9
	$H(s) + NH(s)$	$\rightarrow$	$NH_2(s)$	$E_a = 0.0$ eV	5.3×10^{-8}	7.6×10^9
	$H(s) + NH_2(s)$	$\rightarrow$	NH_3	$E_a = 0.0$ eV	5.3×10^{-8}	7.6×10^9

Table S14. Calculated steady state NH_3 concentration and NH_3 formation rate through the LH pathway ($H(s) + NH_2(s) \rightarrow NH_3$) for the various test cases.

Case	NH_3 concentration (ppm)	LH NH_3 formation rate ($cm^{-3}s^{-1}$) in the first afterglow
Basic chemistry	223	$\underline{8.6 \times 10^{15}}$
Equal barriers	224	2.4×10^{10}
Increased barriers	224	6.0×10^{-3}
Barrierless	223	$\underline{8.7 \times 10^{15}}$

Table S14 lists the calculated steady-state NH_3 concentration for the basic model and the additional calculations. It can be seen that all additional calculations give the same concentration as the basic chemistry which was used to assess the reaction mechanisms in detail. In the basic chemistry model we found that the eventual formation of NH_3 is through the LH reaction: $H(s) + NH_2(s) \rightarrow NH_3$. Table S14 also reports the corresponding reaction rate of this LH reaction. Despite the same NH_3 concentration, we do see different LH reaction rates when increasing the activation energy (i.e. for barriers of 1.0 eV and 2.0 eV in the case of equal barriers and increased barriers, respectively). This means that reactions other than this LH reaction should be responsible for the formation of NH_3. When the LH reactions were barrierless, the eventual rate is the same, despite a significantly higher rate coefficient (cf. table S13), thus indicating a preceding step as rate limiting, i.e. the formation of $NH(s)$ by ER reactions. Indeed, also when the LH formation of $NH(s)$ is increased, i.e. the barrierless case, the formation rate is still the same, indicating that the same ER $NH(s)$ formation is still faster than the LH alternative.

In addition, when the LH reactions are slower (increased barriers), we don't see a change in the main formation of $NH(s)$ by the ER reactions, but we do see other NH3 formation reactions taking place in the final step, with the same rate as when the formation was due to LH reactions, as shown in table S15.

Table S15. Comparison of the NH_3 formation rate by the most important reactions for the various test cases.

Case	NH₃ formation rate (cm⁻³s⁻¹) in the first afterglow		
	$H(s) + NH_2(s) \rightarrow NH_3$	$H_2 + NH(s) \rightarrow NH_3$	$H + NH_2(s) \rightarrow NH_3$
Basic chemistry	$\underline{8.6 \times 10^{15}}$	3.4×10^{13}	2.2×10^{11}
Equal barriers	2.4×10^{10}	$\underline{7.7 \times 10^{15}}$	7.6×10^{14}
Increased barriers	6.0×10^{-3}	$\underline{7.7 \times 10^{15}}$	7.6×10^{14}
Barrier-less	$\underline{8.7 \times 10^{15}}$	6.8×10^{8}	6.8×10^{8}

The reaction $H_2 + NH(s) \rightarrow NH_3$ is dominant when the LH reaction ($H(s) + NH_2(s) \rightarrow NH_3$) is not fast enough, and is characterized by a nearly equal rate (underlined in table S15). We also list $H + NH_2(s) \rightarrow NH_3$ which has the highest reaction rate after the LH reaction and the H_2 ER reaction in the basic chemistry case. Indeed, we also found that the stepwise ER hydrogenations with H are fast enough to account for the same NH_3 formation rates if the H_2 ER reaction is absent.

Based on the above we can present two alternative NH_3 formation paths as revealed by our model. After the ER formation of $NH(s)$, a single reaction step might form NH_3:

$$H_2 + NH(s) \rightarrow NH_3 \tag{S13}$$

Alternatively, stepwise ER hydrogenation reactions might form NH_3:

$$H + NH(s) \rightarrow NH_2(s) \tag{S14}$$

$$H + NH_2(s) \rightarrow NH_3 \tag{S15}$$

References

(1)   Pancheshnyi, S.; Eismann, B.; Hagelaar, G. J. M.; Pitchford, L.C. Computer code ZDPlasKin, versions 2.0a; University of Toulouse: LAPLACE, CNRS-UPS-INP, Toulouse, France. http://www.zdplaskin.laplace.univ-tlse.fr (2008).

(2)   Hagelaar, G. J. M.; Pitchford, L. C. Solving the Boltzmann Equation to Obtain Electron Transport Coefficients and Rate Coefficients for Fluid Models. *Plasma Sources Sci. Technol.* **2005**, *14*.

(3)   van 't Veer, K.; Reniers, F.; Bogaerts, A. Zero-Dimensional Modelling of Unpacked and Packed Bed Dielectric Barrier Discharges: The Role of Vibrational Kinetics in Ammonia Synthesis. *Plasma Sources Sci. Technol.* **2020**, *29*, 045020.

(4)   Kim, H.; Nanba, T. Atmospheric-Pressure Nonthermal Plasma Synthesis of Ammonia over Ruthenium Catalysts. *Plasma Process. Polym.* **2016**, 1–9.

(5)   Alves, L. L. The IST-LISBON Database on LXCat. *J. Phys. Conf. Ser.* **2014**, *565*, 012007.

(6)   Morgan database. https://nl.lxcat.net/ (accessed May, 2019).

(7)   Tarnovsky, V.; Deutsch, H.; Becker, K. Cross-Sections for the Electron Impact Ionization of ND_x (x = 1−3). *Int. J. Mass Spectrom. Ion Process.* **1997**, *167–168*, 69–78.

(8)   Itikawa, Y. Cross Sections for Electron Collisions with Nitrogen Molecules. *J. Phys. Chem. Ref. Data* **2005**, *35*, 31–53.

(9)   Yoon, J.-S.; Song, M.-Y.; Han, J.-M.; Hwang, S. H.; Chang, W.-S.; Lee, B.; Itikawa, Y. Cross Sections for Electron Collisions with Hydrogen Molecules. *J. Phys. Chem. Ref. Data* **2008**, *37*, 913–931.

(10)   Carrasco, E.; Jiménez-Redondo, M.; Tanarro, I.; Herrero, V. J. Neutral and Ion Chemistry in Low Pressure Dc Plasmas of H2/N2 Mixtures: Routes for the Efficient Production of NH_3 and NH_4^+. *Phys. Chem. Chem. Phys.* **2011**, *13*, 19561–19572.

(11)   Capitelli, M.; Ferreira, C. M.; Gordiets, B. F.; Asipov, A. I. *Plasma Kinetic in Atmospheric Gases*; Springer-Verlag Berlin Heidelberg: Berlin, 2000.

(12)   Nighan, W. L. Electron Energy Distributions and Collision Rates in Electrically Excited N_2, CO, and CO_2. *Phys. Rev. A* **1970**, *2*, 1989–2000.

(13)   Kossyi, I. A.; Kostinsky, A. Y.; Matveyev, A. A.; Silakov, V. P. Kinetic Scheme of the Non-Equilibrium Discharge in Nitrogen-Oxygen Mixtures. *Plasma Sources Sci. Technol.* **1992**, *1*, 207–220.

(14)   Celiberto, R.; Janev, R. K.; Wadehra, J. M.; Laricchiuta, A. Cross Sections for 14-eV e-H_2 Resonant Collisions: Dissociative Electron Attachment. *Phys. Rev. A* **2009**, *80*, 12712.

(15)   Laporta, V.; Little, D. A.; Celiberto, R.; Tennyson, J. Electron-Impact Resonant Vibrational Excitation and Dissociation Processes Involving Vibrationally Excited N_2 Molecules. *Plasma Sources Sci. Technol.* **2014**, *23*, 065002.

(16)   Kewley, D. J.; Hornung, H. G. Free-Piston Shock-Tube Study of Nitrogen Dissociation. *Chem. Phys. Lett.* **1974**, *25*, 531-536.

(17)   Gaens, W. Van; Bogaerts, A. Kinetic Modelling for an Atmospheric Pressure Argon Plasma Jet in Humid Air. *J. Phys. D. Appl. Phys.* **2013**, *46*, 275201.

(18)   Gordiets, B.; Ferreira, C. M.; Pinheiro, M. J.; Ricard, A. Self-Consistent Kinetic Model of Low-Pressure N_2–H_2 Flowing Discharges: I. Volume Processes. *Plasma Sources Sci. Technol.* **1998**, *7*, 363–378.

(19)   Caridade, P. J. S. B.; Rodrigues, S. P. J.; Sousa, F.; Varandas, A. J. C. Unimolecular and Bimolecular Calculations for HN_2. *J. Phys. Chem. A* **2005**, *109*, 2356–2363.

(20)   Fontijn, A.; Shamsuddin, S. M.; Crammond, D. Kinetics of the NH Reaction with H_2 and Reassessment of HNO Formation from NH + CO_2, H_2O. *Combust. Flame* **2006**, *145*, 543–551.

(21)   Johnston, H. S. Computation of High-Temperature Rate Constants for Bimolecular Reactions of Combustion Products. *Symp. Combust.* **1967**, *11*, 837–844.

(22)   Klippenstein, S. J.; Harding, L. B.; Ruscic, B.; Sivaramakrishnan, R.; Srinivasan, N. K.; Su, M.; Michael, J. V. Thermal Decomposition of NH_2OH and Subsequent Reactions: Ab Initio Transition State Theory and Reflected Shock Tube Experiments. *J. Phys. Chem. A* **2009**, *113*, 10241–10259.

(23)   Sheets, D. Chemical Kinetic Data Sheets for High-Temperature Chemical Reactions. *J. Phys. Chem. Ref. Data* **1983**, *12*, 531.

(24)   Deppe, J.; Friedrichs, G.; Ibrahim, A.; Romming, H.; Wagner, H. G. The Thermal Decomposition of NH_2 and NH Radicals. *Berichte der Bunsengesellschaft für Phys. Chemie* **1998**, *102*, 1474–1485.

(25)   Hanson, R. K.; Salimian, S. Survey of Rate Constants in the N/H/O System. In *Combustion Chemistry*; Gardiner, W. C., Ed.; Springer New York: New York, 1984; pp 361–421.

(26)   Clyne, M. A. A.; Stedman, D. H. Rate of Recombination of Nitrogen Atoms. *J. Phys. Chem.* **1967**, *71*, 3071–3073.

(27)   Fridman, A. *Plasma Chemistry*; Cambridge University Press: Cambridge, U.K., 2008.

(28)   Hong, J.; Pancheshnyi, S.; Tam, E.; Lowke, J. J.; Prawer, S.; Murphy, A. B. Kinetic Modelling of NH_3 Production in N_2–H_2 Non-Equilibrium Atmospheric-Pressure Plasma Catalysis. *J. Phys. D. Appl. Phys.* **2018**, *51*, 109501.

(29)   Anicich, V. G. Evaluated Bimolecular Ion-Molecule Gas Phase Kinetics of Positive Ions for Use in Modeling Planetary Atmospheres, Cometary Comae, and Interstellar Clouds. *J. Phys. Chem. Ref. Data* **1993**, *22*, 1469–1569.

(30)   Wang, W.; Snoeckx, R.; Zhang, X.; Cha, M. S.; Bogaerts, A. Modeling Plasma-Based CO_2 and CH_4 Conversion in Mixtures with N_2, O_2, and H_2O: The Bigger Plasma Chemistry Picture. *J. Phys. Chem. C* **2018**, *122*, 8704–8723.

(31)   Celiberto, R.; Janev, R. K.; Wadehra, J. M.; Laricchiuta, A. Cross Sections for 11-14-eV e-H_2 Resonant Collisions: Vibrational Excitation. *Phys. Rev. A.* **2008**, *77*, 012714.

(32)   Celiberto, R.; Janev, R. K.; Laporta, V.; Tennyson, J.; Wadehra, J. M. Electron-Impact Vibrational Excitation of Vibrationally Excited H_2 molecules Involving the Resonant $^2\Sigma_g^+$ Rydberg-Excited Electronic State. *Phys. Rev. A.* **2013**, *88*, 062701.

(33)   Esposito, F. N–N_2 State to State Vibrational-Relaxation and Dissociation Rates Based on Quasiclassical Calculations. *Chem. Phys.* **2006**, *331*, 1–8.

(34)   Adamovich, I. V; Rich, J. W.; Treanor, C. E. Vibrational Energy Transfer Rates Using a Forced Harmonic Oscillator Model. *J. Thermophys. Heat Transf.* **1998**, *12*, 57-65.

(35)   Billing, D.; Guldberg, A.; He, N. E.; Hansen, F. Y. Dissociative Chemisorption of N_2 on Rhenium: Dynamics at Low Impact Energies. *Chem. Phys.* **1990**, *147*, 1–11.

(36)   Hansen, F. Y.; Henriksen, N. E.; Billing, G. D.; Guldberg, A. Catalytic Synthesis of Ammonia Using Vibrationally Excited Nitrogen Molecules: Theoretical Calculation of Equilibrium and Rate Constants. *Surf. Sci.* **1992**, *264*, 225–234.

(37)   Black, G.; Wise, H.; Schechter, S.; Sharpless, R. L.; Black, G.; Wise, H.; Schechter, S.; Sharpless, R. L. Measurements of Vibrationally Excited Molecules by Raman Scattering II. Surface Deactivation of Vibrationally Excited N_2. *J. Chem. Phys.* **1974**, *60*, 3526.

(38)   Heidner, R. F.; Kasper, J. V. V. An Experimental Rate Constant for H+H_2(v'' = 1)→ H+H_2 (v'' = 0). *Chem. Phys. Lett.* **1972**, *15*, 179–184.

(39)   Carrasco, E.; Herrero, V. J.; Tanarro, I. Isotopic Exchange Processes in Cold Plasmas of H_2/D_2 Mixtures. *Phys. Chem. Chem. Phys.* **2011**, *13*, 9655–9666.

(40)   Barth, J. V. Transport of Adsorbates at Metal Surfaces: From Thermal Migration to Hot Precursors. *Surf. Sci. Rep.* **2000**, *40*, 75–149.

(41) Ertl, G. Surface Science and Catalysis- Studies on the Mechanism of Ammonia Synthesis: The P. H. Emmett Award Address. *Catal. Rev. Sci. Eng.* **1980**, *21*, 201–223.

(42) Dumesic, J. A.; Trevino, A. A. Kinetic Simulation of Ammonia Synthesis Catalysis. *J. Catal.* **1989**, *129*, 119–129.

(43) Engelmann, Y.; van 't Veer, K.; Gorbanev, Y.; Neyts, E. C.; Schneider, W. F.; Bogaerts, A. Plasma Catalysis for Ammonia Synthesis: The Importance of Eley-Rideal Reactions. *Submitted.*

(44) Mehta, P.; Barboun, P.; Herrera, F. A.; Kim, J.; Rumbach, P.; Go, D. B.; Hicks, J. C.; Schneider, W. F. Overcoming Ammonia Synthesis Scaling Relations with Plasma-Enabled Catalysis. *Nat. Catal.* **2018**, *1*, 269–275.

(45) Engelmann, Y.; Mehta, P.; Neyts, E. C.; Schneider, W. F.; Bogaerts, A. Predicted Influence of Plasma Activation on Nonoxidative Coupling of Methane on Transition Metal Catalysts. *ACS Sustain. Chem. Eng.* **2020**, *8*, 6043–6054.

(46) Peeters, F. J. J.; Sanden, M. C. M. Van De. The Influence of Partial Surface Discharging on the Electrical Characterization of DBDs. *Plasma Sources Sci. Technol.* **2015**, *24*, 015016.

(47) Uytdenhouwen, Y.; Alphen, S. Van; Michielsen, I.; Meynen, V.; Cool, P.; Bogaerts, A. A Packed-Bed DBD Micro Plasma Reactor for CO_2 Dissociation: Does Size matter? *Chem. Eng. J.* **2018**, *348*, 557–568.

(48) Berthelot, A.; Bogaerts, A. Modeling of CO2 Plasma: Effect of Uncertainties in the Plasma Chemistry. *Plasma Sources Sci. Technol.* **2017**, *26*, 115002.

(49) Wang, W.; Berthelot, A.; Zhang, Q.; Bogaerts, A. Modelling of Plasma-Based Dry Reforming: How Do Uncertainties in the Input Data Affect the Calculation Results? *J. Phys. D. Appl. Phys.* **2018**, *51*, 204003.